2007

First-principles calculations of electric field gradients in complex perovskites

Dandan Mao
College of William & Mary - Arts & Sciences

FIRST-PRINCIPLES CALCULATIONS OF ELECTRIC FIELD GRADIENTS IN COMPLEX PEROVSKITES

Dandan Mao

Jingzhou, Hubei, China

Master of Science, The College of William and Mary, 2001
Bachelor of Science, Peking University, 1999

A Dissertation presented to the Graduate Faculty
of the College of William and Mary in Candidacy for the Degree of
Doctor of Philosophy

Department of Physics

The College of William and Mary
August 2007

ABSTRACT

Various experimental and theoretical work indicate that the local structure and chemical ordering play a crucial role in the different physical behaviors of lead-based complex ferroelectrics with the ABO_3 perovskite structure. First-principles linearized augmented plane wave (LAPW) with the local orbital extension method within local density approximation (LDA) are performed on structural models of $Pb(Zr_{1/2}Ti_{1/2})O_3$ (PZT), $Pb(Sc_{1/2}Ta_{1/2})O_3$ (PST), $Pb(Sc_{2/3}W_{1/3})O_3$ (PSW), and $Pb(Mg_{1/3}Nb_{2/3})O_3$ (PMN) to calculate electric field gradients (EFGs). In order to simulate these disordered alloys, various structural models were constructed with different imposed chemical orderings and symmetries. Calculations were carried out as a function of B-site chemical ordering, applied strain, and imposed symmetry. Large changes in the EFGs are seen in PZT as the electric polarization rotates between the tetragonal and rhombohedral directions. The onset of polarization rotation in monoclinic *Cm* symmetry strongly correlates with the shearing of the TiO_6 octahedron, and there is a sharp change in slope in plots of Ti EFGs versus octahedral distortion index. The same changes in EFGs and the BO_6 shearing corresponding to the change of off-centering direction are also seen in PST. In PSW and PMN, the calculated B cation EFGs showed more sensitivity to the surrounding nearest B neighboring environments. Calculated B atom EFGs in all alloys are considerably larger than those inferred from the NMR measurements. Based on comparisons with experiments, the calculated results are interpreted in terms of static and dynamic structural models of these materials.

TABLE OF CONTENTS

To Mom and Dad

ACKNOWLEDGMENTS

I would like to express my gratitude to Dr. Henry Krakauer, under whose supervision this project was conducted, for his guidance, patience, and support during the tenure of this work.

I would also like to extend special thanks to Dr. E. J. Walter for his encouragement and assistance on all aspects of this project.

Furthermore, I would like to thank the rest of my committee members, Dr. S. Zhang, Dr. G. Hoatson, Dr. R. Vold, and Dr. I. Novikova for careful reading and helpful comments on much of this manuscript.

I am also very grateful for my colleagues and group mates, Dr. Z. Wu, Dr. W. Purwanto, Dr. M. Suewattana, Hendra Kwee, and Dan Pechkis for their support and assistance.

Finally, I would like to acknowledge my family and all of my friends for their continuous trust, support, encouragement, and constructive criticism.

LIST OF TABLES

LIST OF FIGURES

Chapter 1

Introduction

Ferroelectric materials are of great technological importance due to their excellent physical properties. The local structure and the short-range order-disorder in these materials are directly related to their physical behavior. In the present work, electric field gradients are calculated using a first-principles approach in a number of structural models for a series of solid solutions in order to study the local structure of ferroelectrics. Quadrupole nuclear magnetic resonance spectra are then generated from the electric field gradients and compared to experimental measurements. The comparison between simulations and experiments provides helpful information to interpret the complicated experimental spectra. Furthermore, predictions of nuclear magnetic resonance spectra for novel materials can help drive the development of next generation ferroelectric materials.

1.1 Ferroelectrics

Perovskite-type ferroelectric materials have been the subject of intense research in the last ten years. New classes of perovskite ferroelectrics have been discovered with enhanced physical properties (such as piezoelectrics, dielectrics) and an ex-

panded region of technological applications [1–3]. With advances in theoretical and experimental techniques, it is now possible to pursue the microscopic origin of static and dynamic properties of these ferroelectrics. In the present work, first-principles calculations are performed on a few representative complex perovskite systems to study their local structure at the atomic level.

The discovery as well as some applications of ferroelectrics and related materials is discussed in detail by Lines and Glass [1], and briefly summarized here. In 1880, Pierre and Jacques Curie demonstrated for the first time that some crystals (such as tourmaline, quartz, topaz, cane sugar, and Rochelle salt) generate electric polarization under mechanical stress. These crystals were termed piezoelectrics, where "piezo" comes from the Greek "piezein", meaning to squeeze or press. In 1881, the converse piezoelectric effect was mathematically deduced by Lippmann from fundamental thermodynamic principles. Soon after, Pierre and Jacques Curie confirmed this effect experimentally, showing that piezoelectric crystals can also experience structural distortion when an external electric field is applied. In the present day, piezoelectric materials have been widely used in industrial applications [2, 3] such as sonar, high voltage sources, sensors, actuators, frequency standards, ultrasonic transducers, accelerometers, high frequency devices for medical imaging, and random access memories. They have also attracted a great deal of scientific research, both experimental and theoretical, aimed at understanding the microscopic origin of their properties and developing new materials.

A periodic crystal can be thought of as the same structural unit repeated infinitely in three dimensions. The possible configurations for all existing crystals are categorized into various point groups. There are a total of 32 unique point groups in nature. Eleven of them are classified as centrosymmetric types, which have a center of symmetry. Crystals with these point groups do not possess any polarity. The remaining twenty-one groups have no center of symmetry [4] and exhibit piezo-

electric properties [5], with the exception of the point group *432*. Among these twenty groups, ten of them contain more than one crystallographically unique direction axis. The other ten point groups have only one unique direction axis and are classified as pyroelectric. Ferroelectrics are those pyroelectric crystals which display spontaneous polarization even after the external electric field is removed. Their spontaneous polarization direction can be reorientated by applying an external electric field.

Many ferroelectric compounds (such as $KNbO_3$, $BaTiO_3$, $KTaO_3$, and $SrTiO_3$) belong to the perovskite family, named for the mineral perovskite, $CaTiO_3$. The perovskite family is a group of oxides with the general formula ABO_3 and ideally form a cubic structure, as shown in Fig. 1.1. The A atoms occupy the corners of the cube (examples include Pb, Ca, Sr, Ce, Na). The B atoms reside at the center of the cube, and normally have a small ionic radius and a high valence state with no occupied outer *d*-electron orbitals (for example, Sc^{3+}, Nb^{5+}, Ti^{4+}, Zr^{4+}, Ta^{5+}, W^{6+}). Oxygen atoms at the center of each face form an octahedron centered on the B site. The size difference between A and B atoms usually distorts the structure from perfect cubic to lower symmetries, such as rhombohedral, tetragonal and orthorhombic.

Some ferroelectric perovskite alloys can have more than one atomic species on the crystallographic sites. One well-known example is $PbMg_{1/3}Nb_{2/3}O_3$ (PMN), which consists of a 2:1 mixture of Nb^{5+} and Mg^{2+} cations on the B site, such that the overall B-site valence is +4 . Other examples include $Pb_{1-x}La_{2x/3}TiO_3$ with A-site alloying and $K_{1/3}Pb_{2/3}Zn_{2/9}Nb_{7/9}O_3$ with alloying on both the A and B sites.

Above the Curie temperature T_c, the crystal is in a paraelectric phase, often displaying an average cubic structure and no spontaneous polarization. When the temperature decreases below T_c, one or more ferroelectric phases appear, and the crystal structures are slightly distorted. For example, the Curie temperature of

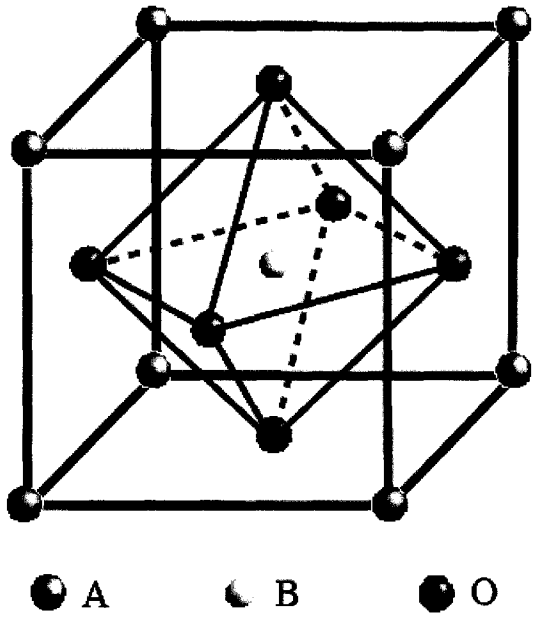

FIG. 1.1: Three-dimensional ABO_3 perovskite structure.

$BaTiO_3$ is 393 K, where the paraelectric phase transforms to a ferroelectric tetragonal phase. Between 278 K and 193 K, the stable ferroelectric phase becomes orthorhombic. Below 193 K, $BaTiO_3$ enters a rhombohedral phase [6]. At temperatures close to T_c, some anomalies appear for many thermodynamic properties. For example, the dielectric constant becomes very large near T_c for $BaTiO_3$.

Various theoretical approaches have been proposed to understand the behavior of ferroelectrics. Phenomenological Landau theory [1, 7] provides a macroscopic picture and can interpret many physical properties of ferroelectric materials, especially near the transition region. The soft mode concept was introduced by Cochran [8–10] to treat displacive ferroelectric transitions, where ions have small, continuous, and spontaneous displacements from their equilibrium positions. Later, the soft mode theory was developed to treat many displacive ferroelectric compounds, especially perovskite type materials. This method has been discussed in several references

[1, 8–11], and can be applied to high pressure effects [12]. Both phenomenological and soft mode theories achieved great success in many aspects understanding ferroelectrics (as reviewed by Samara [13]), but the origin of ferroelectricity at the atomic level was still unclear. In 1990, first-principles theory was found not only to be able to explain ferroelectric properties at a microscopic level, but also to be used in designing new materials [14]. Ever since, theory has made great progress in calculating structural properties, polarization, and piezoelectric response of ferroelectric ABO_3 compounds and solid solutions with considerable accuracy. The most widely used first-principles methods are based on density functional theory (DFT) framework. A more detailed introduction of DFT will be presented in the next chapter.

1.2 Lead-based complex perovskites

Among ferroelectric materials, lead based complex perovskites generally possess superior piezoelectric, ferroelectric, and dielectric properties. The piezoelectric response of these disordered alloys depends on their composition and possibly local ordering [13, 15, 16]. Many of these ferroelectrics with mixed valences form a special class known as relaxors. Some characteristic behaviors of relaxor ferroelectrics include a strong frequency dependent dielectric response, a diffusive dielectric permittivity maximum [17, 18], no long-range order, as well as the persistence of the mean polarization to temperatures well below that of the dielectric permittivity maximum. Relaxors often have large dielectric constants, and excellent electromechanical and piezoelectric properties. Consequently, relaxor ferroelectrics have attracted intense interest since their first discovery [19], and developed broad industrial applications, including strain actuators, sensors, capacitors, and transducers [2, 15, 20, 21]. Local and average structures of some relaxors have been studied by experimental techniques including x-ray and neutron diffraction [22–27], x-ray

diffuse scattering [28], infrared and Raman spectroscopy [29–37], nuclear magnetic resonance [38–45], high resolution transmission electron microscopy [46–48], and scanning force microscopy [49]. To explain some aspects of the various experimental results and the bulk properties of the relaxors, many theoretical models have been introduced [50–56]. However, the physical origin of the relaxor properties remains unclear, and the microscopic picture incomplete.

In the present work, local structures of the following solid solutions with various B site compositions and orderings are studied using first-principles method.

$Pb(Zr_{1-x}Ti_x)O_3$ (PZT) is a well-studied ferroelectric material whose B site is randomly occupied by either a Zr or Ti cation. Below 250°C and below 7% Ti, PZT is antiferroelectric; however, it becomes ferroelectric as the concentration of Ti (x) increases above 7%. As shown in the T-x phase diagram, Fig. 1.2, an almost vertical morphotropic phase boundary (MPB) at $x = 0.52$ separates the Zr-rich rhombohedral phase from the Ti-rich tetragonal phase, and large piezoelectric coupling occurs for compositions near the MPB. Noheda *et al.* discovered a monoclinic phase in PZT at low temperatures in a narrow compositional range at the MPB [57]. The macroscopic electric polarization rotation has been proposed as the origin of the large piezoelectric response in PZT and related materials. The polarization rotation mechanism was first proposed by Park and Shrout to explain the giant piezoelectric response in single-crystal piezoelectrics $(1-x)Pb(Zn_{1/3}Nb_{2/3})O_3{+}xPbTiO_3$ (PZN-PT) and $(1-x)Pb(Mg_{1/3}Nb_{2/3})O_3{+}xPbTiO_3$ (PMN-PT) [21]. Using first-principles calculations, Fu and Cohen [58] found that a large strain response is induced in $BaTiO_3$ by polarization rotation induced by a non-collinear applied electric field, while the strain response for collinear applied field was much smaller. They calculated a strain-vs-field curve that was qualitatively similar to that observed in PZN-8%PT [21]. The new monoclinic phase near the MPB of PZT suggested that the new phase might serve as a bridge between the tetragonal and rhombohedral

phases [57]. Subsequent effective Hamiltonian calculations by Bellaiche *et al.* [59] also showed this behavior. Wu and Krakauer [60] performed direct first-principles calculations of the piezoelectric response in PZT 50/50 and found greatly enhanced piezoelectric coefficients due to polarization rotation as a function of applied strain in the monoclinic phase. Similar polarization rotation has been observed in related materials such as PZN-8%PT [61] via an orthorhombic intermediate phase, and the existence of such intermediate phases has been established on general principles by Vanderbilt and Cohen [62]. Dmowski *et al.* [63] examined the local structure for PZT compositions near the MPB using atomic pair distribution functions (PDFs) obtained from Fourier transform of the neutron scattering structure factor. Based on comparisons with model PDFs, they found that the greatest change, with varying Ti/Zr composition, was the distribution in direction of the Pb displacements. The Ti rich local environments tending to have $< 100 >$ pseudocubic Pb displacements, while Zr rich environments tended to have $< 110 >$ pseudocubic Pb displacements.

$Pb(Sc_{1/2}Ta_{1/2})O_3$ (PST) belongs to the ABO_3 perovskite group, with a complex B site occupied by Sc^{3+} and Ta^{5+} cations with a 1:1 distribution. The degree of B site ordering can be controlled by specific heat treatments [65, 66]. When perfectly ordered, PST behaves as a normal ferroelectric; it becomes a relaxor when disordered. Thus, PST provides a good contrast to PZT, which is predominantly ferroelectric, and $Pb(Mg_{1/3}Nb_{2/3})O_3$ (PMN)-type relaxors which have 1:2 B site cation stoichiometry. Various experiments have been applied to study the structure and phase transitions of PST solid solutions. It was suggested by Chu *et al.* that the ferroelectric-relaxor transition is due to Pb vacancies introduced into the material [67]. The x-ray and neutron diffraction study of Dmowski *et al.* [27] revealed not only that significant local disorder exists in the ordered PST, but also that the local atomic [001] distortion is quite different from the average [111] crystallographic structure.

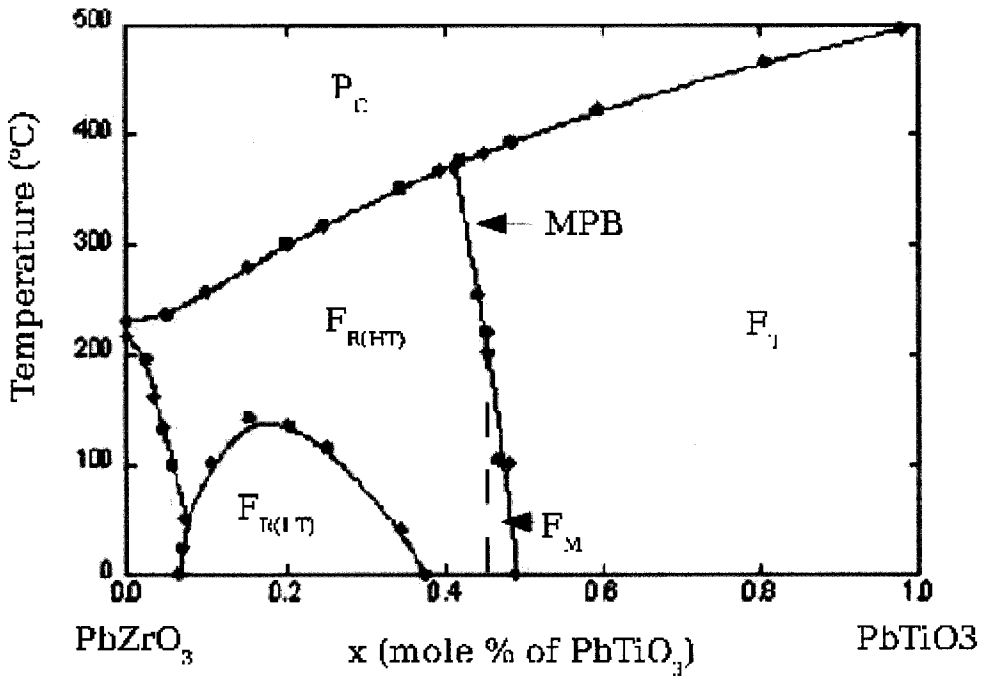

FIG. 1.2: PZT phase diagram after Jaffe *et al.* [64]

The PMN-type ferroelectrics with $Pb(B'B''B''')O_3$ perovskite structure, such as $Pb(Mg_{1/3}Nb_{2/3})O_3$-$PbTiO_3$ and $Pb(Mg_{1/3}Nb_{2/3})O_3$-$PbZrO_3$, are high performance relaxors of great technical importance. These solid solutions have been intensively studied in order to understand the microscopic origin of the macroscopic relaxor properties which remains unclear. But it is generally believed that the local structure and the chemical ordering play an essential role in the relaxor behaviors [15, 68].

$Pb(Sc_{2/3}W_{1/3})O_3$ (PSW) belongs to the PMN perovskite family, whose B-site cations have a 1:2 stoichiometric ratio. The B atoms in PSW obey the "random site" model [69], in which the B sites completely occupied by Sc^{3+} and those occupied by Sc^{3+} and W^{6+} in a 1:2 distribution form a rocksalt structure. The B-sites in PMN are occupied by Nb^{5+} and Mg^{2+} with a 1:2 distribution. In PSW and PMN, each B cation is surrounded by an inner-most O_6 cage, and a more distant B_6 octahedron. It has been shown by the x-ray diffuse scattering, neutron diffraction [70], and solid state NMR [43] experiments that the "random site" model [69] gives the best description of the short-range B-site disordering in PMN. More NMR measurements have been carried out to study the local structure of PMN-type alloys. For example, high field NMR magic angle spinning (MAS) ^{93}Nb spectra were recently presented for solid solutions of $(1-x)Pb(Mg_{1/3}Nb_{2/3})O_3+xPb(Sc_{1/2}Nb_{1/2})O_3$ [40], where distinct peaks were assigned according to the percentages of Mg, Sc, and Nb occupying the six nearest B-sites of the Nb atoms. The measurements [40, 43, 71, 72] suggested that the Nb quadrupole coupling parameters in PMN and related materials are sensitive to the number and identity of its nearest B neighbors as well as its displacement from the ideal cubic position. B-site environments in both PSW and PMN solid solutions have been studied using high-field NMR for ^{45}Sc and ^{93}Nb isotopes [40, 41, 44, 45]. However, inequivalent B-sites associated with various surrounding BO_6 configurations are overlapping and can not be fully distinguished from one another by NMR. It is thus of great interest to study the local environment of the B atoms

in PSW and PMN.

1.3 NMR quadrupole interaction

Many different experimental techniques have been used to study the local structural properties of ferroelectric materials, such as x-ray absorption fine structure spectroscopy, x-ray/neutron scattering pair distribution functions [63], and nuclear magnetic resonance (NMR) [40]. Recently, high field NMR measurements have shown great promise as a probe of the local structure of ABO_3 perovskite-based alloys. For example, NMR measurements of Ti spectra in $BaTiO_3$ have recently been used to argue for the coexistence of order-disorder and displacive components in the phase transition mechanism [73].

Several textbooks provide detailed information about NMR spectroscopy [3, 74–78], and some key features are summarized here. NMR is based on the coupling between the external magnetic field and the spin of the atomic nucleus (I). Spin is one of the intrinsic nuclear properties. A nucleus with odd mass number (A) possesses half-integral spin, for example: ^{1}H has spin 1/2, ^{17}O has spin of 5/2. A nucleus with both even A and charge (Z) has spin I = 0, examples of which are ^{16}O, ^{12}C, and ^{32}S. If the A of a nucleus is even, and Z is odd, the nucleus has an integral spin; for instance, ^{2}H and ^{14}N both have a spin of 1. Any nucleus with non-zero spin can be detected by NMR. Table 1.1 lists some magnetic properties of a few elements.

As a charged spinning particle, a nucleus would have a spin angular momentum, $\hat{J} = \hbar\hat{I}$, as well as a corresponding magnetic moment, $\hat{\mu} = \gamma\hbar\hat{I}$, where γ is the magneto-gyric ratio and is a constant for each particular nucleus. It is this magnetic moment that is manipulated in modern NMR experiments. In quantum mechanics, $\hat{J}$ and $\hat{I}$ are considered as operators. $\hat{I}^2$ has eigenvalue $I(I+1)$, and its component

TABLE 1.1: NMR magnetic properties for selected isotopes [42, 79].

Isotope	Spin I	Natural Abundance(%)	NMR Frequency in a 17.6157 T field (MHz)
^{1}H	1/2	99.98	750.000
^{2}H	1	0.015	115.128
^{6}Li	1	7.42	110.367
^{7}Li	3/2	92.58	291.474
^{17}O	5/2	0.037	101.676
^{23}Na	3/2	100	198.384
^{25}Mg	5/2	10.13	45.894
^{45}Sc	7/2	100	182.205
^{47}Ti	5/2	7.28	42.276
^{49}Ti	7/2	5.51	42.285
^{93}Nb	9/2	100	183.321
^{207}Pb	1/2	22.6	156.912

$\hat{I}_z$ has eigenvalue m, which is called the magnetic component quantum number with values of $-I, -I+1, ..., I-1, I$.

When placed in an external magnetic field $\mathbf{B_0}$, the magnetic moment of the nucleus interacts with the magnetic field. This interaction is called the Zeeman interaction, and the Hamiltonian operator can be written as:

$$\hat{H}_z = -\hat{\mu} \cdot \mathbf{B_0} = -\gamma \hat{J} \cdot \mathbf{B_0} = -\gamma \hbar \hat{I} \cdot \mathbf{B_0} = -\gamma \hbar B_0 \hat{I}_z. \tag{1.1}$$

The Zeeman interaction gives rise to a splitting of a series of m energy levels:

$$E_m = -\gamma \hbar m B_0. \tag{1.2}$$

A schematic of the energy levels for a nucleus with $I = 3/2$ is shown in Fig. 1.3. The energy difference between two adjacent energy levels is $\Delta E = \gamma \hbar B_0$. When the nucleus placed in a magnetic field absorbs this energy ΔE from radio-frequency

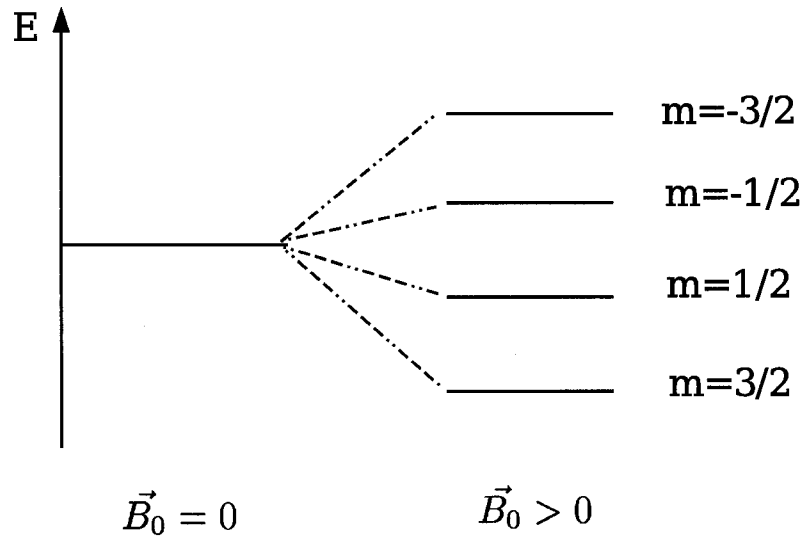

FIG. 1.3: Effect of Zeeman interaction on the energy level of a spin 3/2 nucleus.

irradiation, $h\nu_{\mathrm{L}}$, and transitions from one energy state to the next, the nucleus is described as being in resonance. Different atoms within a molecule or a crystal resonate at different frequencies for a given magnetic field. The frequency $\nu_{\mathrm{L}} = \gamma B_0/2\pi$ is known as the Larmor frequency. By detecting the resonance frequencies, the kind of atoms and those connected to them in a molecule or a crystal can be identified, and the structure of the molecule or the crystal can thus be determined.

Since the macroscopic sample with an ensemble of N nuclei is in thermodynamic equilibrium, the population of nuclei in each energy state is given by the Boltzmann distribution:

$$N_m = Ne^{-\frac{E_m}{k_B T}}, \tag{1.3}$$

where k_B is the Boltzmann constant and T is the absolute temperature. From this, the population difference can be obtained:

$$\Delta N = n_m - n_{m-1} \approx \frac{N\gamma\hbar B_0}{k_B T} = \frac{Nh\nu_L}{k_B T}. \tag{1.4}$$

For hydrogen nuclei ($I = 1/2$) in a magnetic field of 9.39 Tesla, with a Larmor frequency $\nu_L = 400$ MHz, and at room temperature 300 K, $h\nu_L/k_BT$ has a value of about 6×10^{-5}, which means that for every 300,000 hydrogen nuclei, the nuclear population difference between the two energy states is 1. It is this extremely small quantity that is responsible for the entire NMR signal, and thus high magnetic field and low temperature are desired.

In condensed matter, a nucleus experiences interactions with the local magnetic field, electric field gradients, and the lattice. The main contributions to the total Hamiltonian comes from the Zeeman interaction, quadrupole interaction, and magnetic shielding interaction. The origin of the electric quadrupole moment possessed by a nucleus arises from the nonspherical nuclear charge distribution. The nucleus thus has an electrostatic interaction with its environment when placed in an electrostatic field gradient. This interaction is dependent on the orientation of the nucleus. The nuclear electric quadrupole moment is important in solid state and chemical physics because many of the atoms or ions of interest have quadrupole moments. Fortunately, it is possible to use nuclei as microscopic probes to explore the internal electric field gradients in solids and molecules, which furthermore gives information about the local structure at the atomic scale.

Using the relative magnitude of the nuclear quadrupole interaction, NMR experiments can be roughly divided into two cases. The first is the low field case, where the nuclear quadrupole interaction is so large that NMR experiments can be performed only in zero or very small field. Studies of this case have been reviewed by Das and Hahn [80]. On the other hand, in high field NMR studies, the quadrupole interaction is much smaller than the Zeeman interaction, and can be treated as a perturbation. The high field case is widely applied in NMR experiments since it can improve the resolution of the spectrum and will be discussed here. A detailed review of the quadrupole interaction in NMR is given by Cohen and Reif [81], where

the quadrupole coupling Hamiltonian, H_Q, is derived. It describes the electrostatic interaction between a nucleus and its environment, and can be written as an integral over the whole nuclear volume:

$$\hat{H}_Q = \int \rho(x)V(x)d^3x, \tag{1.5}$$

where ρ is the electric charge density distributed over the nucleus and $V(x)$ is the electrostatic potential. The Hamiltonian can be expanded into a Taylor series:

$$\hat{H}_Q = \int d^3x\rho(x)\Big\{V\Big|_{\mathbf{x}=0} + \sum_{j=1}^{3}(\frac{\partial V}{\partial x_j})\Big|_{\mathbf{x}=0}x_j + \frac{1}{2}\sum_{j,k=1}^{3}(\frac{\partial^2 V}{\partial x_j \partial x_k})\Big|_{\mathbf{x}=0}x_j x_k + \cdots\Big\}. \tag{1.6}$$

Here the first term $\int d^3x\rho(x)V|_{\mathbf{x}=0} = ZeV|_{\mathbf{x}=0}$ is simply the electrostatic energy of a point nucleus, and by introducing the definition of the electric dipole moment $P_j \equiv \int d^3x\rho(x)x_j$, as well as that of the electric quadrupole moment tensor $Q'_{jk} \equiv \int d^3x\rho(x)x_j x_k$, the quadrupole Hamiltonian can be simplified to the form:

$$\hat{H}_Q = ZeV\Big|_{\mathbf{x}=0} + \sum_{j=1}^{3}P_j(\frac{\partial V}{\partial x_j})\Big|_{\mathbf{x}=0} + \frac{1}{2}\sum_{j,k=1}^{3}Q'_{jk}(\frac{\partial^2 V}{\partial x_j \partial x_k})\Big|_{\mathbf{x}=0} + \cdots. \tag{1.7}$$

Since all terms in this equation are either constant, or vanish due to the parity conservation of ground state wave functions, except for the third one, the quadrupole Hamiltonian eventually takes the form:

$$\hat{H}_Q = -\frac{1}{6}\sum_{j,k=1,3}Q_{jk}V_{jk}, \tag{1.8}$$

where $Q_{jk} \equiv 3Q'_{jk} - \delta_{jk}\sum_{j,k}Q'_{jk}$ is the traceless version of the electric quadrupole tensor Q'_{jk}, and $V_{jk} \equiv -\frac{\partial^2 V}{\partial x_j \partial x_k}$ is the electric field gradient tensor at the nuclear position, which can be represented by its three eigenvalues, $|V_{zz}| > |V_{yy}| > |V_{xx}|$.

H_Q describes the interaction between the nucleus and the electric field gradient around it, and can also be expressed as:

$$\hat{H}_Q = \frac{hC_Q}{4I(2I-1)}[(3\hat{I}_z^2 - \hat{I}^2) + \eta(\hat{I}_x^2 - \hat{I}_y^2)]. \tag{1.9}$$

In this expression, h is the Planck constant, $\hat{I}$, $\hat{I}_x$, $\hat{I}_y$, and $\hat{I}_z$ are quantum spin operators, η is the asymmetry parameter defined as $\eta \equiv \frac{V_{xx}-V_{yy}}{V_{zz}}$ (see Appendix A), and C_Q is the quadrupole coupling constant in frequency units, $C_Q \equiv \frac{eQV_{zz}}{h}$ where e is the proton charge, and Q is the nuclear electric quadrupole moment of the nucleus, usually expressed in barns (10^{-28} m^2). Both η and C_Q can be measured by NMR experiments.

The presence of the quadrupolar interaction results in a modification of the Zeeman splitting, and the $2I+1$ evenly spaced Zeeman levels are shifted to $2I$ distinguishable lines. Many of the nuclei in various ferroelectric solid solutions have half-integer spin larger than 1, including ^{17}O with $I = 5/2$, ^{45}Sc with $I = 7/2$, ^{93}Nb with $I = 9/2$, and many others. For such elements, their NMR spectra is dominated by the central $m = 1/2 \leftrightarrow -1/2$ transition, surrounded by $2I-1$ first-order satellite transition lines. Furthermore, their central transition is independent of the first-order perturbation [81]. In solid state NMR experiments, powder samples are normally used. Since the crystallites in powders are orientated randomly relative to the applied magnetic field, measured NMR quadrupole spectra (powder patterns), averaged over all possible orientations, are broadened. A characteristic central transition lineshape of the quadrupole interaction in a non-rotating (static) powder pattern is shown in fig. 1.4. The width and splitting of the lineshape are determined by the Larmor frequency, spin, as well as the electric field gradient that the nucleus experiences through C_Q and η. The width of the spectrum is proportional to the square of the V_{zz}, while the splitting of the peaks is controlled by the

value of η, with large η corresponding to small peak splitting.

In NMR experiments, nuclei exhibit other effects in addition to Zeeman and quadrupole interactions, including the screening of the applied magnetic field by the induced electric current, resulting in the NMR chemical shielding. On each chemically inequivalent crystalline site, the nucleus has its own electric field gradient and chemical shielding related lineshape broadening and shielding due to the anisotropy. This makes the assignment and structural interpretation very difficult. There are many ways and techniques in experiments to help remove part of the anisotropy and increase the resolution of the NMR spectrum, one is to use high magnetic fields. The Larmor frequency ν_{L} of a nucleus is proportional to the external magnetic field it is exposed to, and high ν_{L} provides larger frequency dispersion in the chemical shifts as well as less anisotropic broadening from the second-order quadrupolar interaction. Moreover, high magnetic field increases the signal intensity of the nucleus and consequently the signal-to-noise ratio of the NMR spectrum. Although these benefits from high field can improve the resolution, the magnitude of the magnetic field available for solid state NMR in practice is very limited (typically no higher than 20 Tesla). A common approach to increase the resolution in solid state NMR experiments is the Magic Angle Spinning (MAS) method, where the crystalline sample is rapidly spun at a fixed "magic" angle, $\theta = 54.74^{o}$, where $\cos^2\theta = 1/3$, with respect to the applied magnetic field. By applying MAS, interactions dependent on a geometric factor $(3\cos^2\theta - 1)$, such as the nuclear dipole-dipole interaction and part of the chemical shielding interaction, are averaged to zero. Hence, the normally wide NMR lines can be significantly narrowed and higher resolution can be achieved. However, MAS is not capable of completely removing all second-order quadrupolar broadening. To better separate the broadened and overlapped NMR signals of different chemical sites, multidimensional NMR techniques have been used [53, 83, 84]. In this technique, the NMR spectrum is extended from one frequency

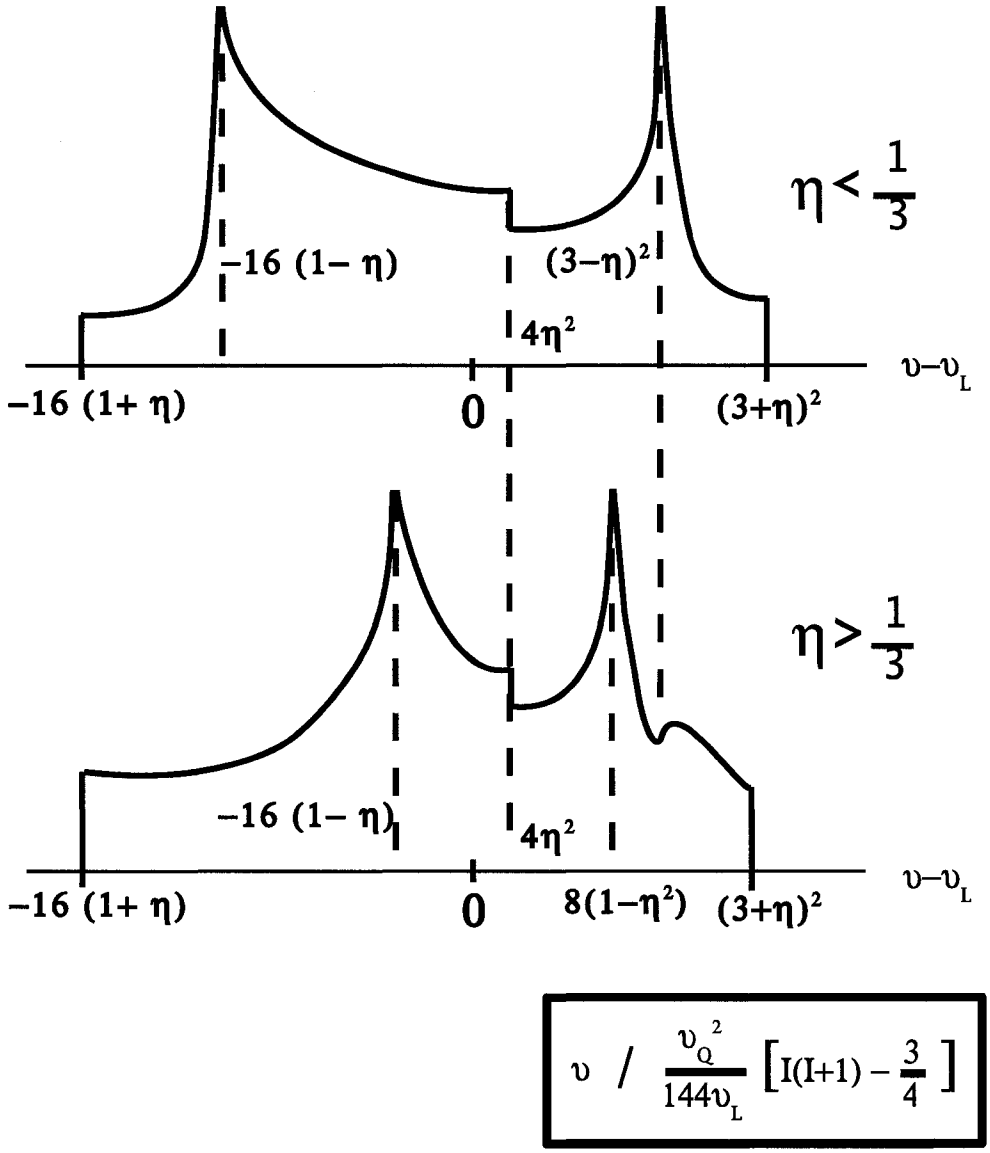

FIG. 1.4: Static powder pattern for the central transition of a nucleus with half-integer spin in the presence of NMR quadrupole effect. The frequencies are in units of $\frac{\nu_Q^2}{144\nu_0}[I(I+1)-3/4]$, where ν_L is the Larmor frequency of the nucleus, and $\nu_Q \equiv \frac{3C_Q}{2I(2I-1)}$ [82].

dimension to two or more frequency axes, and more structural information can be obtained.

Since the electric field gradient at a nucleus is very sensitive to local changes in electronic density, its effect on NMR spectra can serve as a useful probe of the atomic structure. But for a given nuclear isotope, each chemically inequivalent site produces its own electric field gradient induced NMR line-shifts and broadenings. In addition, each chemically inequivalent site will in general be subject to different chemical shifts of the NMR spectra due to screening of the applied magnetic field by induced electronic currents [82]. The combination of these effects can make it difficult to assign spectra arising from inequivalent sites. It is thus of considerable interest to provide theoretical guidance to interpret these spectra. From the calculated electric field gradients, the NMR quadrupolar spectra of static powder patterns can be simulated (see Appendix A), and be used to help understand the experimental spectra.

1.4 Electric field gradient (EFG)

The electric field gradient (EFG) is a second-rank tensor, defined as the second partial spatial derivative of the Coulomb potential V(r) at the nuclear site,

$$V_{ij} = \frac{\partial^2 V}{\partial x_i \partial x_j} - \frac{1}{3}\delta_{ij}\nabla^2 V. \tag{1.10}$$

It is a symmetric and traceless tensor, normally represented by its largest eigenvalue and the asymmetry parameter η. By convention, the three eigenvalues of the EFG tensors are ordered as $|V_{zz}| > |V_{yy}| > |V_{xx}|$, and η is expressed by:

$$0 < \eta = \frac{V_{xx} - V_{yy}}{V_{zz}} < 1. \tag{1.11}$$

TABLE 1.2: Quadrupole moments of some nuclei [85, 86]

Nucleus	Q(barn)
^{2}H	+0.002860(15)
^{6}Li	-0.00083(8)
^{17}O	-0.02578
^{23}Na	+0.1006(20)
^{25}Mg	+0.201(3)
^{45}Sc	-0.22(1)
^{93}Nb	-0.32(2)

TABLE 1.3: Sternheimer factors for some ions both in free states and in crystals.

Nucleus	γ_∞ free[87]	γ_∞ free[88]	γ_∞ crystal[88]
Li^{+}	0.262	0.249	0.255
O^{2-}	0.0892	-	-13.785
Na^{+}	-5.59	-5.261	-5.452
Mg^{2+}	-3.76	-3.503	-4.118
Sc^{3+}	-13.6	-11.388	-23.104
Rb^{+}	-52.3	-47.664	-52.781
Sr^{2+}	-40.4	-38.893	-47.828
Y^{3+}	-34.8	-31.020	-51.985
Zr^{4+}	-31.1	-	-
Nb^{5+}	-29.5	-	-49[42]

Since the EFG tensor is traceless, V_{zz} and η determine all three eigenvalues.

One way to obtain EFG information is from observed NMR quadrupole coupling constants, C_Q:

$$V_{zz} = \frac{hC_Q}{eQ}. \tag{1.12}$$

The nuclear quadrupole moment Q for most quadrupole isotopes can be measured by various experimental techniques (atomic beam, Coulomb excitation reorientation, laser resonance, and muonic x-ray hyperfine structure for example). The Q values of most nuclei are well documented [85, 86], several of them are listed in Table 1.2.

The EFG can also be determined theoretically. The earliest approach is through the simple point-charge model [89]. In this model, ions are represented by point charges at the respective lattice sites. The EFG on a nucleus is calculated from point-ion electrostatic potential of surrounding charges. The point-charge model significantly underestimates the magnitude of EFGs since it neglects the on-site anisotropic charge distribution. In the Steinheimer approach, the total EFG is obtained by:

$$V_{zz} = (1 - \gamma)V_{zz}^{\mathrm{Ext}}, \tag{1.13}$$

where V_{zz}^{Ext} is the point-charge EFG. The Steinheimer parameter γ is obtained from quantum-mechanical calculations of the isolated atom. The γ values for some selected nuclei are listed in Table 1.3.Nowadays, the point-charge and Steinheimer method are rarely used. Instead, first-principles methods can obtain EFGs directly with high accuracy.

All-electron first-principles approaches such as the linearized augmented plane wave (LAPW) method are usually used to calculate EFGs [90–96]. In the LAPW method, space is divided into two regions, a region close to the nucleus and a more distant bonding region between nuclei. In the region close to the nucleus, correct atomic-like solutions are found for all wave functions. These wave functions yield accurate Coulomb potential at the nucleus, which is needed to obtain EFGs. The difficulty with widely used pseudopotential methods is the incorrect form of the pseudo-wave-functions near the atomic nuclei. Pseudo wave functions lack the nodal features of the true valence wave functions. This arises from orthogonality of the valence to the core-electron states, which are absent in a pseudopotential calculation. This can result in sizable errors, since the EFG depends sensitively on the charge density near the nucleus. Recently, EFGs have been successfully calculated using the the projector augmented wave (PAW) method [97]. While the PAW method is

sometimes regarded as a planewave pseudopotential approach, it is essentially an all-electron method that retains the correct nodal properties of the valence wave functions near the nucleus. First-principles methods have been applied successfully to many materials [90–97]. First-principles all-electron methods are thus a reliable means to determine EFGs in perovskite alloys.

This work presents first-principles all-electron density functional theory calculations of EFGs for structural models of $Pb(Zr_{1/2}Ti_{1/2})O_3$ (PZT), $Pb(Sc_{1/2}Ta_{1/2})O_3$ (PST), and $Pb(Sc_{2/3}W_{1/3})O_3$ (PSW), and $Pb(Mg_{1/3}Nb_{2/3})O_3$. Calculations were carried out as a function of B-site chemical ordering, applied strain, and imposed symmetry. Using the first-principles LAPW method, EFGs are obtained for the four solid solutions. NMR quadrupole spectra are generated in order to help interpret experiments and guide further NMR research. In Chapter 2, the LAPW method will be discussed in some detail. In Chapter 3 and 4, detailed research results on PZT, PST, PSW, and PMN will be presented and discussed, respectively. Chapter 5 presents a summary of this work.

Chapter 2

Methodology

With the rapid growth of computer power in the last few decades, first-principles quantum-mechanics calculational techniques have become an indispensable tool in condensed matter physics, due to their ability to provide very accurate theoretical results. In the first-principles approach, there are no adjustable parameters, thus no experimental information is required as input. This not only allows first-principles methods to help interpret experimental results, but also enables them to provide guidance to experiments by predicting properties under some unachievable laboratory conditions [98] or of new materials which have yet to be synthesized [99]. In this chapter, one of the most successful first-principles methods, the density functional theory (DFT), will be briefly introduced, as well as the applications of the DFT in 3 dimensional periodic systems and the method used in the electric field gradient calculations under the DFT framework.

2.1 Density functional theory (DFT)

In areas including chemistry [100], biochemistry [101], polymers [102], nanotechnology, and condensed matter physics, DFT has been very successfully applied

to study properties of ground state and excited states.

In quantum mechanics, the time-independent Schrödinger equation governs many physical properties of materials,

$$\hat{H}\Psi = E\Psi. \tag{2.1}$$

Here $\hat{H}$ is the Hamiltonian operator with eigenvalue E (the total energy of the system). The eigenstate Ψ is the many-body wave function, which determines the nature of the system. For any system with a collection of interacting nuclei and electrons, the exact non-relativistic many-body Hamiltonian can be written as:

$$\begin{aligned} \hat{H} \;=\; & -\frac{1}{2}\sum_i \frac{\nabla^2_{\mathbf{R}_i}}{M_i} - \frac{1}{2}\sum_j \nabla^2_{\mathbf{r}_j} - \sum_{i,j}\frac{Z_i}{|\mathbf{R}_i - \mathbf{r}_j|} \\ & + \frac{1}{2}\sum_{j\neq j'}\frac{1}{|\mathbf{r}_j - \mathbf{r}_{j'}|} + \frac{1}{2}\sum_{i\neq i'}\frac{Z_i Z_{i'}}{|\mathbf{R}_i - \mathbf{R}_{i'}|}, \end{aligned} \tag{2.2}$$

where M_i is the mass of the nucleus at position $\mathbf{R}_i$ with charge Z_i, and r's are the positions of electrons. The terms in Eq. (2.2) represents the kinetic energy of the nuclei, the kinetic energy of the electrons, the Coulomb interaction between nuclei and electrons, between different electrons, and between different nuclei, respectively.

In the Born-Oppenheimer approximation [103], the nuclear positions can be regarded as fixed, since the nuclei are much heavier than the electrons and move much more slowly. The kinetic energy of the nuclei is neglected and the Coulomb interaction between the nuclei is simply a constant. Furthermore, the electrons experience an external potential, which depends parametrically on the nuclear positions. The resulting many-body electronic Hamiltonian can be written as the sum of the kinetic energy, the electron-electron interaction, the potential energy due to the external potential (e.g. the nuclear-electron potential and possibly other external fields), and

a constant which includes the nuclear-nuclear repulsion:

$$\hat{H} = \hat{T} + \hat{V}_{\text{ee}} + \hat{V}_{\text{ext}} + \frac{1}{2}\sum_{i \neq i'} \frac{Z_i Z_{i'}}{|\mathbf{R}_i - \mathbf{R}_{i'}|}, \tag{2.3}$$

where

$$\hat{V}_{\text{ext}} = \sum_j V_{\text{ext}}(\mathbf{r}_j). \tag{2.4}$$

The form of the first two terms are universal for any system, while the external potential, depends on the system in question.

2.1.1 Hohenberg and Kohn theorems

Even after applying the Born-Oppenheimer approximation, the Schrödinger equation is still a difficult problem to solve. The advantage of DFT is that it can exactly map the complicated many-body problem onto a non-interacting system. The foundation of DFT is the Hohenberg and Kohn (HK) theorems, which make DFT an exact method in principle for treating many-body systems. A concise account of the HK theorems and the Kohn Sham method is given by R. Martin [104], which will be briefly paraphrased here.

The first HK theorem states that the external potential for any system of interacting particles, $V_{\text{ext}}(\mathbf{r})$, is determined uniquely by the ground state particle density $n_0(\mathbf{r})$ up to a constant. Since V_{ext} uniquely determines $\hat{H}$ in Eq. (2.3), this implies that $n_0(\mathbf{r})$ determines not only the ground state E_0, but also all excited states.

The second Hohenberg and Kohn theorem further indicates that the ground state energy for a many-particle system is the global minimum of the total energy, and the charge density which minimizes the total energy is the exact ground state charge density.

Consequently, all properties of the system are fully determined by the charge

density $n(\mathbf{r})$, and the values of all observables can be written as functionals of $n(\mathbf{r})$. The ground state energy E_0 and the energy $E_{\rm HK}$ take the form:

$$\begin{aligned} E_0[n_0(\mathbf{r})] \leqslant E_{\rm HK}[n(\mathbf{r})] &= \langle\Psi|\hat{T}|\Psi\rangle + \langle\Psi|\hat{V}_{\rm ee}|\Psi\rangle + \langle\Psi|\hat{V}_{\rm ext}|\Psi\rangle \\ &= T[n(\mathbf{r})] + E_{\rm ee}[n(\mathbf{r})] + \int d^3r V_{\rm ext}(\mathbf{r})n(\mathbf{r}) \\ &\equiv F_{\rm HK}[n(\mathbf{r})] + \int d^3r V_{\rm ext}(\mathbf{r})n(\mathbf{r}), \end{aligned} \tag{2.5}$$

where the Hohenberg and Kohn functional $F_{\rm HK}[n(\mathbf{r})] \equiv T[n(\mathbf{r})] + E_{\rm ee}[n(\mathbf{r})]$ is a universal functional since it only contains the kinetic energy of the electrons and the electron-electron internal potential energy, and no information related to the nuclear configuration. The ground state charge density of an interacting many-particle system can be obtained by minimizing the total energy E_{HK} in Eq. (2.5), but the exact form of the universal functional $F_{\rm HK}$ is unknown.

2.1.2 Kohn-Sham theory

Although the HK theorems prove that the density is sufficient in principle for all ground state properties, no practical method has been specified. The Kohn-Sham approach [105] provides a useful framework for practical approximations. The central idea of this approach is to replace the original complicated many-body system obeying the Hamiltonian of Eq. (2.3) by a new non-interacting auxiliary system.

In an independent-particle system with N electrons, the orbital of each electron obeys the single-particle Schrödinger equation:

$$\hat{H}_{\rm s}\psi_i(\mathbf{r}) = \left[-\frac{1}{2}\nabla_i^2 + V_{\rm s}(\mathbf{r})\right]\psi_i(\mathbf{r}) = \epsilon_i\psi_i(\mathbf{r}). \tag{2.6}$$

The density of this non-interacting system is defined as:

$$n(\mathbf{r}) = \sum_{i}^{occ} |\psi_i(\mathbf{r})|^2, \tag{2.7}$$

where the sum is over the N lowest occupied states, and the density satisfies the constraint:

$$\int n(\mathbf{r}) d\mathbf{r} = N. \tag{2.8}$$

The kinetic energy of the auxiliary system, T_s, takes the form:

$$T_s = -\frac{1}{2}\sum_{i}^{N} \langle \psi_i | \nabla^2 | \psi_i \rangle = \frac{1}{2}\sum_{i}^{N} |\nabla \psi_i|^2. \tag{2.9}$$

It is useful to define the Hartree energy, which describes the classical Coulomb interaction between the charge density and itself:

$$E_{\mathrm{H}}[n] = \frac{1}{2}\int \frac{n(\mathbf{r}')n(\mathbf{r})}{|\mathbf{r}' - \mathbf{r}|} d^3r' d^3r, \tag{2.10}$$

Thus ground state total energy of the many-body system can be written in terms of a non-interacting system, whose charge density is the same as that of the interacting system:

$$E_{\mathrm{KS}} = T_s + \int d^3r V_{\mathrm{ext}}(\mathbf{r}) n(\mathbf{r}) + E_{\mathrm{H}}[n] + E_{\mathrm{xc}}[n]. \tag{2.11}$$

where the (so far unknown) exchange correlation energy E_{xc} is defined as:

$$E_{\mathrm{xc}}[n] \equiv (T[n(\mathbf{r})] - T_s) + (E_{\mathrm{ee}}[n(\mathbf{r})] - E_{\mathrm{H}}[n]). \tag{2.12}$$

Here $T[n(\mathbf{r})]$ is the actual kinetic energy of the many-body system. The energy E_{xc} contains all the exchange and correlation effects in the interacting system which are

omitted by the single-particle energy. Since it is a sum of differences, its effects are reduced compared to $F_{\rm HK}$ in Eq. (2.5). The ground state energy can be obtained by following the Hohenberg and Kohn theorem, namely, minimizing the total energy in Eq. (2.11) with respect to the density $n(\mathbf{r})$. To satisfy the charge conservation requirement (Eq. 2.8), this minimization is equivalent to:

$$\frac{\delta E_{\rm HK}}{\delta \psi_i^*(\mathbf{r})} = \frac{\delta T_{\rm s}}{\delta \psi_i^*(\mathbf{r})} + \left[V_{\rm ext}(\mathbf{r}) + \frac{\delta E_{\rm H}}{\delta n(\mathbf{r})} + \frac{\delta E_{\rm xc}}{\delta n(\mathbf{r})} \right] \frac{\delta n(\mathbf{r})}{\delta \psi_i^*(\mathbf{r})} = 0, \tag{2.13}$$

under the orthonormalization constraint:

$$\langle \psi_i^*(\mathbf{r}) | \psi_j(\mathbf{r}) \rangle = \delta_{ij}. \tag{2.14}$$

From the definitions of T_s and $n(\mathbf{r})$ in Eq. (2.9) and Eq. (2.7), the functional derivatives in Eq. (2.13) can be obtained:

$$\frac{\delta T_{\rm s}}{\delta \psi_i^*(\mathbf{r})} = -\frac{1}{2}\nabla^2 \psi_i(\mathbf{r}), \tag{2.15}$$

$$\frac{\delta n(\mathbf{r})}{\delta \psi_i^*(\mathbf{r})} = \psi_i(\mathbf{r}). \tag{2.16}$$

These lead to the Kohn-Sham single-particle Scrödinger-like equations:

$$(H_{\rm KS} - \varepsilon_i)\psi_i(\mathbf{r}) = 0. \tag{2.17}$$

Here ε_i's are the eigenvalues, $\psi_i(\mathbf{r})$'s are the Kohn-Sham orbitals, and the effective Hamiltonian $H_{\rm KS}$ is:

$$H_{\rm KS} = -\frac{1}{2}\nabla^2 + V_{\rm eff}, \tag{2.18}$$

with

$$V_{\rm eff}(\mathbf{r}) = V_{\rm ext} + V_{\rm H} + V_{\rm xc}, \tag{2.19}$$

in which $V_{\rm H}$ and $V_{\rm xc}$ are defined separately as:

$$V_{\rm H}(\mathbf{r}) = \int \frac{n(\mathbf{r}')}{|\mathbf{r}-\mathbf{r}'|} d\mathbf{r}', \tag{2.20}$$

$$V_{\rm xc} = \frac{\delta E_{\rm xc}[n(\mathbf{r})]}{\delta n(\mathbf{r})}. \tag{2.21}$$

The electronic charge density $n(\mathbf{r})$ is determined by the single-particle orbitals as shown in Eq. (2.7). Although the $\psi_i(\mathbf{r})$'s yield the same density as the real interacting system, the KS orbitals generally don't have any physical meaning. Furthermore, the total energy of the real system is not a simple sum of all single-particle eigenvalues. Eq. (2.11) can be re-written as:

$$E_{KS} = \sum_{i}^{\rm occ} \varepsilon_i - \frac{1}{2}\int \frac{n(\mathbf{r})n(\mathbf{r}')}{|\mathbf{r}-\mathbf{r}'|} d\mathbf{r}d\mathbf{r}' + E_{\rm xc}[n(\mathbf{r})] - \int \frac{\delta E_{\rm xc}[n(\mathbf{r})]}{\delta n(\mathbf{r})} n(\mathbf{r}) d\mathbf{r}. \tag{2.22}$$

When the density of the system is known, the Hamiltonian in the KS equations can be exactly determined if $E_{\rm xc}[n(\mathbf{r})]$ is known. It is evident that KS equations (2.17) must be solved self-consistently. Starting with a guess of the density n_0, the KS Hamiltonian $H_{\rm KS}$ is constructed from this density n_0; solving the KS equations results in a set of KS orbitals $\psi_i(\mathbf{r})$. An output density $n_{\rm out}$ is then created from these orbitals. If $n_{\rm out}$ differs from n_0 (and it most likely does) a new input density $n_{\rm in}$ is generated from $n_{\rm out}$. The self-consistent circle starts again with the new density $n_{\rm in}$. This procedure continues until the difference between the output density and the previous input density reaches a convergence limit.

2.1.3 Widely used exchange-correlation approximations

If the exchange correlation functional is known, the KS equations can be exactly solved for the interacting system. Unfortunately, the exact form of $E_{\rm xc}$[n] is not known, and some approximation is needed. One of the most successful and the most

natural (and also the simplest) way to approximate exchange-correlation effects is the so-called Local Density Approximation (LDA), first proposed by Kohn and Sham in 1965 [105]. In this approximation, the exchange-correlation energy depends only on the density at $\mathbf{r}$:

$$E_{\rm xc}^{\rm LDA}[n(\mathbf{r})] = \int d^3r n(\mathbf{r})\epsilon_{\rm xc}(n(\mathbf{r})), \tag{2.23}$$

where the energy density $\epsilon_{\rm xc}(n(\mathbf{r}))$ is of an homogeneous electron gas with density $n(\mathbf{r})$. The potential $V_{\rm xc}$ then takes the form:

$$V_{\rm xc}^{\rm LDA}[n(\mathbf{r})] = \frac{\delta E_{\rm xc}^{\rm LDA}}{\delta n(\mathbf{r})} = \epsilon_{\rm xc}^{\rm hom}[n] + n(\mathbf{r})\frac{\delta \epsilon_{\rm xc}^{\rm hom}[n]}{\delta n}. \tag{2.24}$$

There are many approximations for the exchange-correlation energy per electron, $\epsilon_{\rm xc}^{\rm hom}[n]$, in a homogeneous gas with density n. In this work, the Hedin-Lunquist LDA functional [106]is applied.

The LDA is surprisingly successful in describing the ground state geometries and dynamic properties (such as phonon frequencies) for atomic and molecular systems whose density can change rapidly [107], and it has long been the standard for first-principles calculations. Other widely used approximations include the general gradient approximation (GGA) [108–110] in which the exchange-correlation energy density is a function of both the density and the magnitude of its gradient $\epsilon_{\rm xc}(n, |\nabla n|)$, the optimized effective potential (OEP) method [111–113] where the Hartree-Fock exchange potential is replaced by a functional of the local density n, and the hybrid method [114–116] where the exchange-correlation energy is a linear combination of the Hartree-Fock energy and $E_{\rm xc}$ from LDA or GGA.

2.1.4 Solving the Kohn Sham equations with basis set

There are various ways to solve the Kohn-Sham equations (2.17). Almost all first-principles methods choose to apply the basis set expansion, in which the Kohn-Sham orbitals are expressed by a set of basis functions φ_j's and expansion coefficients c_{nj}'s:

$$\psi_n(\mathbf{r}) = \sum c_{nj}\varphi_j(\mathbf{r}). \tag{2.25}$$

By inserting Eq. (2.25) into the Kohn-Sham equations (2.17), and operating φ_i^* from the left of the Kohn-Sham equation, it can be rewritten as a matrix equation:

$$\sum_j (H_{ij} - \varepsilon_n O_{ij}) c_{nj} = 0. \tag{2.26}$$

Here H_{ij}'s are the Hamiltonian matrix elements $H_{ij} = \langle\varphi_i|\hat{H}|\varphi_j\rangle$, O_{ij}'s are the overlapping matrix elements $O_{ij} = \langle\varphi_i|\varphi_j\rangle$, and c_{nj} is a column vector. The matrix equation (2.26) can be directly diagonalized and thus result in all the eigenvalues, ε's, as well as all the corresponding eigenvectors, c_{nj}'s. Eq. (2.26) is essentially the Euler-Lagrange equation, which minimizes the ground state energy E_0 in Eq. (2.11), when the KS orbitals are expanded as in Eq. (2.25).

In general, any linearly independent set of functions can be used as a basis set; the most common in DFT based methods are Gaussian type orbitals, plane waves, and the linearized augmented plane wave (LAPW) functions.

2.2 DFT applications to periodic systems

The DFT-LDA approach has been widely used to determine the ground state electronic properties of solids. In periodic systems, Bloch's theorem simplifies the solution of the KS orbitals. To obtain electric field gradients, all-electron wave func-

tions are needed since EFGs are dependent on the value of the electronic potential at the nucleus. Because of this, the all-electron linearized augmented plane wave (LAPW) method is used in the present work to calculate the wave functions. However, it can be time-consuming to optimize the structural configuration of a given system by using the LAPW method, especially for large unit cells. To achieve better scaling in structural relaxation, the plane wave pseudopotential method is applied in the present work. A detailed review of this method has been given by Pickett [117]. The calculated residual forces on atoms in the same relaxed atomic structures by the pseudopotential and LAPW methods usually agree well with each other.

In this section, the structural relaxation procedure and the **k**-point sampling technique will be first discussed, followed by a brief introduction to the plane wave pseudopotential method and the LAPW method. In the next section, the calculation of the electric field gradient will be described in detail.

2.2.1 Structural relaxation

Now the total energy for a given nuclear configuration **R** can be calculated, the next task is to find the structure that yields the true ground state. The use of analytic derivatives (i.e. atomic forces) facilitates this. According to the Hellmann-Feynman (HF) theorem [118, 119], $\frac{\partial E}{\partial \lambda} = \langle \psi_\lambda | \frac{\partial H}{\partial \lambda} | \psi_\lambda \rangle$ (here λ is some parameter of interest, **R** for instance), the atomic forces are just the derivatives of the total energy with respective to the atomic position R_i:

$$\begin{aligned} F_i &= -\frac{\partial E_{\rm tot}(\mathbf{R})}{\partial R_i} = -\frac{\partial}{\partial R_i}(E_{\rm DFT}(\mathbf{R}) + E_{\rm ion-ion}(\mathbf{R})) \\ &= -\frac{\partial}{\partial R_i}\Big(T_{\rm s}[n(\mathbf{r})] + E_{\rm H}[n(\mathbf{r})] + E_{\rm xc}[n(\mathbf{r})] \\ &\quad + \int n(\mathbf{r}) V_{\rm ext}(\mathbf{r}) d^3r + E_{\rm ion-ion}(\mathbf{R})\Big). \end{aligned} \tag{2.27}$$

For the exact ground state, only the terms which depend explicitly on the atomic positions contribute to the force:

$$F_i = -\int d^3r n(\mathbf{r}) \frac{\partial V_{\text{ext}}(\mathbf{r})}{\partial R_i} - \frac{\partial E_{\text{ion-ion}}}{\partial R_i}. \tag{2.28}$$

The HF forces tend to move the ions toward their equilibrium positions, thus they can be used to find the atomic configuration of a local energy minimum.

Structural relaxations using a plane wave basis in the present work were obtained through the use of the ABINIT code [120].

2.2.2 k-point sampling

Although the Bloch's theorem allows the calculations to be carried out within one unit cell of a finite size instead of the whole infinite periodic solid, the number of **k** inside the first Brillouin zone (BZ) (defined as the Wigner-Seitz primitive cell of the reciprocal lattice, or as the set of points in **k**-space that can be reached from the origin without crossing any Bragg plane) is still infinite in principle. Considering that the wavefunctions at those **k**-points close to each other are very similar, it is possible to discretize the sampling in a **k**-space. There are different methods to specify such a set of discrete **k**-points so that they can appropriately sample the BZ, for example the tetrahedron method [121–123] and the special points method [124–126], which is applied in the present work. In the special points methods, a weight is assigned to each **k**-point, and the locations and the weights of these **k**-points are not dependent on the band energies. Hence, an integrated function, such as the charge density $n(\mathbf{r})$, can be expressed as a sum over the chosen **k**-points:

$$n(\mathbf{r}) = \sum_n \frac{1}{(2\pi)^3} \int_{\text{BZ}} \psi^*_{nk}(\mathbf{r}) \psi_{nk}(\mathbf{r}) d\mathbf{k} = \sum_n \sum_j w_j \psi^*_{nk_j}(\mathbf{r}) \psi_{nk_j}(\mathbf{r}), \tag{2.29}$$

where the ω_j's are the quadrature weighting factors. And the error introduced by finite **k**-point sampling can easily be monitored by using denser **k**-point grids.

2.2.3 Plane wave basis functions for crystals

In a periodic crystal, the potential is also periodic:

$$V(\mathbf{r}+\mathbf{R}) = V(\mathbf{r}), \tag{2.30}$$

where **R** is any lattice vector. By Bloch's theorem [127], the eigenfunctions, ψ_{nk}'s , of the Kohn-Sham equation in this system can be expressed as:

$$\psi_{nk}(\mathbf{r}) = u_{nk}(\mathbf{r})e^{i\mathbf{k}\cdot\mathbf{r}}. \tag{2.31}$$

Here, **k** is the wave vector, different eigenfunctions with the same **k** are distinguished by the band index n, and $u_{nk}(\mathbf{r})$ is a periodic function. This theorem essentially reduces the calculation of KS orbitals to a single unit cell, since the wavefunctions outside this region can be obtained by:

$$\psi(\mathbf{r}+\mathbf{R}) = e^{i\mathbf{k}\cdot\mathbf{R}}\psi(\mathbf{r}). \tag{2.32}$$

The periodic function $u_{nk}(\mathbf{r})$ in Eq. (2.31) is most easily expanded in plane waves:

$$u_{nk}(\mathbf{r}) = \sum_{\mathbf{G}} c_{nk,\mathbf{G}} e^{i\mathbf{G}\cdot\mathbf{r}}, \tag{2.33}$$

where **G**'s are reciprocal lattice vectors. The Kohn-Sham orbitals thus take the form:

$$\psi_{nk}(\mathbf{r}) = \sum_{\mathbf{G}} c_{n,\mathbf{k}+\mathbf{G}} e^{i(\mathbf{k}+\mathbf{G})\cdot\mathbf{r}}. \tag{2.34}$$

The periodic potential $V_{\text{eff}} = V_{\text{ext}} + V_{\text{H}} + V_{\text{xc}}$ can also be expanded as a Fourier sum in the reciprocal space over the lattice vector $\mathbf{G}$:

$$V_{\text{eff}}(r) = \sum_{\mathbf{G}} V_{\mathbf{G}} e^{i\mathbf{G}\cdot\mathbf{r}}. \tag{2.35}$$

By inserting Eq. (2.34) and Eq. (2.35) into Eq. (2.17), operating from the left with $e^{-i(\mathbf{G}+\mathbf{k})\cdot\mathbf{r}}$, and integrating over $\mathbf{r}$, the Kohn-Sham equations can be rewritten as a matrix equation:

$$\sum_{\mathbf{G}'}[\frac{1}{2}|\mathbf{k}+\mathbf{G}|^2\delta_{\mathbf{G}\mathbf{G}'} + V_{\text{eff}}(\mathbf{G}-\mathbf{G}')]c_{n,\mathbf{k}+\mathbf{G}'} = \varepsilon_n c_{n,\mathbf{k}+\mathbf{G}} \tag{2.36}$$

By diagonalizing the Hamiltonian matrix, H ($\mathbf{G}$, $\mathbf{G}'$), whose elements are given by the terms in brackets in Eq. (2.36), the eigenvalues, ε_n, and the Kohn-Sham orbitals can be obtained, as well as other ground state properties, charge density, and total energy, for instance.

A key advantage of the plane wave (PW) basis is its ability to exploit fast Fourier transforms. This leads to $O(NM \ln M)$ for unit cells with less than about 100 atoms, compared to $O(M^3)$ for diagonalization. A disadvantage is the incorrect behavior of the wave function ψ_{PW} near the nucleus.

To keep the number of plane waves tractable, the highly localized core electron states must be removed from the spectrum of $\hat{H}$ using a pseudopotential. The corresponding pseudo-wave-function is much smoother and nodeless for $r < r_c$ (also known as the "core radius"), and matches the real wave function exactly beyond r_c. Both the pseudopotential and the pseudo-wave-function are shown schematically in Fig. 2.1.

The choice of the pseudopotential that exactly reproduces the valence properties is not unique. One of the most widely used classes is known as the norm-conserving

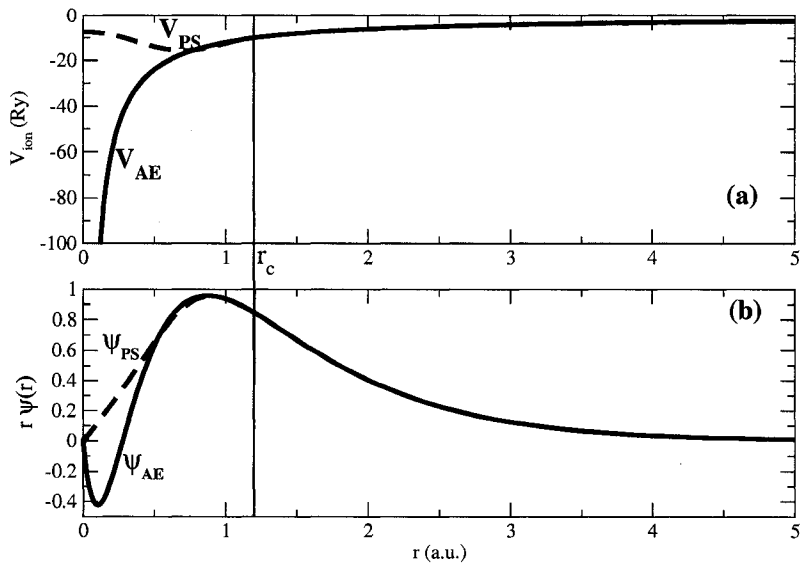

FIG. 2.1: Panel (a) and (b) show the full featured all-electron (AE) potential (solid curve) versus pseudopotential (dashed curve) and their corresponding wave functions, respectively.

pseudopotentials, proposed by Hamann, Schlüter, and Chiang [128]. This type of pseudopotential has the following properties:

a). For a specific reference configuration, the eigenvalues of the pseudo valence states agree with those of the real all-electron (AE) states:

$$\varepsilon^{\mathrm{PS}} = \varepsilon^{\mathrm{AE}} \tag{2.37}$$

b). The logarithmic derivatives and the first energy derivatives of the pseudo and real wave functions match with each other beyond r_{c}.

c). The integrated pseudo and the real charge densities are equal, leading to the norm-conservation constraint:

$$\int_0^{r_{\mathrm{c}}} |\psi^{\mathrm{PS}}|^2 d^3r = \int_0^{r_{\mathrm{c}}} |\psi^{\mathrm{AE}}|^2 d^3r \tag{2.38}$$

Since the pseudopotential is generated for a chosen reference state, often the ground state of the atom, it is important that this potential can also faithfully de-

scribe the valence properties of the atom in other chemical environments, such as in molecules and solids. This is characterized as the transferability of the pseudopotential. It can be shown that the norm-conserving pseudopotentials listed above have optimum transferability in some sense [104, 128, 129]. Norm-conserving pseudopotentials, as well as the majority of pseudopotentials in use, are also dependent on the angular momentum l because the potential valence electrons feel from core electrons is not the same in different states (s, p, d, etc.). Such pseudopotentials are also referred to as nonlocal or semi-local pseudopotentials.

Norm-conserving pseudopotentials are constructed from first-principles all-electron atomic calculation results. The first step of the scheme is to self-consistently solve the KS equation for each l in a reference atomic configuration with imposed spherical symmetry and a chosen exchange-correlation potential:

$$(\hat{T} + V^{\mathrm{AE}} - \varepsilon_l)\psi_l^{\mathrm{AE}} = 0, \tag{2.39}$$

where V^{AE} is the sum of the ionic Coulomb potential, the Hartree potential and the exchange-correlation potential:

$$V^{\mathrm{AE}} = -\frac{Z}{r} + V_{\mathrm{H}}[n^{\mathrm{AE}}(\mathbf{r})] + V_{\mathrm{xc}}[n^{\mathrm{AE}}(\mathbf{r})]. \tag{2.40}$$

From the AE wave function ψ_l^{AE} determined by the first-principles procedure, the pseudo wave function ψ_l^{PS} can be created by applying the norm-conservation constraint. This pseudopotential must be nodeless within the cutoff radius r_{c}, while be identical as the AE wave function outside r_{c}, and yield the same eigenvalue ε_l as well.

The major difference between various pseudopotential methods is the form of the pseudo-wave-functions, and the properties of the norm-conserving pseudopoten-

tials permit a great deal of freedom when creating pseudo-wave functions from the AE results. Various recipes have been proposed in the last couple of decades, such as the Bachelet scheme [129], and the Troullier and Martins scheme [130].

The pseudopotentials used in the present work are constructed using the optimized pseudopotential method devised by Rappe *et al.* in 1990 [131]. This type of pseudopotentials are softer (i.e. have rapid plane wave convergence) than most of the other norm-conserving pseudopotentials, and they perform especially well for elements in the first row (e.g. O, F, N) and the transition metals (e.g. Mn, Fe, Cr, Ni). In this method the pseudo orbitals are expanded in spherical Bessel functions for $r < r_c$:

$$\psi_l^{PS}(\mathbf{r}) = \begin{cases} \psi_l^{AE}(\mathbf{r}) & \text{if } r > r_c \\ r\sum_{i=1}^{4} \alpha_i j_l(q_i r_c) & \text{otherwise} \end{cases}$$

The coefficients are determined so that the normalization condition of the wave function is satisfied, and the wave function is continuous at r_c up to the second derivative. The wave vectors of the Bessel functions, q_i, are chosen by enforcing the constraint:

$$\frac{j_l'(q_i r_c)}{j_l(q_i r_c)} = \frac{\psi_l'(r_c)}{\psi_l(r_c)}. \tag{2.41}$$

All the optimized pseudopotentials used in this work were generated and tested by OPIUM (Open-source Pseudopotential Interface and Unification Model) code [132] to ensure the accuracy, good transferability, convergency, and efficiency of these pseudopotentials.

After constructing the pseudo-wave-functions, the screened pseudopotential is solved by inverting the KS equation:

$$V_{scr}^{PS} = \frac{(\varepsilon_l - \hat{T})\psi_l^{PS}}{\psi_l^{PS}}. \tag{2.42}$$

This is well-defined, since $\psi_l^{\rm PS}$ is nodeless for $r < r_{\rm c}$. After removing the valence contribution to both the Hartree and exchange-correlation potentials, the unscreened pseudopotential is generated:

$$V^{\rm PS} = V_{\rm scr}^{\rm PS} - V_{\rm H}[n^{\rm PS}(\mathbf{r})] - V_{\rm xc}[n^{\rm PS}(\mathbf{r})]. \tag{2.43}$$

The valence charge density $n^{\rm PS}(\mathbf{r})$ here is defined as:

$$n^{\rm PS}(\mathbf{r}) \equiv \sum_l f_l |\psi_l^{\rm PS}|^2, \tag{2.44}$$

where f_l is the degeneracy of the state with angular momentum l. For instance, f_l is 2 for the s state, 6 for the p state, etc.

2.2.4 LAPW basis functions

The all-electron linearized augmented planewave method (LAPW) [133] is used in this work to achieve the required accuracy necessary for calculating the electric field gradients (EFGs). The LAPW method is based on the augmented planewave method (APW), first introduced by Slater in 1937 [134]. The LAPW method is one of the most accurate DFT methods which can be applied in real materials with reasonable efficiency. Details about the LAPW method have been reviewed by Singh [135], and only some of the main points are described here.

The basic idea of the LAPW method is to partition space into two regions: non-overlapping spheres ("muffin-tin" spheres) with radius $R_{\rm MT}^{\alpha}$ centered on the nuclei, and the interstitial region between the spheres. A schematic picture of the space partition is shown in Fig. 2.2. All quantities (basis functions, charge density, and potential) then have a dual representation. The LAPW basis function ϕ_G is a single planewave in the interstitial region, matched onto a spherical harmonic

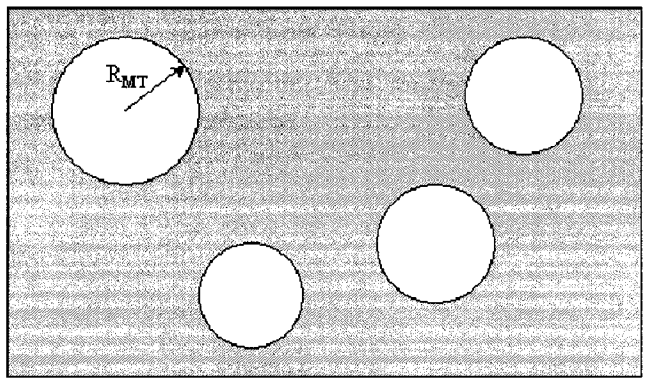

FIG. 2.2: The space partition of the LAPW method in a unit cell: the non-overlapping muffin-tin (MT) spheres with different radius $R_{\rm MT}$ around each atom, and the remaining interstitial region (gray).

representation inside the muffin-tin (MT) spheres:

$$\phi_G(\mathbf{r}) = \begin{cases} \frac{1}{\Omega^{1/2}} \sum_G e^{i(\mathbf{G}+\mathbf{k})\cdot\mathbf{r}} & \mathbf{r} \in \text{interstitial} \\ \sum_{lm} [A_{lm} u_l^\alpha(E_l, r) + B_{lm} \dot{u}_l^\alpha(E_l, r)] Y_{lm}(\hat{r}) & r < R_{\rm MT}^\alpha \end{cases}$$

And the wave function can be written as:

$$\psi_{nk}(\mathbf{r}) = \sum_G C_{n,\mathbf{G}+\mathbf{k}} \phi_G(\mathbf{r}). \tag{2.45}$$

Here Ω is the volume of the unit cell, the Y_{lm}'s are spherical harmonics, and typically values of $l_{max} \sim 8$ are used. The radial function $u_l^\alpha(E_l, r)$ is the regular solution of the radial Schrödinger equation at a fixed energy level E_l for atom α:

$$\left[\frac{1}{2}(-\frac{d^2}{dr^2} + \frac{l(l+1)}{r^2}) + V_{\rm eff}(r) - E_l\right] r u_l^\alpha = 0. \tag{2.46}$$

In this equation, $V_{\rm eff}(r)$ is the spherical component of the effective potential in Eq. (2.19) inside the MT spheres. $\dot{u}_l^\alpha(E_l, r)$ is the energy derivative of the radial

function $u_l^\alpha(E_l, r)$. It satisfies the inhomogeneous radial equation:

$$\left[\frac{1}{2}(-\frac{d^2}{dr^2} + \frac{l(l+1)}{r^2}) + V_{\text{eff}}(r) - E_l\right] r\dot{u}_l^\alpha = ru_l^\alpha. \tag{2.47}$$

The coefficients of the basis functions, A_{lm}'s and B_{lm}'s, are determined by requiring the continuity of the wavefunction and its first derivative at the boundary of the spheres.

Although the fixed energy parameter E_l is not equal to the exact eigenvalue ε_{nk} (as in the APW method), the following Taylor series:

$$u_l(r, \varepsilon_{nk}) = u_l(r, E_l) + (E_l - \varepsilon_{nk})\dot{u}_l(r, E_l) + O((E_l - \varepsilon_{nk})^2) \tag{2.48}$$

motivates the use of the two linearly independent functions u and $\dot{u}$. In practice, the results are very insensitive to the choice of E_l within the range $|E_l - \varepsilon_{nk}| \lesssim 7\ eV$. E_l is normally chosen near the centroid of ε_{nk} corresponding to the atomic eigenvalue with the same l.

The accuracy of such basis functions is controlled by the product of the smallest atomic sphere radius in the unit cell, R_{MT}, and the largest reciprocal wave vector, G_{max}. In general, the value of this product is set to be between 6 and 9, yielding about 100 planewaves per atom in the basis set, for materials containing d and f electrons. Comparable PW pseodopotential calculation would require more than an order of magnitude larger basis set.

The dual representation of the LAPW basis set can describe both localized and delocalized orbitals. However, many materials, including the rare earth elements, the early transition metals, the alkali metals, and the actinides, also possess semi-core states, whose energy lies between that of the valence and core states. The Ti $3s$, $3p$ and Nb $4s$, $4p$ states are examples of semi-core states. Given that such

states are not perfectly confined with the sphere region (as are the core states), orthogonality between the radial functions of the semi-core and the valence with the same angular momentum l is difficult to maintain while preserving accuracy. In order to overcome this difficulty, additional fully localized basis functions are added. Such functions are known as the "local orbitals" [136], and are the combination of two radial functions at different energies together with the first energy derivative of one of them:

$$\phi^{\mathrm{LO}}_{\alpha lm}(\mathbf{r}) = \begin{cases} 0 & \mathbf{r} \in \text{interstitial} \\ \sum_{lm}[A'_{lm}u^{\alpha}_{l}(E^{(1)}_{l},\ \mathbf{r}) + B'_{lm}\dot{u}^{\alpha}_{l}(E^{(1)}_{l},\mathbf{r}) + u^{\alpha}_{l}(E^{(2)}_{l},\mathbf{r})]Y_{lm}(\hat{r}) & r < R^{\alpha}_{MT} \end{cases}$$

The wave function then takes the form:

$$\psi_{nk}(\mathbf{r}) = \sum_{G} C_{n,\mathbf{G}+\mathbf{k}}\phi_{G}(\mathbf{r}) + \sum_{\alpha lm} C'_{\alpha lm}\phi^{\mathrm{LO}}_{\alpha lm}(\mathbf{r}). \tag{2.49}$$

The A'_{lm}'s and B'_{lm}'s coefficients are determined by enforcing the vanishing of ϕ^{LO} and its first derivative at the MT sphere surface. The energy parameter $E^{(2)}_{l}$ is usually near the centroid of the semi-core state. To add these additional functions to the LAPW basis can greatly improve the accuracy without largely increase the size of the basis, take s and p semi-core states for example, only 4 local orbitals are needed for each atom.

2.3 Computation of electric field gradients

The electric field gradient (EFG) is defined as the second derivatives of the Coulomb potential, which includes the external nuclear potential and the Hartree

term (electron-electron interacting potential):

$$V_C(\mathbf{r}) = V_{\text{ext}} + \int \frac{n(\mathbf{r}')}{|\mathbf{r} - \mathbf{r}'|} d\mathbf{r}'. \tag{2.50}$$

This potential can be obtained by solving the Poisson's equation:

$$\nabla^2 V_C(\mathbf{r}) = 4\pi\rho(\mathbf{r}). \tag{2.51}$$

In the LAPW method, the charge density ρ, the sum of the nuclear and electronic densities, has a dual representation:

$$\rho(\mathbf{r}) = \rho_{PW}(\mathbf{r})\theta(\mathbf{r} \in \text{Interstitial}) + \sum_{\alpha}^{\text{MTspheres}} \rho_{\text{MT},\alpha}(\mathbf{r})\theta(\mathbf{r} < \text{R}^{\alpha}_{\text{MT}}), \tag{2.52}$$

where θ is the unit step function enforcing the partition, ρ_{PW} and $\rho_{MT,\alpha}$ are the density in the interstitial and in the MT sphere centered at atom α, respectively. The solution of Poisson's equation is not trivial as it is in the plane wave method, where the Fourier coefficient of the Coulomb potential is simply given as $V_C(\mathbf{G}) = \frac{4\pi\rho(\mathbf{G})}{\mathbf{G}^2}$.

Weinert proposed a method known as the pseudocharge method to solve equation (2.51) for V_C [137] in two steps. The first step is to replace the real charge density $\rho(\mathbf{r})$ by a pseudocharge density $\tilde{\rho}(\mathbf{r})$:

$$\tilde{\rho}(\mathbf{r}) = \rho_I(\mathbf{r})\theta(\mathbf{r} \in \text{Interstitial}) + \sum_{\alpha}^{\text{MTspheres}} \tilde{\rho}_{\alpha}(\mathbf{r})\theta(\mathbf{r} < \text{R}^{\alpha}_{\text{MT}}), \tag{2.53}$$

where θ is the unit step function, and $\tilde{\rho}_{\alpha}(\mathbf{r})$'s have the same multipole moments q_{lm} as the real density $\rho(\mathbf{r})$:

$$q_{lm} \equiv \frac{4\pi}{2l+1} \int_{MT} r^l \rho(\mathbf{r}) Y^*_{lm}(\hat{\mathbf{r}}) d^3\mathbf{r}. \tag{2.54}$$

A smoothly varying form is chosen for $\tilde{\rho}_\alpha$, so it can be expressed in a rapidly convergent Fourier series:

$$\tilde{\rho}(\mathbf{r}) = \sum_{\mathbf{G}} \tilde{\rho}(\mathbf{G}) e^{i\mathbf{G}\cdot\mathbf{r}}, \tag{2.55}$$

and the exact interstitial Coulomb potential can thus be obtained from this pseudocharge density:

$$V_I(\mathbf{r}) = \sum_{\mathbf{G}\neq 0} \frac{4\pi\tilde{\rho}(\mathbf{G})}{\mathbf{G}^2} e^{i\mathbf{G}\cdot\mathbf{r}}. \tag{2.56}$$

This follows from $\tilde{\rho}_\alpha$ having the same multipoles as $\rho_{MT,\alpha}$. However, the pseudocharge density can not directly provide the correct Coulomb potential inside of the spheres. The second step of the Weinert method is to calculate the potential inside the spheres from the V_I in equation (2.56) since it yields the correct boundary condition on the surface of the MT spheres. As a general solution to Poisson's equation with specified values of the potential on the boundary of the sphere, the Coulomb potential inside of the spheres can be written as [138]:

$$V_\alpha(\mathbf{r}) = \int_{MT} \rho_\alpha(\mathbf{r}')G(\mathbf{r},\mathbf{r}')d^3r' - \frac{1}{4\pi}\oint_S V_I(\mathbf{r}')\frac{\partial G(\mathbf{r},\mathbf{r}')}{\partial n'}dS, \tag{2.57}$$

where the Green's function for the sphere is given by

$$G(\mathbf{r},\mathbf{r}') = 4\pi\sum_{lm}\frac{Y^*_{lm}(\hat{\mathbf{r}}')Y_{lm}(\hat{\mathbf{r}})}{2l+1} r_<^l \left(\frac{1}{r_>^{l+1}} - \frac{r_>^l}{R^{2l+1}}\right), \tag{2.58}$$

where $r_>(r_<)$ is the larger(smaller) of r and r', and R is the radius of the MT sphere. The normal derivative of the Green's function for $r' = R$ is given by

$$\frac{\partial G}{\partial n'} = \left.\frac{\partial G}{\partial r'}\right|_{r'=R} = \frac{-4\pi}{R^2}\sum_{lm} Y^*_{lm}(\hat{\mathbf{r}}')Y_{lm}(\hat{\mathbf{r}})\left(\frac{r}{R}\right)^l. \tag{2.59}$$

Consequently, the total Coulomb potential can be expressed as

$$V(\mathbf{r}) = \int_{MT} \rho(\mathbf{r}')G(\mathbf{r},\mathbf{r}')d^3r' + \sum_{lm} V_{lm}\left(\frac{r}{R}\right)^l Y_{lm}(\hat{\mathbf{r}}), \tag{2.60}$$

where V_{lm} is defined by $V(\mathbf{R}) \equiv \sum_{lm} V_{lm}Y_{lm}(\hat{\mathbf{R}})$. The EFG can then be obtained by directly taking the derivatives of the Coulomb potential.

For each atom, the EFG can be separated into two contributions: 1) that due to the charge density within the MT sphere of the given nucleus, and 2) that due to the charge density distribution external to the MT sphere. The external contribution is included in the second term of of Eq. (2.60), but this term also includes a contribution from the multipole moments q_{lm} of the charge density within the MT sphere. Thus the external EFG contribution is determined by the potential given by

$$V^{\text{ext}}(\mathbf{R}) \equiv \sum_{lm} \left\{V_{lm} - \frac{q_{lm}}{R^{l+1}}\right\}\left(\frac{r}{R}\right)^l Y_{lm}(\hat{\mathbf{r}}). \tag{2.61}$$

if expanding the Coulomb potential around a nucleus in spherical harmonics, the only terms that contribute to the EFG are the $l = 2$ components, and Eq. (2.61) can be simplified to

$$V^{\text{ext}}(\mathbf{R}) \equiv \sum_{m} \left\{V_{2,m} - \frac{q_{2,m}}{R^3}\right\}\left(\frac{r}{R}\right)^2 Y_{2,m}(\hat{\mathbf{r}}). \tag{2.62}$$

Similarly, the EFG can be further analyzed by synthesizing the charge density using only band eigenstates within certain energies, e.g. originating from electronic orbitals associated with specific atoms. By expanding the Coulomb potential in

spherical harmonics near the nuclear site:

$$V_C(\mathbf{r} \to 0) = \sum_{lm} \left[\frac{4\pi}{2l+1}\right]^{1/2} r^l \Phi_{l,m} Y_{lm}(\hat{r}), \tag{2.63}$$

only the $l = 2$ terms contribute to the EFG tensor. From the asymptotic form of V_C, elements of the EFG tensor can be expressed in a simple way [139]:

$$\begin{aligned}
V_{xx} &= \left(\frac{3}{2}\right)^{1/2} (\Phi_{2,-2} + \Phi_{2,2}) - \Phi_{2,0}, \\
V_{yy} &= -\left(\frac{3}{2}\right)^{1/2} (\Phi_{2,-2} + \Phi_{2,2}) - \Phi_{2,0}, \\
V_{zz} &= 2\Phi_{2,0}, \\
V_{xy} &= V_{yx} = -i\left(\frac{3}{2}\right)^{1/2} (\Phi_{2,-2} - \Phi_{2,2}), \\
V_{yz} &= V_{zy} = -i\left(\frac{3}{2}\right)^{1/2} (\Phi_{2,-1} + \Phi_{2,1}), \\
V_{zx} &= V_{xz} = \left(\frac{3}{2}\right)^{1/2} (\Phi_{2,-1} - \Phi_{2,1}).
\end{aligned}$$

Here, $\Phi_{2,m} = \Phi^*_{2,m} = \lim_{r\to 0} \left[\frac{5}{4\pi}\right]^{1/2} \frac{V_{2m}(r)}{r^2}$. And under the traceless constraint of the EFG tensor:

$$V_{zz} = -(V_{xx} + V_{yy}) = 2\Phi_{2,0}. \tag{2.64}$$

By applying both the LAPW method and the pseudopotential method within the frame work of the density functional theory, one is able to explore the local structure of complex ferroelectric solid solutions by studying the EFGs of the fully optimized crystal structures. This procedure will be implemented for $Pb(Zr_{1/2}Ti_{1/2})O_3$, $Pb(Sc_{1/2}Ta_{1/2})O_3$, $Pb(Sc_{2/3}W_{1/3})O_3$, and $Pb(Mg_{1/3}Nb_{2/3})O_3$ as will be shown later in this work.

Chapter 3

Structural dependence of EFGs in PZT

Recently, Baldwin *et al.* [39] presented the first NMR solid-state study of $Pb(Zr_{1-x}Ti_x)O_3$ (PZT) solid-solution series as a function of x using ^{17}O, $^{47,49}Ti$, and ^{207}Pb spectra. They interpreted their results as providing evidence for an anisotropy in the local structure of PZT solutions. In this chapter, calculated electric filed gradients (EFGs) in PZT structures are presented as a function of chemical ordering and applied strain to assess this interpretation.

This chapter is organized as follows. Section 3.1 gives technical details of the LAPW evaluation of EFGs. Section 3.2 describes the PZT structural models and compares the relaxed structures with experimental pair distribution measurements. In Section 3.3, EFG results and calculated NMR EFG powder spectra are presented as a function of chemical ordering and strain. A discussion of the results and comparison with recent PZT NMR measurements are given in Section 3.4. Details of the NMR static powder spectra calculations are given in Appendix A.

3.1 Simulation procedure

All calculations were performed with the local density approximation (LDA), using the first-principles all-electron LAPW plus local orbital (LAPW+LO) method [135]. The local orbital extension yields the most accurate treatment of atoms with extended semi-core orbitals, allowing them to be treated variationally along with the valence bands in a single energy window. The use of local orbitals can also provide additional variational freedom for valence states. Local orbitals were associated with the Zr $4s$, $4p$, Ti $3s$, $3p$, and O $2s$, $2p$ states. Core-electron states were calculated with a fully relativistic atomic-like approximation using the self-consistent crystal potential. The valence states were treated scalar-relativistically, and the Hedin-Lundqvist exchange-correlation functional [106] was used. The LAPW basis functions, charge density and potential are all described by a dual representation. Within non-overlapping ("muffin-tin") spheres that are centered on the nuclear positions these functions are represented by numerical radial functions times spherical harmonics. In the interstitial region between the spheres, all functions are represented by plane wave expansions. Muffin tin (MT) sphere radii of 2.30, 1.65, 1.65, and 1.55 a.u. were used for the Pb, Zr, Ti, and O ions, respectively. For all systems, a well-converged 44 Ry plane wave energy cutoff was used, and special $\mathbf{k}$ points [125] were used to sample the Brillouin zone with a $4 \times 4 \times 4$ mesh.

In a crystal, the EFG at an atomic nucleus is induced by the nonspherical field of the electrons and other ions. Typically, the dominant electronic contributions come from the valence electron and shallow semi-core states. Ehmann and Fahnle [140] have calculated EFG corrections due to the polarization of tightly bound core electron states using a method similar to Sternheimer's [141]. In their calculations, the perturbation acting on the core states is due to the nonspherical effective crystal potential near the nucleus, as determined from first-principles all-electron LAPW

calculations using a spherical core. For a nearest neighbor site of a substitutional Ni atom in Cu, they found that the principal core contributions to the Cu EFG came from the Cu($3p$) states, about 25% of the calculated EFG using spherical core states, while the contributions of the $2p$ states was small and the s-states contributions could be neglected. In the present calculations, the corresponding Ti($3s$,$3p$) and Zr($4s$,$4p$) shells are treated variationally, and so the effects of core polarization are adequately treated. The definition of the EFG tensor is given in Appendix A.

For each structure, all the atomic positions were allowed to relax, consistent with the imposed symmetry, until the calculated forces were less than 0.02 eV/Å. The resulting EFGs are estimated as accurate to less than ~5% error with respect to the atomic positions.

3.2 Structural models and comparison with experimental pair distribution functions

PZT 50/50 was studied using $Pb(Zr_{1/2}Ti_{1/2})O_3$ 10 atom supercells. Most of the calculations were performed for [001]1:1 B-site ordered unit cells, with the ferroelectric polarization direction along the [001] axis in imposed $P4mm$ symmetry. This corresponds to alternating Zr and Ti atoms along the [001] direction. In this structure, the B-atom planes perpendicular to the [001] direction contain either all Zr or all Ti. Calculations with these supercells were performed for various c/a values with imposed tetragonal $P4mm$, monoclinic Cm, and $P1$ triclinic symmetry. Experimentally, Noheda *et al.* [57] find that monoclinic PZT, near 50/50 composition, has only a small monoclinic angular distortion, $\beta = 90.5°$. In the calculations presented here, this angle is simply set to 90° in all of the calculations. Some calculations were also performed for supercells with [001]1:1 B-site ordering with imposed orthorhombic

$P2mm$ symmetry. The $P2mm$ orthorhombic unit cell has dimensions $a' \times a \times 2a$, corresponding to alternating Ti and Zr B-atom stacking along the [001] direction with periodicity $2a$, with the ferroelectric polarization along the a' [100] direction. Thus, the $P2mm$ "c/a" value given in Table 3.2 is actually $a'/a = 1.04$. Finally, a [111]1:1 B-site ordered supercell with imposed $R3m$ symmetry is also studied. In all calculations, the unit cell was set to the experimental volume [142].

The relaxed structural models can be compared to experimentally determined pair distribution functions. Experimental 10 K PDFs from Dmowski *et al.* [63] (their Fig. 4) are shown in Fig. 3.1. The experimental PDFs were obtained from Fourier transform of neutron scattering structure factors. The average observed symmetry is tetragonal $P4mm$ for 60% Ti, monoclinic Cm for 48% Ti, and rhombohedral $R3c$ for 40% Ti. Fig. 3.2 compares the calculated PDFs for the relaxed PZT 50/50 structures with experiment. The top panel of Fig. 3.2 compares the experimental 60% Ti PDFs with calculated PDFs for tetragonal $P4mm$ and also with reduced orthorhombic $P2mm$ imposed symmetry, the middle panel compares the experimental 48% Ti PDF with the calculated PDF for monoclinic Cm imposed symmetry, and the bottom panel compares the experimental 40% Ti with the calculated PDF for rhombohedral $R3m$ imposed symmetry. The calculations used $c/a = 1.045$ (1.02) for $P4mm$ (Cm), respectively, as determined by the experimental Rietveld analysis [63] for the corresponding samples. $P2mm$ calculations were for $c/a = 1.04$. The simulated PDFs were obtained using the calculated relaxed atomic positions as input into the PDFFIT program [143], which weights pairs of atoms by the product of their neutron scattering lengths. The simulations used $Q_{max} = 80$ Å^{-1}, and an isotropic thermal factor of 0.005 Å^2 for all the atoms. Compared to the PZT 40/60 experimental PDF, the rms errors between 1.7 and 10 Å are 0.018 and 0.011 Å^{-3} for $P4mm$ and $P2mm$ imposed symmetries, respectively. The rms error for Cm symmetry is 0.017 Å^{-3} and 0.022 Å^{-3} for $R3m$ symmetry.

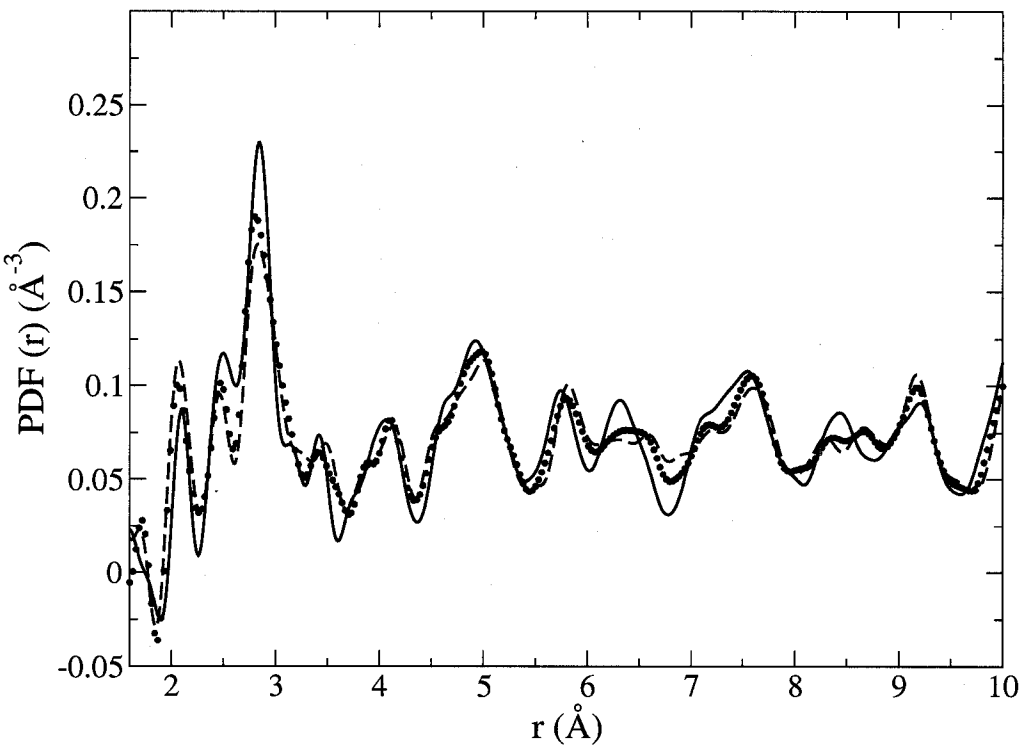

FIG. 3.1: PZT experimental pair distribution functions (PDF) at $T = 10$ K from Fig. 4 of Dmowski *et al.* [63]: 60% Ti with average $P4mm$ symmetry (solid line), 48% Ti with average Cm symmetry [(red) dotted line], and 40% Ti with average $R3c$ symmetry [dashed (blue) line].

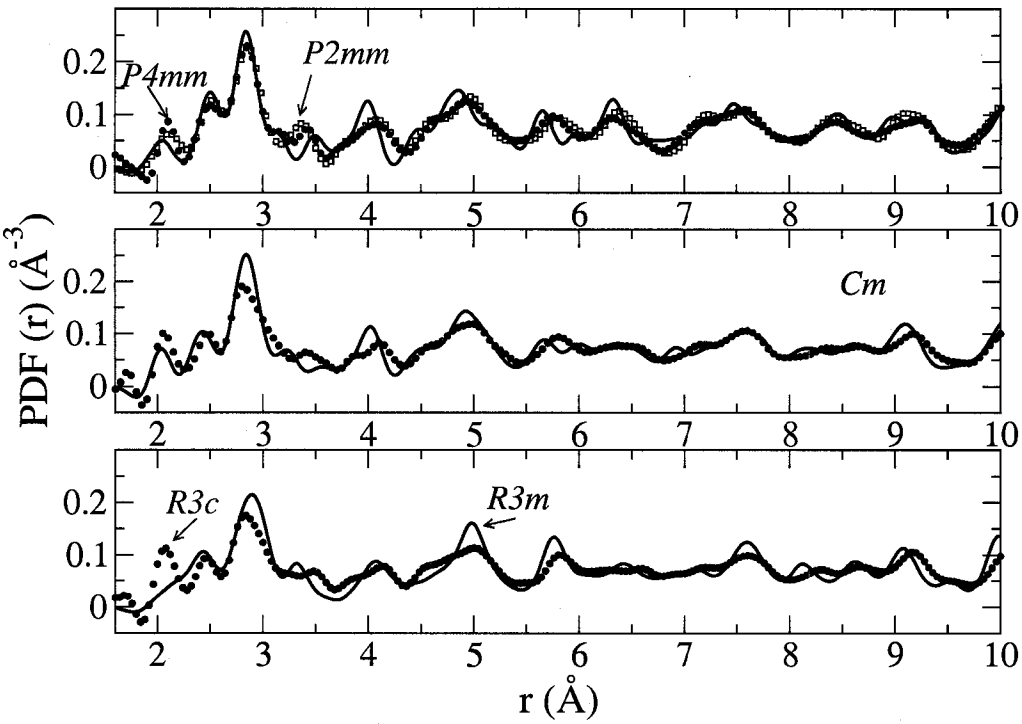

FIG. 3.2: PZT experimental pair distribution functions (PDF) at $T = 10$ K [dotted (red) curves] from Dmowski *et al.* [63] are compared to simulated PDFs, calculated using the relaxed atomic positions (see text). Top panel: experimental PDF for 60% Ti with average $P4mm$ symmetry, and calculated PZT 50/50 PDFs with symmetries $P4mm$ (solid line) and $P2mm$ [(blue) box symbols]. Middle panel: experimental PDF for 48% Ti with average Cm symmetry, and calculated PZT 50/50 PDF with Cm symmetry (solid line). Bottom panel: experimental PDF for 40% Ti with average $R3c$ symmetry, and calculated PZT 50/50 PDF with $R3m$ symmetry (solid line).

A generic feature of many lead-based perovskite alloys is the wide range of Pb-O nearest-neighbor bond lengths. Table 3.1 shows the Pb-O nearest-neighbor bond lengths in both tetragonal and monoclinic imposed symmetries for the relaxed structures. In tetragonal symmetry, there are four groupings of Pb-O bond lengths: $\sim$ 2.5, 2.9, 3.2, and 3.5 Å. In imposed monoclinic Cm symmetry, the Pb-O groupings are more spread out. The experimental and theoretical curves in the top panel of Fig. 3.2 both show peaks at $\sim$ 2.5, 2.9, 3.5 Å and a shoulder at $\sim$ 3.2 Å, corresponding to these Pb-O distances. These features, especially the peak near $\sim$ 2.5 Å, are also evident at the other compositions. The presence of the 2.5 Å bond length, similar to the shortest Pb-O distance in $PbTiO_3$, is characteristic of PZT and many other perovskite lead-based alloys, as noted by Dmowski *et al.* Based on comparisons with model PDFs, Dmowski *et al.* concluded that the greatest changes with varying Ti/Zr composition in PZT was the distribution in direction of the Pb displacements, with Ti-rich local environments tended to have $\langle 100 \rangle$ pseudocubic Pb displacements while Zr-rich environments tended to have $\langle 110 \rangle$ pseudocubic Pb displacements. This is consistent with our monoclinic Cm calculations, which show that the Pb atoms move toward one side of the oxygen octahedra and displace between the $\langle 111 \rangle$ and $\langle 001 \rangle$ directions.

Very small energy differences separate the simulated [001]1:1 B-site ordered PZT 50/50 $P2mm$, Cm, and $P4mm$ relaxed structures shown in Fig. 3.2. The $P2mm$ and Cm structures differ by only $\sim$ 0.02 mRy per perovskite formula unit, while the $P4mm$ structure is only $\sim$ 1.2 mRy higher in energy. The [111]1:1 B-site ordered $R3m$ structure is the lowest energy structure considered here, being $\sim$ 23 mRy lower than the [001]1:1 structures. Since ordered PZT does not exist at these compositions, it is likely that the Born Oppenheimer energy landscape is described by many local minima with small energy separations and with local atomic structure similar to the present [001]1:1 and [111]1:1 models. The system is thus kinetically

TABLE 3.1: Calculated PZT 50/50 Pb-O nearest-neighbor distances (Å) for Cm monoclinic and $P4mm$ tetragonal imposed symmetries. c/a values correspond to Fig. 3.2, and m refers to the number of bonds of the given length.

Cm c/a=1.02				$P4mm$ c/a=1.045			
Pb_1-O	m	Pb_2-O	m	Pb_1-O	m	Pb_2-O	m
2.437	2	2.384	2	2.533	4	2.484	4
2.515	1	2.496	1	2.871	4	2.877	4
2.816	2	2.757	2	3.170	4	3.535	4
2.901	2	2.906	2	–	–	–	–
2.920	2	3.255	2	–	–	–	–
3.242	1	3.266	1	–	–	–	–
3.248	2	3.533	2	–	–	–	–

trapped in a disordered state. However, the good agreement of the calculated PDFs with experiment indicates that the nearest neighbor atomic structure is reasonably well reproduced in the relaxed PZT structural models.

3.3 EFG results and simulated NMR spectra

Calculated values of V_{zz} for [001]1:1 ordered PZT, with imposed monoclinic Cm and tetragonal $P4mm$ symmetries are displayed in Figure 3.3, as a function of c/a. For Cm symmetry, the corresponding EFG asymmetry parameter η is shown in Fig. 3.4 (see Appendix A for definitions of V_{zz} and η). The labeling of the atoms is as follows. The Pb_1 and Pb_2 atoms have the shortest A-B bond length with the Zr (Ti) atoms, respectively. For example, at $c/a = 1.035$ and with Cm symmetry, the Pb_1-B distances are 6.34 a.u. (6.64 a.u.) for Zr (Ti), respectively, and Pb_2-B distances are 6.82 a.u. (6.17 a.u.) for Zr (Ti), respectively. The ideal A-B bond-length at this c/a is 6.66 a.u. Apex (c-axis) oxygen atoms O_1 and O_3 have their shortest B-O bond length with the Zr (Ti) atoms, respectively. The O_2 and O_4 atoms are roughly coplanar with the [001]-layers of Zr (Ti), respectively.

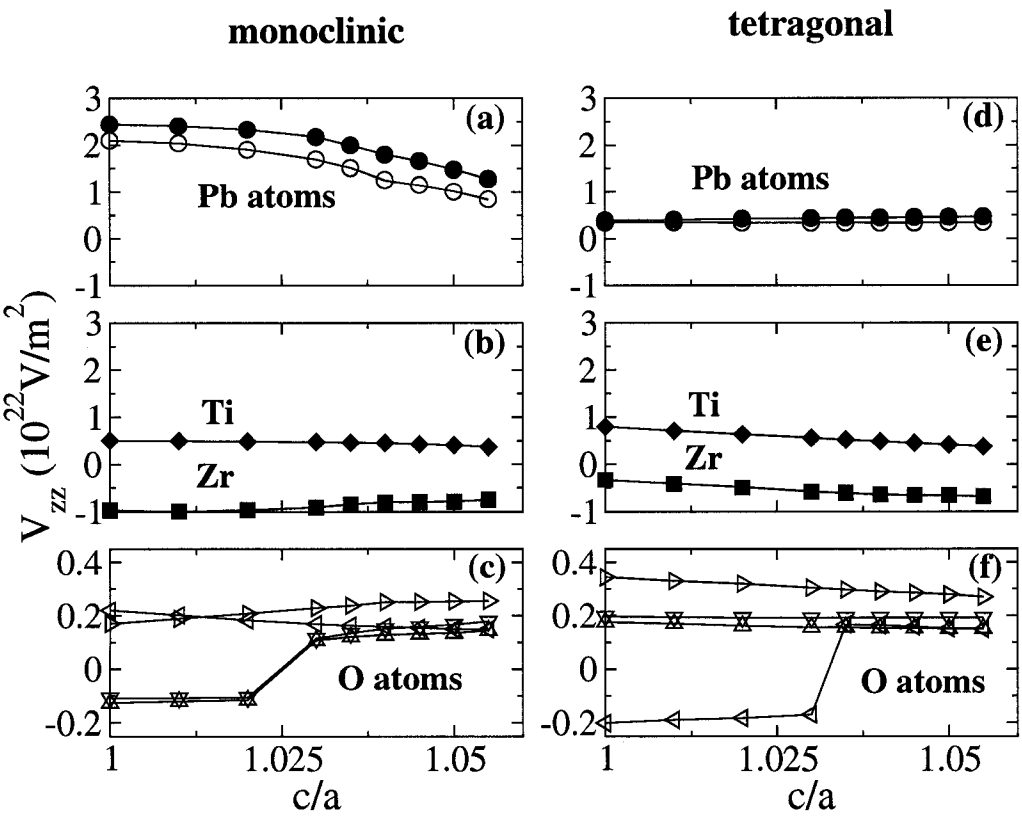

FIG. 3.3: Calculated V_{zz} vs c/a for PZT (50/50). Panels (a)-(c) are for imposed monoclinic Cm symmetry, and panels (d)-(f) are for tetragonal $P4mm$ symmetry. In (a) and (d), open (filled) circles represent Pb_1 (Pb_2), respectively (see text). In (b) and (e), squares (diamonds) represent Zr (Ti), respectively. In (c) and (f), triangles pointing up, down, left, and right represent oxygen atoms O_1, O_3, O_2, and O_4, respectively (see text). Note the change of scale for the O atoms.

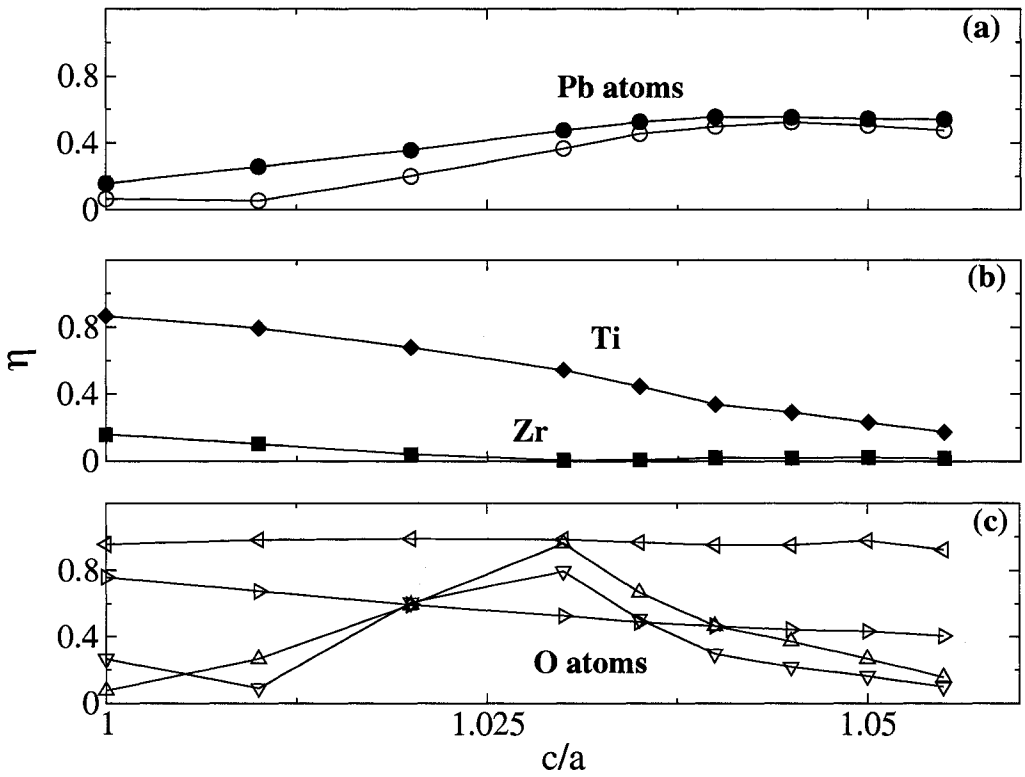

FIG. 3.4: Calculated EFG asymmetry for PZT (50/50) with imposed monoclinic Cm symmetry. Panels (a)-(c) show η vs c/a. Symbols are the same as in Fig. 3.3

The rotation of the polarization away from the [001] direction with decreasing c/a is responsible for the abrupt sign change of V_{zz} for the apex oxygen atoms in Fig. 3.3 for Cm symmetry. Polarization rotation also accounts for the increasing Pb V_{zz}. Neither of these features are seen in $P4mm$ symmetry, where the polarization is constrained to lie along the [001] direction. The polarization rotation coincides with a rotation and shearing of the BO_6 octrahedra, as discussed further below and in Section 3.4.

Numerical results for selected c/a are given in Table 3.2. Also shown in the Table 3.2 are results for [001]1:1 orthorhombic $P2mm$ symmetry and triclinic $P1$ symmetry. For comparison, EFGs for ground state tetragonal $PbTiO_3$ are shown in Table 3.3, which also shows differences in the calculated EFGs due to differences between calculated and experimental geometries. The large η's of the coplanar O_2 and O_4 atoms seen in the tables can be understood by considering the simpler case of $P4mm$ symmetry. In both PZT and $PbTiO_3$, the EFG tensor of the coplanar O atoms have their principal axes oriented as follows. One is along the the c direction (the ferroelectric distortion direction), one is approximately along the B-O bond direction, and the third is perpendicular to these two. The electric field gradients along the c and B-O bond directions are larger than that perpendicular to the bond, due to the B atom off-centering, and this results in large values of η.

Several features are worth noting in the calculated EFGs. As shown by Wu and Krakauer [60] for [001]1:1 ordered PZT with imposed Cm symmetry, the electric polarization is nearly parallel to the [001] (c-axis) for $c/a \gtrsim 1.04$, and it begins to rotate away from the c-axis at $c/a \sim 1.035$. As seen in Figs. 3.3 and 3.4, however, even above $c/a = 1.04$, the EFGs are sensitive to the onset of the polarization rotation. As the electric polarization begins to rotate away from the [001] direction into the Cm mirror plane near $c/a \simeq 1.035$, there are large changes in the calculated η's. The η's for Pb and Ti do not vanish even for large c/a values (as they would for

TABLE 3.2: Calculated EFGs (V_{zz} in units of 10^{22} V/m^2) for PZT 50/50 with imposed monoclinic Cm, triclinic $P1$, tetragonal $P4mm$, orthorhombic $P2mm$, and rhombohedral $R3m$ symmetries. Note that in $P1$ and $P2mm$ symmetries, the two O_2 and two O_4 atoms are not equivalent, while in R3m symmetry, atoms labeled O_1 and O_2, are equivalent (and similarly for oxygen atoms labeled O_3 and O_4).

	Cm						$P1$		$P4mm$		$P2mm$		$R3m$	
	$c/a = 1.0$		$c/a = 1.035$		$c/a = 1.055$		$c/a = 1.055$		$c/a = 1.055$		$c/a = 1.04$		$c/a = 1.0$	
	V_{zz}	η	V_{zz}	η	V_{zz}	η	V_{zz}	η	V_{zz}	η	V_{zz}	η	V_{zz}	η
Pb_1	2.102	0.065	1.515	0.455	0.846	0.475	1.043	0.508	0.347	0	0.806	0.338	1.937	0
Pb_2	2.450	0.157	2.001	0.527	1.280	0.542	1.469	0.542	0.470	0	0.806	0.338	2.403	0
Zr	-0.972	0.159	-0.847	0.008	-0.750	0.017	-0.809	0.022	-0.685	0	-0.948	0.220	-0.393	0
Ti	0.507	0.866	0.462	0.445	0.372	0.173	0.373	0.247	0.376	0	0.422	0.545	-0.229	0
O_1	-0.126	0.077	0.121	0.666	0.146	0.157	0.137	0.255	0.152	0	-0.173	0.419	-0.125	0.088
O_2	0.220	0.954	0.163	0.966	0.149	0.922	0.147	0.967	0.149	0.944	-0.173	0.419	-0.125	0.088
O_2	0.220	0.954	0.163	0.966	0.149	0.922	0.147	0.959	0.149	0.944	-0.385	0.450	-0.125	0.088
O_3	-0.108	0.266	0.134	0.506	0.179	0.100	0.168	0.166	0.192	0	0.302	0.611	-0.144	0.434
O_4	0.170	0.758	0.238	0.488	0.256	0.405	0.248	0.419	0.270	0.380	-0.129	0.557	-0.144	0.434
O_4	0.170	0.758	0.238	0.488	0.256	0.405	0.247	0.426	0.270	0.380	-0.146	0.669	-0.144	0.434

TABLE 3.3: Calculated EFGs (V_{zz} in units of 10^{22} V/m^2) for tetragonal $PbTiO_3$. All calculations are at the experimental volume. "Exp." indicates that both the experimental [144] $c/a = 1.0636$ and atomic positions (reduced coordinates u_i) were used. The other EFG results are obtained using the fully relaxed atomic positions at the indicated c/a.

	Exp. $c/a = 1.0636$			$c/a = 1.065$		
	u_i	V_{zz}	η	u_i	V_{zz}	η
Pb	0.0	0.361	0.0	0.0	0.472	0.0
Ti	0.549	-0.172	0.0	0.546	-0.097	0.0
O_1	0.117	0.061	0.0	0.122	0.111	0.0
O_2	0.620	0.109	0.697	0.626	0.125	0.638

imposed $P4mm$ symmetry). As c/a decreases η(Pb) decreases while η(Ti) increases. At the same time, the apex oxygen's $\eta(O_1)$ and $\eta(O_3)$ first sharply increase and then decrease as c/a is further reduced. The $\eta(O_4)$, which is coplanar with the Ti, increases monotonically with η(Ti), while η(Zr) and the coplanar $\eta(O_2)$ both stay nearly constant. The η(Zr) is very small, while $\eta(O_2) \simeq 0.95$ is large and about the same as in $P4mm$ symmetry (not shown in the figure, but see Table 3.2). The structural dependences of the Ti and apex O EFGs are related to the shearing of the TiO_6 octahedra, which is further discussed in Section 3.4.

The calculated Pb EFGs show large sensitivity to the structure. For example, near $c/a \simeq 1.035$ in Fig. 3.3, V_{zz}(Pb) is much larger in Cm than in imposed $P4mm$ symmetry, even though the Cm electric polarization is still nearly parallel to the c-axis. This is also seen in Table 3.2, comparing V_{zz}(Pb) for different imposed symmetries. Upon relaxing the imposed symmetry from monoclinic Cm to triclinic $P1$, the Pb-O distances change by less than 0.04 Å, although V_{zz}(Pb) changes by about 20%. These indicate that the EFGs are a very sensitive probe of local structural changes, this will be discussed further in Section 3.4.1. The large changes in Pb EFGs seen here are consistent with the large changes observed in recent NMR ^{207}Pb spectra [39] as the Zr composition of PZT is varied, and the resulting Pb chemical shieldings change.

The EFGs of Pb, Ti, and Zr in the $P2mm$ and $P1$ structures are similar to those in the monoclinic symmetry with the same c/a value, as indicated in Table 3.2. V_{zz}(Zr) in rhombohedral $R3m$ PZT is much smaller than in all other [001] chemically stacked structures, but this EFG is in very good agreement with the V_{zz}(Zr) value of -0.356 (in units of 10^{22} V/m^2) in the antiferroelectric $PbZrO_3$ calculated by Johannes and Singh [96]. This indicates that the Zr EFG is sensitive only to the B-site ordering and less sensitive to the polarization and the strain. Compared to the EFG values for $PbTiO_3$ shown in Table 3.3, V_{zz}(Ti) is significantly larger in PZT. There is also

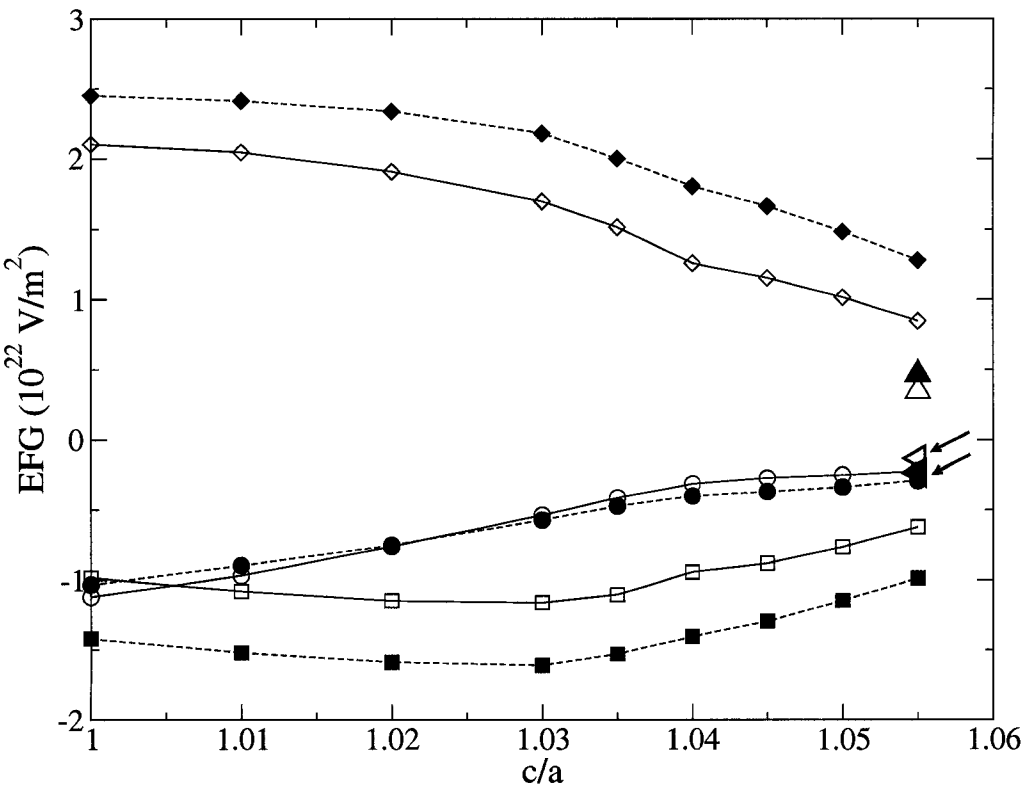

FIG. 3.5: Pb "projected" EFG eigenvalues (see text) vs c/a: circles label $V_\perp$, the EFG eigenvalue for the eigenvector that is perpendicular to the Cm mirror plane; diamonds label V_c, the EFG eigenvalue for the eigenvector that is approximately parallel to the c-axis; squares label $V_\parallel$, the EFG eigenvalue for the remaining eigenvector. The large up-triangles and left-triangles at $c/a = 1.055$, which are identified by arrows for clarity in some cases, represent the conventional EFG eigenvalues calculated in imposed $P4mm$ symmetry: V_{xx}=V_{yy} (left-triangles) and V_{zz} (up-triangles). All open symbols are for Pb_1, and filled symbols are for Pb_2.

a sign change for both V_{zz}(Pb) and V_{zz}(Ti) in PZT compared to $PbTiO_3$, with the exception of rhombohedral PZT.

To help understand the structural dependence of the calculated EFGs, it is helpful to examine the orientation of the EFG principal axes eigenvectors. Note that, by symmetry, one of the eigenvectors of the EFG tensors must be perpendicular to the Cm mirror plane. The corresponding eigenvalue is labeled as $V_\perp$. The other two eigenvectors necessarily lie in the mirror plane. Of these two eigenvectors, the one with the larger dot product with the [001] unit vector (c axis) has its eigenvalue

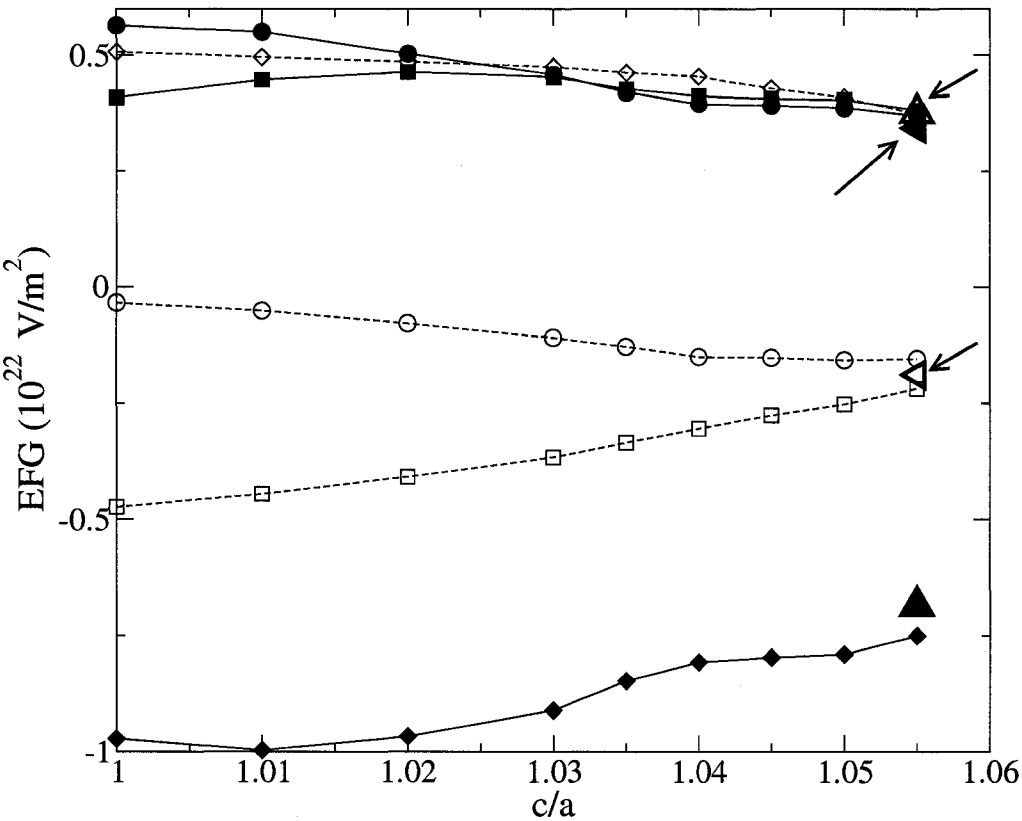

FIG. 3.6: Same as Fig. 3.5, but for Zr and Ti "projected" EFG eigenvalues (see text). All open symbols are for Ti, and filled symbols are for Zr.

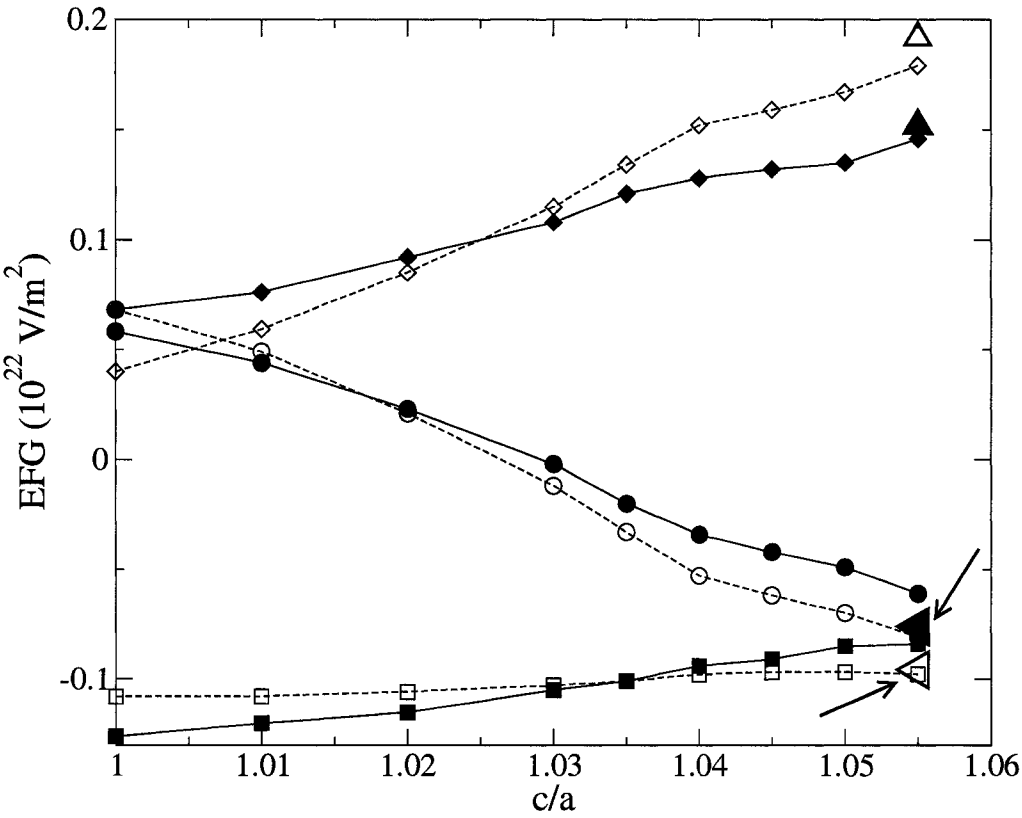

FIG. 3.7: Same as Fig. 3.5, but for the apex-O "projected" EFG eigenvalues (see text). All filled symbols are for O_1 (shortest B-O bond with Zr), and open symbols are for O_3 (shortest B-O bond with Ti).

labeled V_c, and the other is labeled $V_{\|}$. In the following, $V_{\perp}$, $V_{\|}$, and V_c are referred to as "projected" EFG eigenvalues. The projected eigenvalues (rather than the conventionally defined parameters V_{zz} and η) are plotted in Figs. 3.5-3.7 for the cations and apex oxygen atoms. The projected eigenvalues are seen to approach the tetragonal $P4mm$ values $V_{xx} = V_{yy}$ and V_{zz} as c/a increases. For Pb, Zr, and Ti the projected eigenvalue V_c always equals V_{zz}, the conventional (largest magnitude) principal axes EFG eigenvalue. However, for the apex oxygens, $V_{\|} = V_{zz}$ for c/a less than about 1.03, while for larger c/a values, $V_c = V_{zz}$. This abrupt change in direction of the apex oxygens' V_{zz} eigenvector is due to polarization rotation. As c/a decreases from the largest values shown, the projected V_c eigenvalue for the apex O atoms decreases as the BO_6 octahedra begin to rotate and shear from tetragonal symmetry. Similarly, for large c/a, while the system is nearly tetragonal, $V_{\perp} \simeq V_{\|}$, both being nearly equal to $V_{xx} = V_{yy}$ in $P4mm$ symmetry. With decreasing c/a, $V_{\perp}$ becomes less negative, changing sign near $c/a \simeq 1.03$. At this point, the asymmetry parameter reaches it's maximum $\eta = 1$, and the eigenvector associated with $V_{\|}$ becomes the largest eigenvalue $V_{\|} = V_{zz}$ as c/a further decreases. In Section 3.4.2 below (see especially Fig. 3.17), the shearing of the TiO_6 octahedron is shown to be a very sensitive indicator of the onset of polarization rotation.

Direct experimental measurement of the sign of the EFG eigenvalues is difficult to achieve and almost never available. However, it could be indirectly observed from measured NMR spectra. This is illustrated in the simulated NMR EFG powder spectra shown in Figs. 3.8-3.11 for monoclinic Cm. For each atom, the corresponding spectrum of tetragonal $P4mm$ PZT (for $c/a = 1.055$) is also shown for comparison. (NMR spectra for Pb are not shown, since the naturally occurring isotopes have no quadrupolar interaction.) The spectra are powder patterns of the central $(m = 1/2 \leftrightarrow -1/2)$ $\nu_{1/2}^{(2)}$ transition, calculated using perturbation theory to treat the EFG quadrupolar interaction and checked by exact diagonalization of the Hamilto-

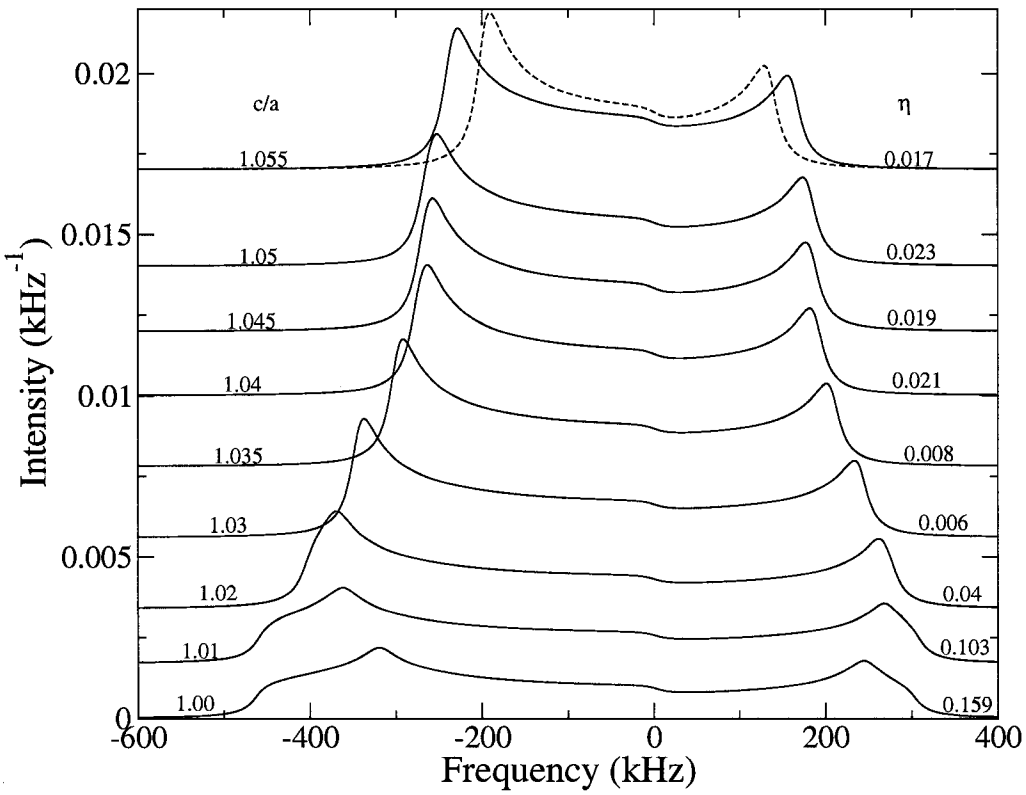

FIG. 3.8: ^{91}Zr calculated static central peak NMR powder spectrum in monoclinic Cm PZT. For comparison, the dotted curve shows the spectrum in tetragonal $P4mm$ PZT with $c/a = 1.055$. Numbers labeling the curves show the corresponding c/a and η values, as indicated.

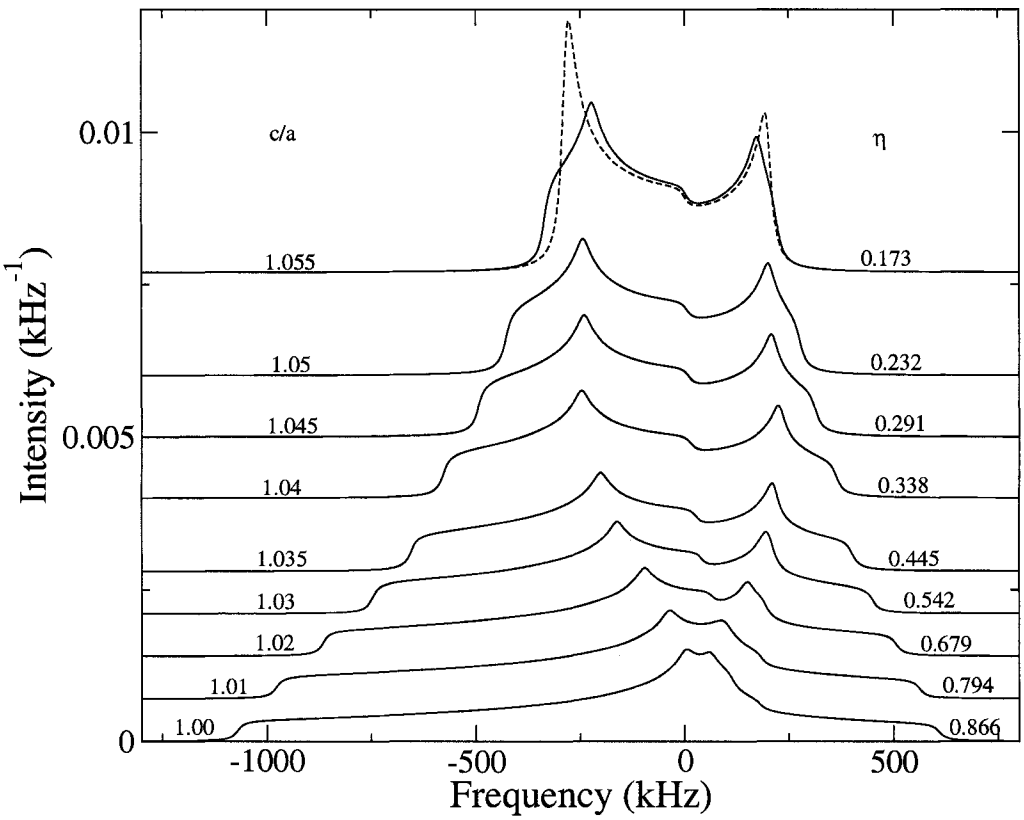

FIG. 3.9: ^{47}Ti static NMR powder spectrum in monoclinic Cm PZT. Dotted curve as in Fig. 3.8.

nian in the $(2m+1)$-dimensional I-subspace [145]. The width of the spectrum is proportional to the square of the V_{zz}, while the splitting of the peaks is controlled by the value of η, with large η corresponding to small peak splitting.

In simulating these spectra, the values used for the quadrupole moments Q were -17.6, 30.2, and -2.558 fm^2 for ^{91}Zr, ^{47}Ti, and ^{17}O, respectively [146]. All these nuclear isotopes have spin $I = 5/2$, and the powder patterns were calculated for an applied (high) field of B = 17.6 T, which corresponds to Larmor frequencies of 70.0, 42.3, and 101.7 MHz for ^{91}Zr, ^{47}Ti, and ^{17}O, respectively. NMR experimental spectra are normally observed for the above isotopes, except for Ti, where both ^{47}Ti ($I = 5/2$) and ^{49}Ti ($I = 7/2$) have nearly overlapping spectra. These two isotopes have very similar magnetic moments, so the difference between their resonance frequencies is small: for example it is only 9 kHz in a 14.1 T applied field. The Ti central transition thus shows overlapping spectra in the experiments [147], and the relative EFG broadenings of ^{47}Ti and ^{49}Ti are $\Delta\nu^{47}/\Delta\nu^{49}\sim 3.44$. In our simulations, the spectra of the two Ti isotopes are, of course, completely separable, and only the spectra for ^{47}Ti are shown in Fig. 3.9.

The calculated NMR spectra of Ti, apex O_1 and O_3, and Ti coplanar O_4 atoms show the largest sensitivity to c/a. The spectra of the ferroelectrically inactive Zr and its equatorial O_2 atom show the least sensitivity. All spectra are seen to approach the $P4mm$ spectra at the largest c/a values. The Ti spectra show a large decrease in width and an increase in peak splitting as c/a increases from 1.0 to 1.055. The spectra of the O_4 atom, which is coplanar with Ti, have splittings that follow a similar trend as for Ti, but the width displays an opposite trend to Ti, increasing as c/a increases. The apex oxygen spectra are also seen to be much narrower than the coplanar oxygens.

The apex-O simulation spectra seen in Figs. 3.12 and 3.13 reflect the abrupt switch in direction of the V_{zz} eigenvector, which occurs when $V_\perp = 0$ near $c/a = 1.03$

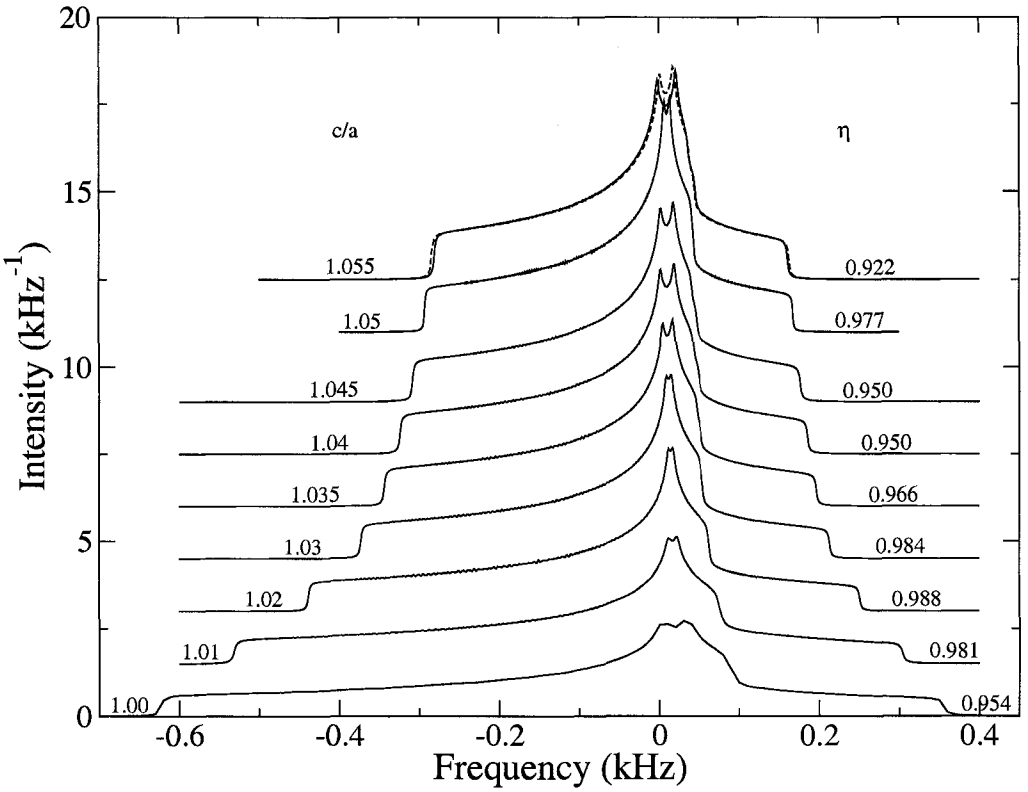

FIG. 3.10: ^{17}O static NMR powder spectrum for the O_2 atom (equatorial O approximately in the Zr plane). Dotted curve as in Fig. 3.8.

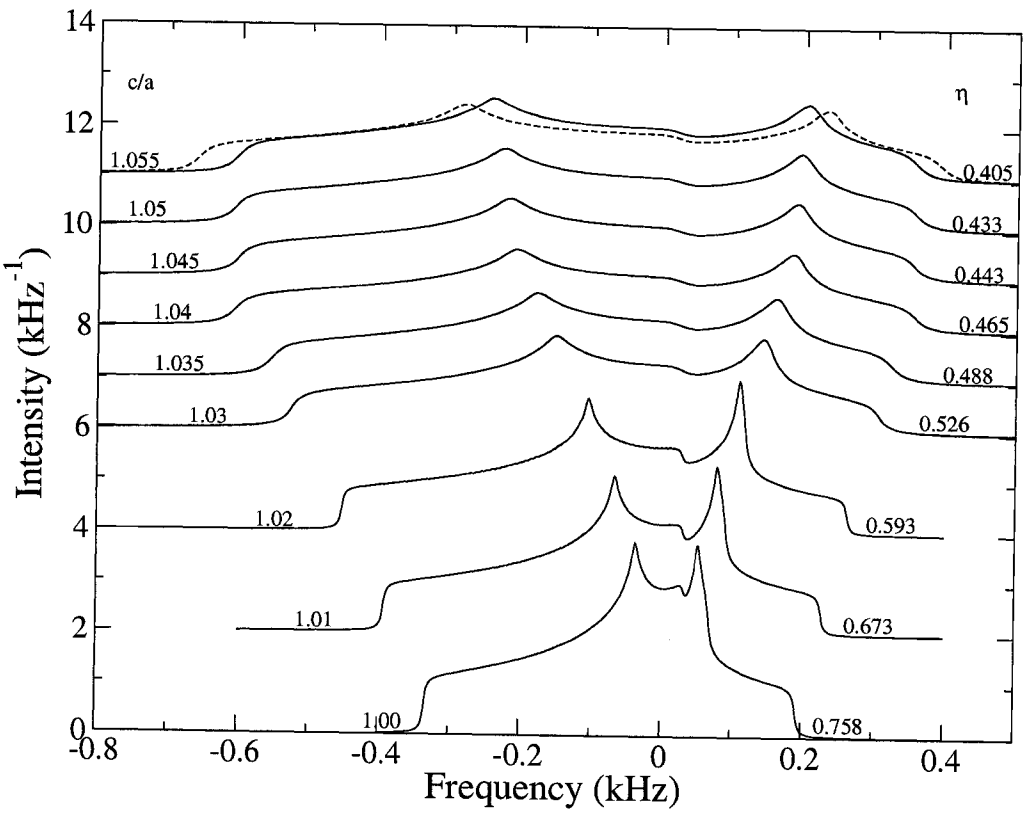

FIG. 3.11: ^{17}O static NMR powder spectrum for the O_4 atom (equatorial O approximately in the Ti plane). Dotted curve as in Fig. 3.8.

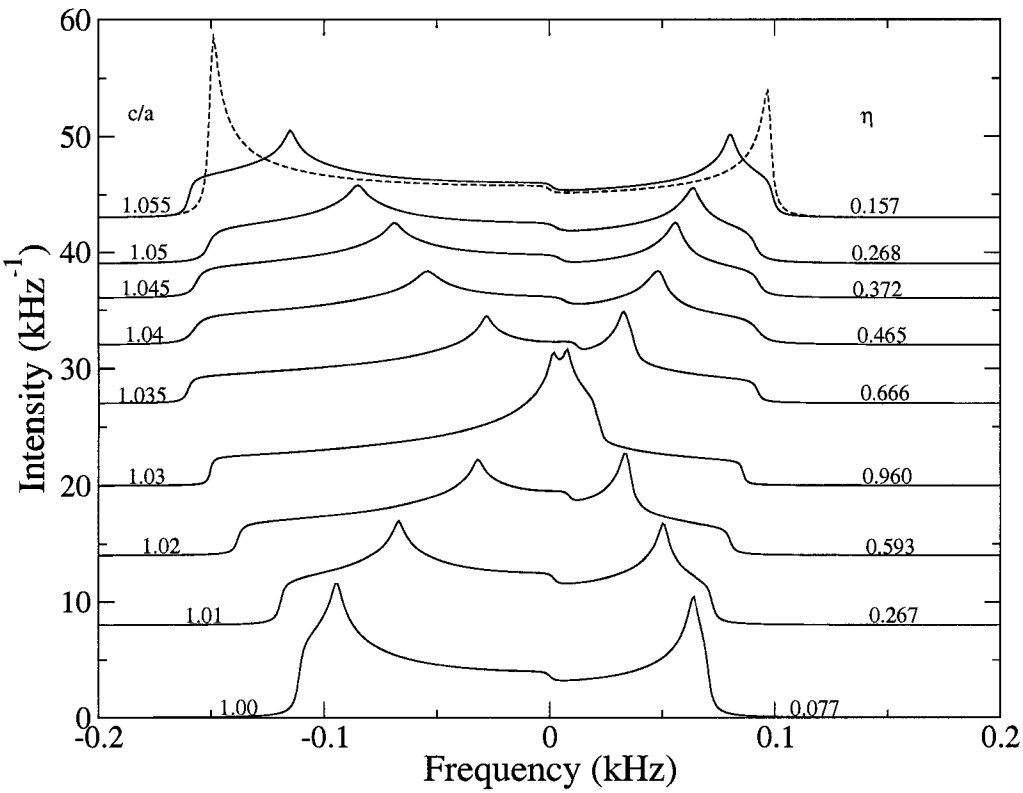

FIG. 3.12: ^{17}O static NMR powder spectrum for the apex O_1 atom (apex O nearest to Zr). Note the change in the frequency scale. Dotted curve as in Fig. 3.8.

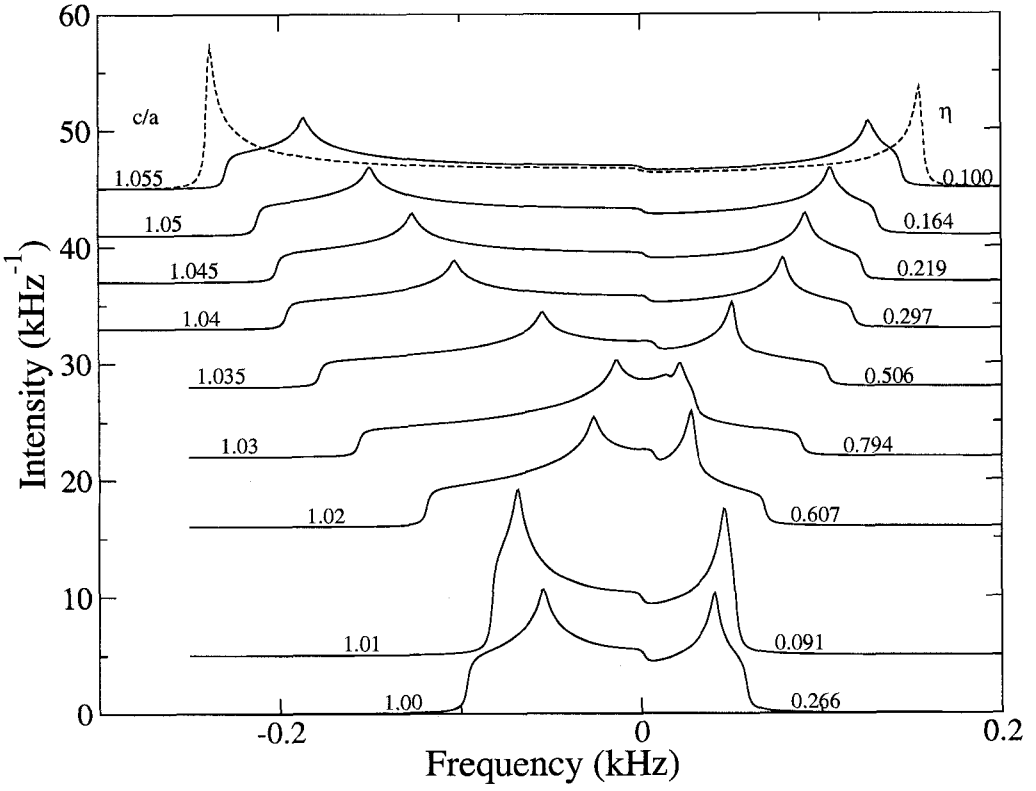

FIG. 3.13: ^{17}O static NMR powder spectrum for the apex O_3 atom (apex O nearest to Ti). Dotted curve as in Fig. 3.8.

in Fig. 3.7. As mentioned, the asymmetry parameter reaches its maximum $\eta = 1$ at this point, and this is evident in the near degeneracy of the two peaks at $c/a = 1.03$ in Figs. 3.12 and 3.13. At this value of c/a the polarization is beginning to rotate away from the [001] direction as c/a decreases. The apex O EFG spectra are thus seen to be a very sensitive probe of structural changes associated with the onset of polarization rotation in PZT.

3.4 Discussion

Since the lead ions give a large contribution to the electric polarization, and since the lead EFGs show considerable sensitivity to B-site ordering, strain, and imposed symmetry, the first subsection below presents a detailed analysis and discussion of the calculated lead EFGs and compares these to a very limited number of non-NMR experimental measurements.

The second subsection discusses the structural dependence of the calculated EFGs of the Ti and O atoms, and their sensitivity to the onset of polarization rotation. The recent suggestion by Baldwin *et al.* [39] of an anisotropy in the local structure of PZT solutions is also considered, based on their Ti and O NMR measurements.

3.4.1 Lead off-centering and lone-pair contributions to the EFG

First, the limited experimental data available for Pb EFGs are discussed. Pronounced changes in the EFGs of the Pb and O atoms are seen in Section 3.3, as a function of polarization rotation and imposed symmetry. While the electric polarization lies essentially along [001] for $c/a \gtrsim 1.04$ [60], the Cm monoclinic distortions

(see Table 3.1) result in $\eta(\mathrm{Pb}) \sim 0.5$ near $c/a = 1.04$ (shown in Figs. 3.3 and 3.4), rather than zero as required by $P4mm$ symmetry. Moreover, there is about an order of magnitude difference in $V_{zz}(\mathrm{Pb})$ between $P4mm$ and Cm imposed symmetries near $c/a = 1.04$. NMR measurements cannot be used to determine Pb EFGs, since the naturally occurring isotopes have no quadrupole moment (nuclear spin $I \leq 1/2$). However, perturbed angular $\gamma - \gamma$ correlation measurements, using metastable Pb isomers, can yield information about the Pb EFGs [148–150], and they are a promising tool for investigating the striking structural sensitivity of Pb EFGs, as predicted here.

Herzog *et al.* [148] reported measurements in ferroelectric $PbTiO_3$ using metastable ^{204m}Pb, which has a half-life of about an hour. ^{204m}Pb implantation energies of 70 keV were used. Troger *et al.* [149] implanted 60 keV ^{204m}Pb or ^{204m}Bi (half-life decay = 11.2 h to ^{204m}Pb) in Cd metal, with subsequent annealing times of 0-10 min. Both ^{204m}Pb and ^{204m}Bi probes have the same intermediate ^{204m}Pb state with a half-life of 265 ns [149, 151]. Herzog *et al.* [148] reports $Q = 0.68\,(15)$ barn for the intermediate state, while the table of isotopes reports $Q = 0.44\,(2)$ barn [151]. In an unpublished report, Dietrich [152] also presented similar measurements using ^{204m}Pb implanted in $PbTiO_3$ and PZT 40/60.

In $PbTiO_3$, the experimentally measured $C_Q = eQV_{zz}/h = 64.2\,(6)$ and $65.6\,(2)$ MHz, in Refs. [148] and [152], respectively, are in good agreement with each other. A comparison between theory and experiment depends on the value of the quadrupole moment Q of the ^{204m}Pb intermediate state. Using Herzog's $Q = 0.68\,(15)$ barn and the calculated $V_{zz}(\mathrm{Pb})$ for the experimental structure in Table 3.3, $C_Q = 70\,(15)$ MHz is obtained. Using $Q = 0.44\,(2)$ barn, $C_Q = 45\,(2)$ MHz is obtained. Alternatively, using our calculated $V_{zz}(\mathrm{Pb})$ and Herzog's experimentally measured $C_Q = 64.2\,(6)$ MHz, our LDA calculations would yield $Q = 0.62\,(1)$ barn. However, first principles LAPW calculations for PbO were within 4% of the experimentally

measured C_Q, using $Q = 0.44\,(2)$ barn [150]. Herzog's [148] 1974 measurement of $C_Q = 64.2\,(6)$ MHz is the only published value for $PbTiO_3$ of which we are aware. Structural damage and incomplete annealing are certainly possible at the large 70 keV ^{204m}Pb implantation energies used by Herzog *et al.* [148] and also by Dietrich [152].

In PZT 40/60, $C_Q(\mathrm{Pb}) = 128\,(5)$ MHz was measured, with $\eta(\mathrm{Pb}) = 0.04\,(9)$ [152]. The calculated values presented here (only $Q = 0.44\,(2)$ barn is reported here, since results for other values of Q are related by a trivial scale factor) are $C_Q(\mathrm{Pb}) = 36 - 49$ MHz for Pb_1 - Pb_2 in tetragonal $P4mm$. These are characteristic for $P4mm$ imposed symmetry for the entire range of c/a, as seen in Fig. 3.3. For monoclinic Cm symmetry with $c/a = 1.045$, $C_Q(\mathrm{Pb}) = 123 - 177$ MHz is obtained. The calculated values for Cm symmetry are larger for smaller c/a, as seen in Fig. 3.3. For $P2mm$ symmetry, both Pb atoms are equivalent in our simulations, and for $c/a = 1.04$, $C_Q(\mathrm{Pb}) = 86\,(4)$ MHz is obtained. All symmetries except tetragonal $P4mm$ symmetry and Cm symmetry with $c/a = 1.0$ have sizable values of η, as seen in Table 3.2 and Fig. 3.3. Our calculations, which show large changes of $V_{zz}(\mathrm{Pb})$ between $PbTiO_3$ and PZT 50/50 and between different imposed symmetries, are consistent with the limited available experimental data. Further experimental work to assess these predictions is desirable.

The large variations of Pb EFGs arise from the strong Pb-O covalency and differences in the Pb off-centerings with respect to their nearest neighbor O atoms. These differences are evident in Fig. 3.2 and Table 3.1. Before discussing covalency effects, it is first pointed out that the EFGs of the Pb atoms as well as those of the other cations are dominated by the contributions to the Coulomb potential arising from the charge distribution near the nucleus. This is shown in Table 3.4, which presents the EFGs calculated i) using only the charge density inside the muffin-tin (MT) sphere and ii) using only the charge density outside the MT. For example the

TABLE 3.4: Electric field gradient contributions arising from the charge density inside and outside the muffin-tin (MT) spheres for monoclinic Cm PZT 50/50 with $c/a = 1.035$. V_{zz} in units of 10^{22} V/m^2.

	inside MT charges only		outside MT charges only	
	V_{zz}	η	V_{zz}	η
Pb_1	1.515	0.455	-0.0014	0.500
Pb_2	2.000	0.526	-0.003	0.367
Zr	-0.845	0.008	-0.0027	0.519
Ti	0.455	0.442	0.007	0.671
O_1	0.217	0.327	-0.097	0.093
O_2	0.265	0.525	-0.102	0.196
O_3	0.242	0.248	-0.109	0.064
O_4	-0.206	0.777	-0.084	0.333

internal EFG tensor component V_{zz} is given by [139]

$$V_{zz} = \left[\frac{4\pi}{5}\right]^{1/2} \int_0^{R_{MT}} \frac{\rho_{20}(r)}{r^3} r^2 dr, \tag{3.1}$$

where R_{MT} is the MT sphere radius and $\rho_{20}(r)$ is the $(L = 2, M = 0)$ radial coefficient in the (real) spherical harmonic decomposition of the MT charge density in the EFG principal axis frame. For the cations, Table 3.4 shows that external contributions to the EFGs are negligible compared to the internal ones, which are essentially equal to the total cation EFG (see Cm $c/a = 1.035$ in Table 3.2). For the O atoms in PZT, however, Table 3.4 shows that the external contributions are much larger. The predominance of charge distributions near the nucleus was also noted by Wei and Zunger [139] in ordered $GaInP_2$. They found that 95% of the EFG in Eq. (3.1) arises from the electron charge distribution inside a small sphere with radius of $R = 0.2$ Å. The cation EFGs in the present calculation also show predominant contributions coming from the charge distribution very close to the nuclei. As mentioned, this underscores the importance of an all-electron treatment of the electronic states near the nucleus.

TABLE 3.5: Orbital decomposition of calculated Pb EFGs for monoclinic PZT with $c/a = 1.035$. Contributions from bands with predominant Pb($5d$), Pb($6s$), O($2s$), O($2p$), Ti($3s$), Ti($3p$), Zr($4s$) and Zr($4p$) are shown. V_{zz} is in units of 10^{22} V/m^2.

	Pb $5d$		Pb $6s$	
	V_{zz}	η	V_{zz}	η
Pb_1	-2.167	0.494	0.103	0.131
Pb_2	-2.232	0.300	0.111	0.114
	O $2s$		O $2p$	
	V_{zz}	η	V_{zz}	η
Pb_1	2.185	0.506	1.430	0.494
Pb_2	2.273	0.325	1.909	0.554
	Ti $3s$		Ti $3p$	
	V_{zz}	η	V_{zz}	η
Pb_1	0	0.039	0	0.190
Pb_2	0	0.019	0	0.411
	Zr $4s$		Zr $4p$	
	V_{zz}	η	V_{zz}	η
Pb_1	0	0.298	0.005	0.438
Pb_2	0	0.536	-0.001	0.984

To examine the effects of covalency on the Pb EFGs, Table 3.5 shows the calculated orbital-decomposition of V_{zz}(Pb) and η(Pb) in PZT with imposed monoclinic Cm symmetry. The results were obtained by synthesizing the charge density, using only the energy bands corresponding to the Pb($5d$,$6s$), O($2s$,$2p$) valence states and to the Ti($3s$,$3p$) and Zr($4s$,$4p$) semi-core contributions. Since V_{zz} and η refer to the eigenvalues of the EFG tensor, the contributions in the table cannot be directly summed and compared to the total EFG. (However, the contributions from different states to each component of the EFG tensor can be summed, and the sum yields the total EFG tensor.) Nevertheless, the eigenvalues in Table 3.5 are indicative of the relative magnitude of the contributions. Thus, for example, the contributions from the Ti($3s$,$3p$) and Zr($4s$,$4p$) semi-core states are seen to be negligible. The Pb-O interaction dominates the Pb EFGs: both O 2s and 2p bands have large positive contributions to the EFGs in the monoclinic PZT, while the Pb 5d band gives large

negative contributions. Moreover, the O 2s and Pb 5d contributions to V_{zz}(Pb) and η(Pb) are seen to nearly cancel. This is verified by adding the O $2s$ and Pb $5d$ EFG tensors and then obtaining the eigenvalues. Since the Pb $6s$ contribution is small (Table 3.5), the dominant contribution to the Pb EFGs is seen to come from the O $2p$ states.

This can be understood in the context of the lone-pair picture of the Pb $6s$ orbital. In an on-site atomic orbital picture, the lone pair can be viewed as arising from the hybridization of the Pb $6s$ and unoccupied $6p$ orbital. A recent study by Payne *et al.* [153] instead attributes it to the hybridization of the Pb $6s$ lone pair and the O $2p$ electrons. The two pictures are not necessarily incompatible, since the states that are identified as predominantly O $2p$ can have Pb $6p$ character near the Pb nucleus. The calculated Pb $5d$ and O $2s$ states are more than 10 eV lower than the Fermi energy, and, as noted above, give a combined contribution to the to the Pb EFG, which is negligible. The closed-shell Pb $6s$ is also seen to give a negligible contribution. Significant Pb $6s$ - O $2p$ hybridization, however, leads to mixing in of some Pb $6p$ character, within an on-site atomic orbital decomposition, resulting in the familiar lone-pair picture. This shows up as the large O $2p$ contribution to the EFG as seen in Table 3.5.

3.4.2 Ti and O calculated EFGs and possible structural anisotropy in PZT

Recently, Baldwin *et al.* [39] presented the first NMR solid-state study of $PbZr_{1-x}Ti_xO_3$ solid-solution series as a function of x. In $PbTiO_3$ ($x = 1$), they observed two distinct ^{17}O peaks, which were unambiguously identified with the axial (650 ppm) and equatorial (450 ppm) O atoms. The evolution of these two peaks with increasing Zr concentration was quite different. While the coplanar-O peak

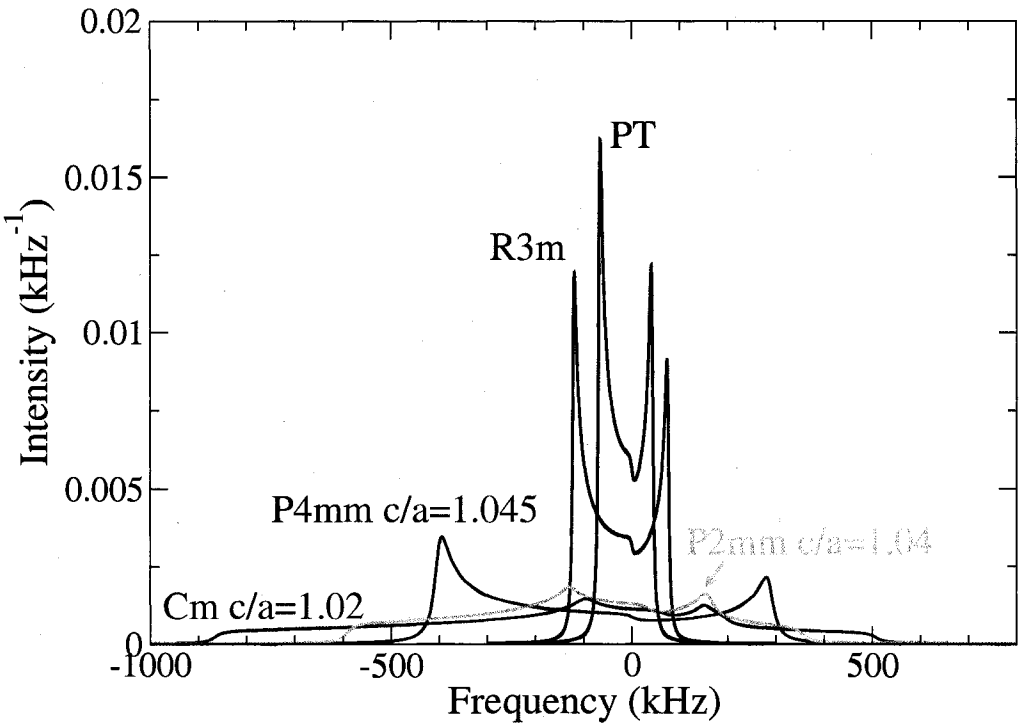

FIG. 3.14: Calculated NMR quadrupole powder spectra of ^{49}Ti: pure $PbTiO_3$ calculated at the experimental structure (black); PZT [001]1:1 tetragonal $c/a = 1.045$ (red); PZT [001]1:1 monoclinic $c/a = 1.02$ (green); PZT [111]1:1 rhombohedral (blue); PZT [001]1:1 orthorhombic $P2mm$ $c/a = 1.04$ (orange).

persisted down to $x = 0.25$ with little change in frequency, the apex-O peak disappeared for $x < 0.75$. They interpreted their measurements as indicating that Ti-O-Ti chains involving the Ti coplanar-O atoms (i.e., chains along the x and y directions, perpendicular to the c-axis) were preserved down to $x = 0.25$, while Ti-O-Ti chains involving the apex-O atoms (i.e., chains along the c-axis) were absent for $x < 0.75$. Their Ti NMR spectra, however, showed little variation over this concentration range, and this is discussed further below. Based on the above observations, they concluded that there is a local structural anisotropy in PZT. Our simulation model, based on [001]1:1 B-site ordering for $x = 1/2$, retains Ti-O-Ti chains in the [100] and [010] directions, but not along [001], where only Zr-O-Ti chains exist. Thus the interpretation of Baldwin *et al.* can be examined using our calculated EFGs for this structure. Before doing this, the calculated Ti EFGs is first discussed in some detail.

For $PbTiO_3$, the present Ti calculated EFGs are in good agreement with experiment and with other calculations [144]. Our calculated V_{zz}(Ti), using the $PbTiO_3$ structure given in the paper of Padro *et al.* [144], is in excellent agreement with their WIEN97 LAPW calculation as well as their NMR measurements. Note, however, that the calculated Ti EFGs are very sensitive to small variations in the internal structural coordinates. For example, the $PbTiO_3$ experimental structures given by Shirane and Pepinsky [154] and Glazer and Mabud [155] differ by only 0.023 Å in the Ti-O(apex) distance. The corresponding calculated V_{zz}(Ti) are -0.184 and -0.115 (10^{22} V/m^2), respectively. This difference amounts to a factor of $\simeq 2.5$ in the corresponding linewidth of the NMR central peak quadrupolar powder pattern. In this regard, we note that the reported experimental structure of the ^{17}O-doped $PbTiO_3$ sample used by Baldwin *et al.* [39] appears to be anomalous, yielding a Ti-O(apex) distance of 2.112(5) Å, which is much larger than the distance of 1.78 Å reported by Shirane and Pepinsky [154] and Glazer and Mabud [155]. It is not

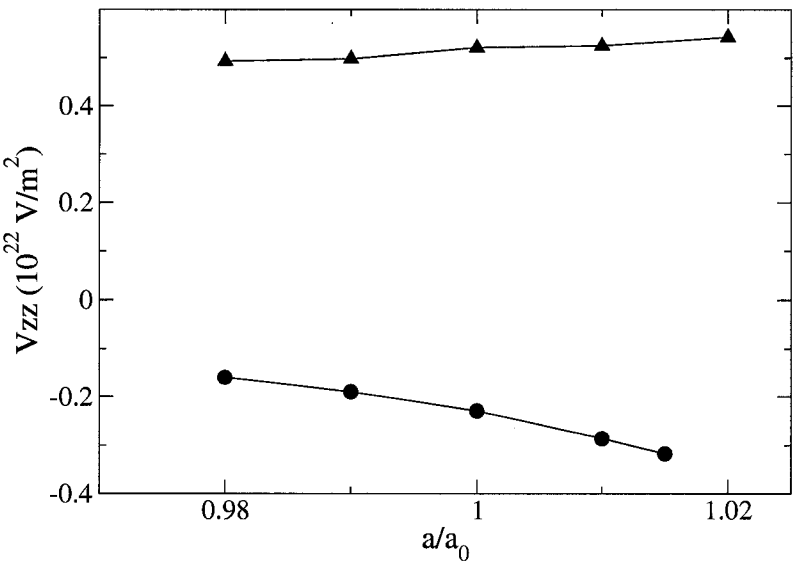

FIG. 3.15: Volume dependence of the calculated PZT 50/50 V_{zz}(Ti). Circles indicate rhombohedral $R3m$ imposed symmetry. Triangles indicate imposed tetragonal $P4mm$ symmetry with $c/a = 1.035$ PZT. The lattice parameter a_0 corresponds to the experimental volume.

clear which structure was used in their LAPW calculations.

For $PbZr_{1-x}Tixo_3$, the measured Ti spectra reported by Baldwin *et al.* [39] show very similar powder spectra for $x = 1$ (pure $PbTiO_3$), $x = 0.75$ and $x = 0.5$ (see their Fig. 5). These results indicate that the Ti EFGs are similar in all their samples over this concentration range: this is not consistent with our calculated results. Our calculated $x = 1/2$ Ti quadrupole central peak static powder spectra for monoclinic, tetragonal, orthorhombic $P2mm$, rhombohedral PZT and tetragonal $PbTiO_3$ are shown in Fig. 3.14. All, but the rhombohedral structure, have [001]1:1 B site ordering. The spectra are all seen to be much broader than that of $PbTiO_3$.

To assess this discrepancy in PZT Ti EFGs between experiment and theory, the structural sensitivity of the calculated Ti EFGs is examined in more detail. Fig. 3.15 shows, for PZT 50/50, the volume dependence of the calculated V_{zz}(Ti) for imposed tetragonal (with fixed $c/a = 1.035$) and for rhombohedral symmetries. The tetragonal [001]1:1 B-site ordered structure shows little sensitivity, while the

rhombohedral [111]1:1 B-site ordered structure shows greater variation. Sensitivity to longitudinal and shear distortions of the TiO_6 octahedra is examined next.

The longitudinal strain $|\alpha|$ of the TiO_6 octahedron [144, 156] is defined as

$$|\alpha| = \sum_{i}^{6} |\ln\left(\frac{l_i}{l_u}\right)|, \tag{3.2}$$

where l_i is the Ti-O bondlength of the distorted TiO_6 octahedron, and l_u is the undistorted bondlength corresponding to the ideal perovskite structure. Figure 3.16 shows the calculated PZT Ti V_{zz} as a function of $|\alpha|$ in imposed monoclinic Cm and tetragonal $P4mm$ symmetries. At the largest c/a values, the Ti V_{zz} have similar values in both monoclinic Cm and tetragonal $P4mm$ imposed symmetries, though the longitudinal strains $|\alpha|$ differ by about 25% at the largest $c/a = 1.055$ shown. Both symmetries show a nearly linear variation, but relaxing the $P4mm$ symmetry greatly reduces the slope. Although the onset of polarization rotation in monoclinic Cm symmetry starts at $c/a \simeq 1.035$ as c/a reduced [60], there is no indication of this in Fig. 3.16.

By contrast, the onset of polarization rotation in Cm symmetry strongly correlates with the shearing of the TiO_6 octahedra. One measure of the shear strain is the distortion index (DI) [144, 156],

$$\mathrm{DI} = \frac{\sum_{\mathrm{i=1}}^{12} |\theta_\mathrm{i} - 90°|}{\sum_{\mathrm{i=1}}^{12} 90°}, \tag{3.3}$$

where there are twelve O-Ti-O angles of 90° in the unsheared TiO_6 octahedra, while the θ_i are the angles in the distorted octahedron. Figure 3.17 shows the dependence of V_{zz}(Ti) on DI. Note that DI is non-zero in tetragonal PZT, due to the off-centering of the Ti atoms. As c/a increases in tetragonal PZT, the Ti off-centering increases.

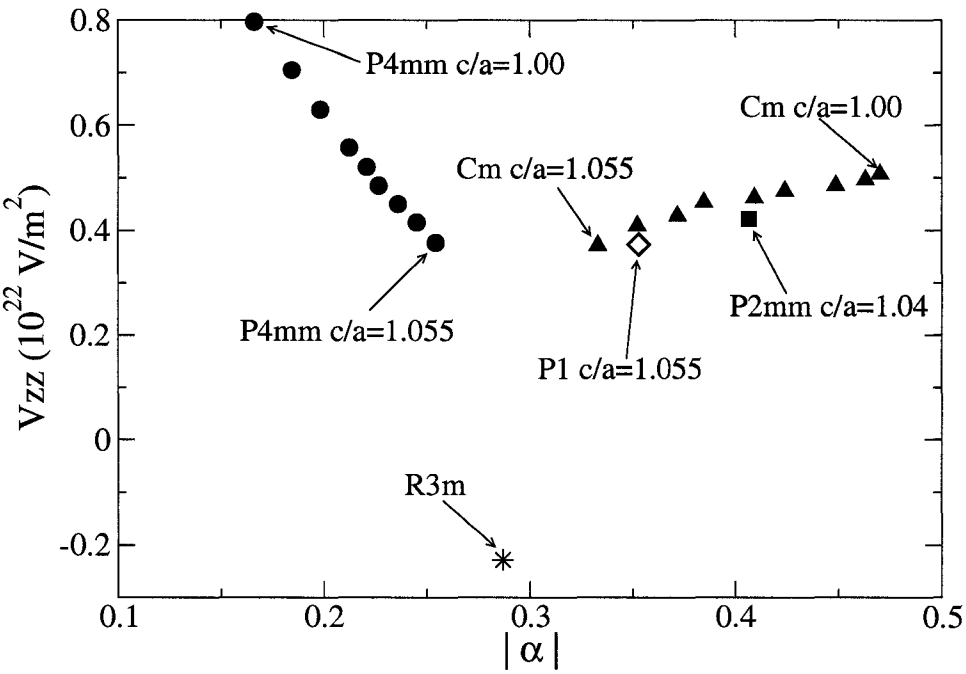

FIG. 3.16: Longitudinal strain ($|\alpha|$, see text) dependence of the calculated V_{zz}(Ti) for PZT 50/50 with different imposed symmetries: tetragonal $P4mm$ (circles), orthorhombic $P2mm$ (square), monoclinic Cm (triangles), triclinic $P1$ (diamond), and rhombohedral $R3m$ (star).

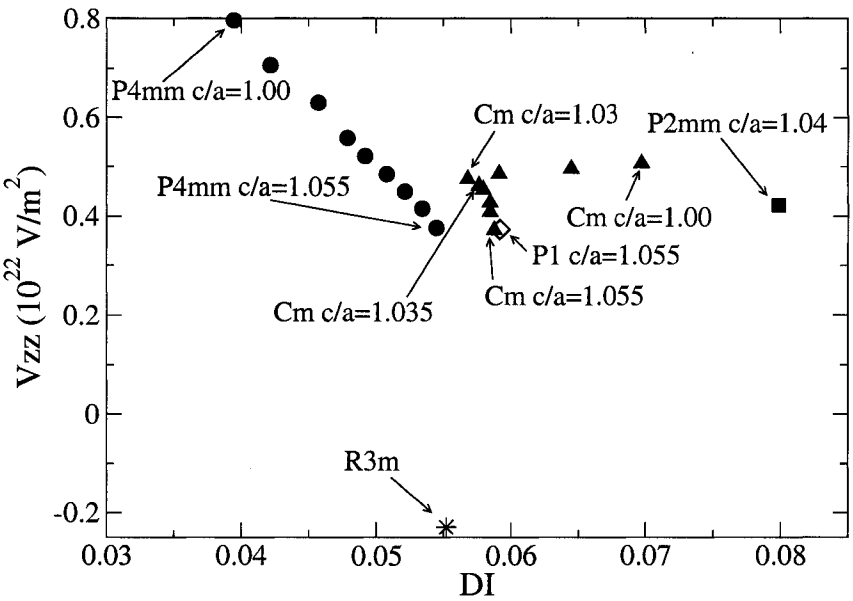

FIG. 3.17: Shear strain (distortion index DI, see text) dependence of the calculated PZT 50/50 V_{zz}(Ti) for different imposed symmetries. Same legends as in Fig. 3.16.

For imposed Cm symmetry, there is a sharp break in the slope at $c/a = 1.03$. This is caused by the abruptly larger shearing of the octahedron when the polarization rotates away from the [001] direction with decreasing c/a. For c/a values larger than 1.03, the variation of V_{zz}(Ti) with DI is similar to that in tetragonal symmetry. For smaller values of c/a, DI in Cm symmetry rapidly increases, although V_{zz} shows little change.

The discrepancy between the experimentally measured PZT 50/50 Ti spectra and the calculated spectra in Fig. 3.14 is now discussed. While the experimental spectra indicate similar η(Ti) $\simeq 0$ and similar values of V_{zz}(Ti) for 0-75% Zr compositions [39], this is not the case for the calculated spectra. The calculated EFGs (shown in Table 3.2 and Figs. 3.16 and 3.17) show that V_{zz}(Ti) in PZT 50/50 are all much larger than in $PbTiO_3$. If taking the Cm [001]1:1 B-site ordered calculated V_{zz}'s in the range $c/a < 1.03$ (Figs. 3.16 and 3.17) as representative of PZT 50/50, these values are about 2.3 times larger than that for $PbTiO_3$, corresponding to a

factor of about 5 times greater powder linewidths. Moreover, in Cm symmetry, the EFG asymmetry η(Ti) increases with decreasing c/a, which also tends to increase the linewidth, as is evident from Fig. 3.14.

One explanation is that the discrepancy results from the limitations of the present simulation cells used in the calculations (all based on two perovskite formula units) to model the disordered structure of PZT 50/50. However, the good agreement of the calculated pair distribution functions (PDF) with the experimental PDFs in Fig. 3.2 indicates that the nearest neighbor atomic structure is reasonably well reproduced. Moreover, the experimental NMR Ti spectra themselves suggest that only the nearest neighbor structure near the Ti atoms is important and that the local Ti environment changes little over the 0-75% Zr composition range. Specifically this would indicate that 1) the Ti EFG is relatively insensitive to the chemical species occupying the nearest neighbor B-site's and 2) that the TiO_6 octahedra are only slightly modified compared to $PbTiO_3$. If that is the case, however, at least one of our PZT 50/50 simulations (both [001]1:1 and [111]1:1 B-site ordering) for various c/a values and symmetries, might be expected to closely represent the Ti local atomistic structure. However, only the PZT 50/50 [111]1:1 B-site ordered $R3m$ rhombohedral model has $\eta(\mathrm{Ti}) = 0$ while at the same time having a V_{zz}(Ti) at least close in magnitude to that of $PbTiO_3$, $R3m$ V_{zz}(Ti) being only 33% larger. The experimental PDFs for rhombohedral R3c 40% Ti are quite similar to the experimental PDF of monoclinic Cm 48% Ti as seen in Fig. 3.1, while both of these show somewhat larger differences compared to the experimental PDF of $P4mm$ 60% Ti. This is also evident in the calculated PDFs for PZT 50/50 in Fig. 3.2. However, in the $R3m$ structure, which has a rock-salt like B-site ordering, there are no intact Ti-O-Ti chains.

Another possible explanation for the experimentally observed lack of structural sensitivity of the NMR Ti spectra is that the PZT spectra are motionally narrowed.

Evidence of motional narrowing in NMR quadrupole Ti spectra was recently reported in single-crystal cubic phases of the related perovskites $BaTiO_3$ and $SrTiO_3$ [157]. These were interpreted as showing the mixed order-disorder and displacive character of the ferroelectric transition. The motional narrowing was interpreted as arising from a fast motion between eight nearly degenerate [111] off-centerings, with a slight bias, on a slower time scale, toward a local tetragonal polarization along a cubic direction. In PZT, motional narrowing would be possible if there were several local structures which were energetically nearly degenerate. The relative ease of polarization rotation, which is responsible for the high piezoelectric constants in PZT and PMN-PT, reflects just such a soft energy landscape. For example, the energies of the PZT Cm $c/a = 1.02$ and the $P4mm$ $c/a = 1.045$ structures differ only by about 1 mRy/perovskite-unit.

The suggestion by Baldwin *et al.* [39] of an anisotropy in the local structure of PZT solid solutions can now be evaluated. Their interpretation is based on 1) very similar Ti NMR spectra for 0-75% Zr concentration and 2) the disappearance of one of the two ^{17}O peaks (observed in pure $PbTiO_3$) for Zr compositions as small as $\simeq$ 25%. Due to the small ^{17}O quadrupole moment and relatively small EFGs, the observed ^{17}O lines are very narrow. (This is also evident in the small widths of the simulated O spectra in Figs. 3.10-3.13 compared to that of the other atoms.) These peaks are located at about 650 and 450 ppm (referenced to liquid water). Since the intensity of the 450 ppm peak is twice that of the 650 ppm peak, the 450 ppm peak was assigned to the O equatorial site, and the 650 ppm peak was assigned to the O apex site. The $\simeq$ 200 ppm difference is due to different chemical shieldings at the apex and equatorial sites (EFG central peak centroid shifts are negligible due to the small magnitudes of O EFGs). The disappearance of the 650 ppm peak with the addition of small concentrations of Zr atoms was interpreted as being due to the elimination of Ti-O-Ti chains along the z-axis (polar axis), while the

persistence of the 450 ppm peak up to about 75% Zr was interpreted as reflecting the presence of Ti-O-Ti chains along the x and y axes. While the calculation of chemical shielding is beyond the scope of the present work, the structural sensitivity of $V_{zz}(\mathrm{O})$ and $\eta(\mathrm{O})$ can be examined to infer information about changes in the O-site local environments. The $V_{zz}(\mathrm{O})$ for the O_2 and O_4 equatorial atoms show little change with c/a in imposed Cm symmetry, as shown in Figs. 3.3, 3.4, 3.7, and 3.10-3.13. The $\eta(\mathrm{O})$ for the O_4 equatorial atom (roughly coplanar with Ti) decreases with increasing c/a, while the O_2 atom (roughly coplanar with Zr) shows little change. By contrast, the apex O_1 and O_3 atoms show much larger changes in $V_{zz}(\mathrm{O})$ and $\eta(\mathrm{O})$. This is most clearly seen in Figs. 3.7, 3.12, and 3.13. Thus, the calculated EFGs for the apex O atom show considerable sensitivity to their local environment. Assuming that significant chemical shielding variations accompany the large EFG changes, this suggests that the introduction of Zr is likely to more strongly affect the apex O, which is consistent with the measurements of Baldwin *et al.* [39] This interpretation would favor a structure similar to our PZT 50/50 [001]1:1 model. However, the calculated Ti EFGs yield central peak NMR static powder patterns (in Fig. 3.14) much wider than observed, unless motional narrowing is invoked.

The persistence of the 450 ppm peak may not require, however, the persistence of Ti-O-Ti chains in the x and y directions. In $PbTiO_3$, the Ti-O-Ti x and y chains have equal B-O bondlengths, while the z chains have alternating short and long B-O bondlengths. In PZT 50/50, with either [001]1:1 or [111]1:1 order, there are still Ti-O bondlengths roughly equal to those in the Ti-O-Ti x and y chains. The 450 ppm peak could be associated with these. The disappearance of the 650 ppm peak could be accounted for if large changes in chemical shielding accompany the large structural dependence of the apex O EFGs found in the present calculations. To explain the observed insensitivity of the Ti NMR spectra over the large PZT composition range, it is possible that, for Zr concentrations greater than about 40%, the local Ti

structure is similar, on average, to that of our [111]1:1 ordering model. Indeed, this structure has the lowest energy of all the structures examined here. Moreover, the experimental and calculated PDF curves suggest that the rhombohedral $R3m$ and Cm nearest neighbor arrangements are quite similar (Figs. 3.1 and 3.2). V_{zz}(Ti) in local $R3m$ symmetry is reasonably close to that in $PbTiO_3$ for both and with $\eta(\mathrm{Ti}) = 0$. A reduction in the effective volume of the TiO_6 octahedra in local $R3m$ symmetry (see Fig. 3.15) or some motional narrowing could reduce the V_{zz}(Ti) to that of $PbTiO_3$. In this scenario, there are no Ti-O-Ti chains, and there is no structural anisotropy in PZT.

There are thus several possible interpretations of the NMR measurements of Baldwin *et al.* [39] Their interpretation of a structural anisotropy in PZT would seem to rule out local $R3m$ [111]1:1 B-site ordering, since no Ti-O chains are present in the $R3m$ structure. This is inconsistent with the present Ti EFG calculations, which yield too large Ti EFGs and non-zero η's for all Ti local structures in a static structural model. If motional narrowing of the Ti EFGs were present, however, this could resolve the discrepancy with the present calculations. Alternatively, an average local $R3m$ [111]1:1 B-site ordering, perhaps accompanied by less pronounced motional narrowing, would also be consistent with the present calculations, without invoking any static structural anisotropy in PZT. In this case, as mentioned, the persistence of the 450 ppm NMR peak could be accounted for by the presence of Ti-O bond lengths similar to that of the coplanar O atoms in $PbTiO_3$ at all compositions of the solid solution. The disappearance of the 650 ppm peak could be due to large structural dependence of the apex O chemical shielding, paralleling the large structural dependence of the calculated apex O EFGs.

Chapter 4

EFG calculations in PST, PSW, and PMN

The last chapter showed electric field gradient (EFG) calculations on 1:1 B-site ordered PZT (50/50), containing homovalent Zr^{4+} and Ti^{4+} cations. In this chapter, calculations are focused on $Pb(Sc_{1/2}Ta_{1/2})O_3$ (PST), $Pb(Sc_{2/3}W_{1/3})O_3$ (PSW) and $Pb(Mg_{1/3}Nb_{2/3})O_3$ (PMN). The B-sites of PST are occupied by heterovalent Sc^{3+} and Ta^{5+} cations with 1:1 distribution, thus PST can provide a contrast to PSW and PMN, which both have heterovalent B-sites with 2:1 stoichiometry.

In the beginning of this chapter, various structural models with different chemical orderings and symmetries are presented for PST, PSW and PMN as well as the technical details of the evaluation of EFGs (Section 4.1). The structures of these models are then compared to the neutron scattering experimental measurements in Section 4.2. Section 4.3 shows the EFG results of PST, PSW and PMN, which are compared to those of PZT in order to examine the effect of different B environments. In the previous calculations of PZT, the off-centerings of Ti showed some sensitivity to the local structures and electric polarization rotation. Since Pb

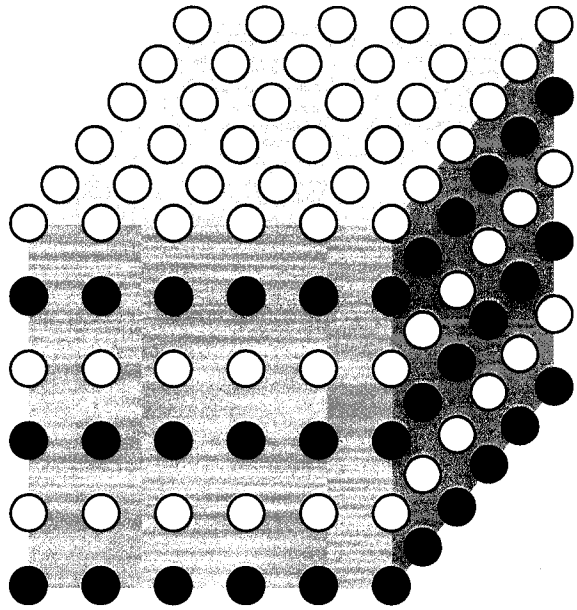

FIG. 4.1: PST 10-atom supercell with [001]1:1 B-site ordering. The open and solid circles indicate Sc and Ta atoms, respectively. Triangles indicate [111] planes.

off-centering correlates strongly with the electric polarization, Pb off-centerings in PST and the off-centering of B atoms in PST, PSW and PMN are presented in Section 4.4. The simulated NMR quadrupole spectra based on the calculated EFGs are shown in Section 4.5. The Sc spectra in PST and PSW and the Nb spectra in PMN are compared with NMR measurements.

4.1 Simulation procedure

The 10-atom PST unit cells were constructed by arranging the layers occupied purely by Sc or Ta alternatively along the [001] direction, which is also the ferroelectric polarization direction. For these supercells, various strain c/a's were applied, as tetragonal $P4mm$ and monoclinic Cm symmetries were imposed. The PST supercell with [111] B-site ordering and rhombohedral $R3m$ symmetry was also studied. In this model, Sc and Ta atoms formed a rocksalt structure and the ferroelectric

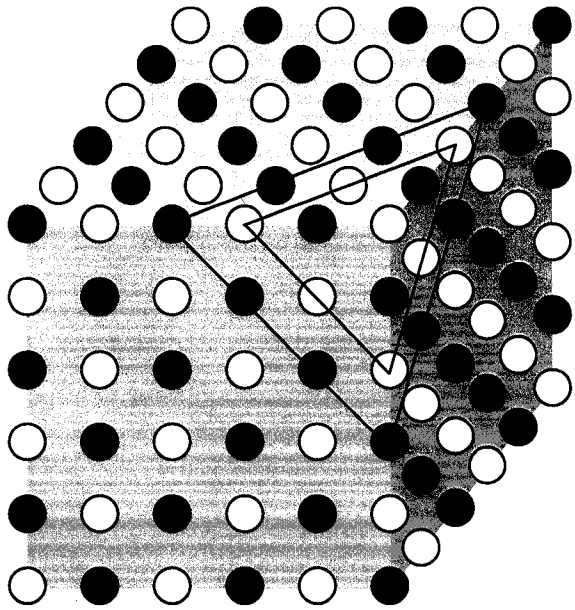

FIG. 4.2: PST 10-atom supercell with [111]1:1 B-site ordering. The open and solid circles indicate Sc and Ta atoms, respectively. Triangles indicate [111] planes.

polarization is oriented along [111] direction. The PST structures with different B-site chemical orderings are shown in Figs. 4.1 and 4.2.

As for ordered PSW supercells, the B-site 2:1 stoichiometry requires at least 15 atoms in each supercell. In the present calculations, two 15-atom supercells and two 30-atom supercells were considered. In the 15-atom unit cells, two pure layers of Sc and one pure layer of W alternate along the [111] direction, as shown in Fig. 4.3. Calculations with both Pm and $P1$ imposed symmetries were carried out. The 30-atom supercells are consistent with the "random site" model [69], where one B-layer is completely occupied by Sc atoms and the other is occupied by Sc and W atoms in a 1:2 ratio, as indicated in Fig. 4.4. With different arrangements of the Sc and W atoms in the mixed layer, two base structures are possible in the 30-atom PSW cells, having either $Immm$ or $I4/mmm$ symmetry when all atoms are at their ideal perovskite positions. The two 30-atom PSW unit cells considered here were generated from the ideal $Immm$ and $I4/mmm$ structures by allowing the

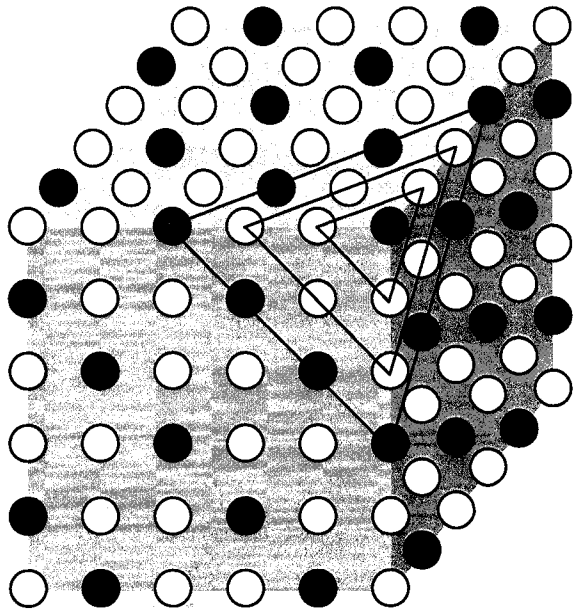

FIG. 4.3: PSW 15-atom supercell with [111]2:1 B-site ordering. The open and solid circles indicate Sc and W atoms, respectively. Triangles indicate [111] planes.

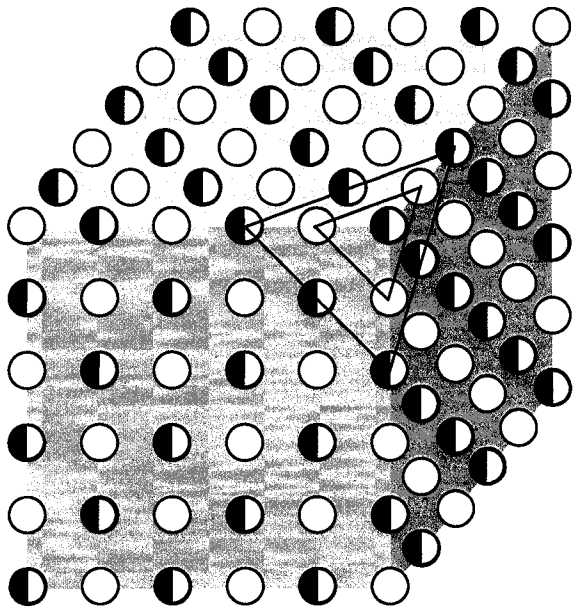

FIG. 4.4: PSW 30-atom supercell with "random site" B-site ordering. The open circles indicate pure Sc sites and half-filled circles represent B sites occupied by Sc and W atoms in a 1:2 distribution, respectively. Triangles indicate [111] planes.

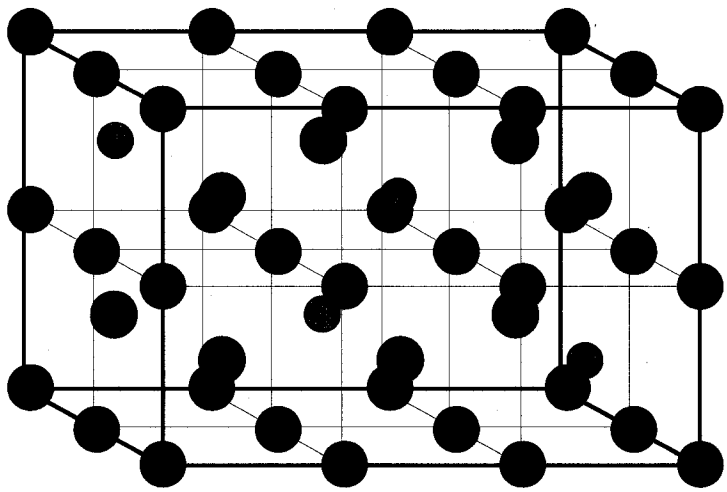

FIG. 4.5: PMN 60-atom supercell [158]. Black, blue, and red represent Pb, Nb and Mg atoms, respectively.

atom positions to relax in $P1$ symmetry. To avoid confusion, they are never the less referred to as $Immm$ and $I4/mmm$ in the following.

A 3×2×2 60-atom unit cell (shown in Fig. 4.5) was constructed by Rappe *et. al.* [158] for PMN with atoms arranged consistent with the "random-site" model.

In order to achieve better scaling than the LAPW method, the atomic positions in all the PST and PSW supercells have been optimized using the first-principles pseudopotential method. The structural relaxations were obtained keeping experimental volumes for PST [27] and PSW [27]. All the atomic forces were minimized to less than 0.04 eV/Å through the use of the open-source ABINIT code. The pseudopotentials implemented in the ABINIT program [120] were the optimized pseudopotentials [131] generated by the open-source OPIUM code [132]. The PMN unit cell was relaxed by Rappe *et al.* [158] at its experimental volume [159].

The LAPW plus local orbital (LAPW+LO) method [135] is used to calculate

the EFGs for PST, PSW and PMN at the experimental volumes. Local orbitals were included with the s, p, d orbitals for all cations and only s and p states for O. The Hedin-Lundqvist exchange-correlation functional [106] was used for the local density approximation. The muffin-tin radii for Pb, Sc, Ta, W, Mg, Nb and O were 2.3, 1.65, 1.70, 1.70, 1.55, 1.65 and 1.55 a. u. , respectively. A well-converged energy cutoff of 49 Ry was applied for the plane waves. To sample the Brillouin zone, a special 6×6×4 **k** point grid [125] was used for PST, PSW, and a $2 \times 2 \times 2$ grid for PMN.

4.2 Structural pair distribution function results

4.2.1 PST

The simulated pair distribution functions (PDF) obtained using our calculated relaxed atomic positions of PST as input into the PDFFIT program [143] are displayed in Fig. 4.6. The simulations used $Q_{max} = 80$ Å^{-1}, and a thermal factor of 0.005 Å^2 for Pb and O atoms, 0.001 Å^2 for Sc and Ta atoms. The relaxed structural models can be compared to experimentally determined PDFs. The experimental PDFs were obtained from Fourier transform of neutron scattering structure factors from a nominally ordered PST (87% B site ordering) at 300 K by Dmowski *et al.* [27]. The average symmetry observed from the experiment is cubic $Fm3m$ with a macroscopic polarization along [111] axis. The PST supercells with imposed monoclinic Cm, tetragonal $P4mm$ and rhombohedral $R3m$ symmetries with $c/a = 1.0$ all agree very well with the neutron scattering PDF results. The first peak centered at ~2.0 Å reflects the B-O distances. The peak centered at ~2.9 Å reflects the ideal perovskite Pb-O bondlength in PST. In all three of the simulated PDFs, the Pb-O peaks split into three, around 2.4, 2.9, and 3.4 Å, respectively. The splitting

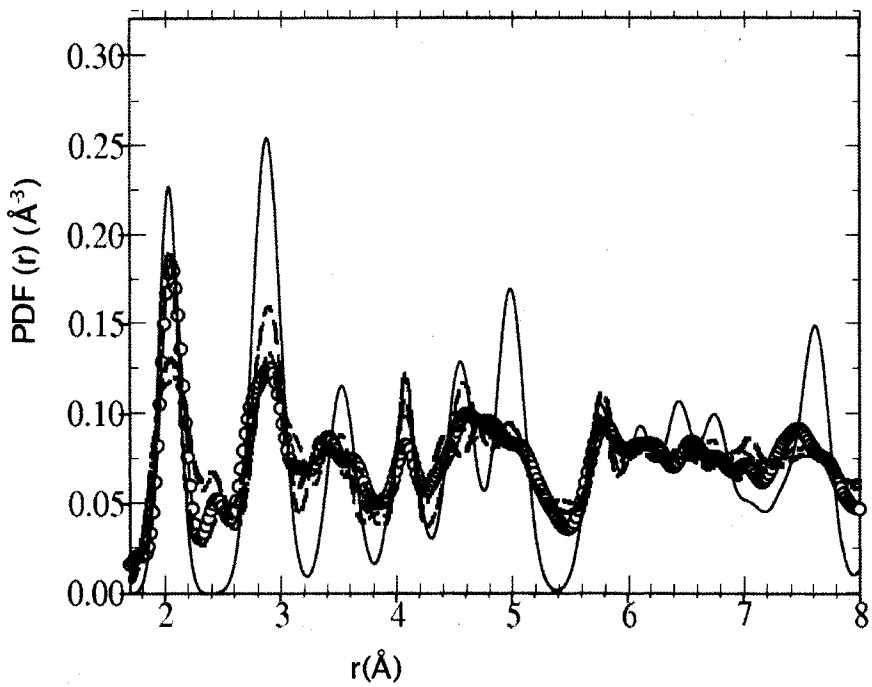

FIG. 4.6: PST experimental pair distribution functions (PDF) at $T = 300$ K [black open circles] from Dmowski *et al.* [27] are compared to simulated PDFs, calculated using the ideal perovskite structure [solid (black) curve] as well as the relaxed atomic positions (see text) with imposed monoclinic Cm [red line] tetragonal $P4mm$ [green line] and rhombohedral $R3m$ [blue line] symmetries at $c/a = 1.0$.

TABLE 4.1: PST Pb-O nearest-neighbor distances (Å) for Cm monoclinic and $P4mm$ tetragonal imposed symmetries. c/a values correspond to Fig. 4.6, and m refers to the number of bonds of the given length.

Cm c/a=1.0				$P4mm$ c/a=1.0			
Pb_1-O	m	Pb_2-O	m	Pb_1-O	m	Pb_2-O	m
2.307	1	2.374	1	2.744	4	2.501	4
2.452	2	2.449	2	2.882	4	2.948	4
2.858	2	2.866	2	3.024	4	3.309	4
2.949	2	2.950	2	–	–	–	–
3.071	2	3.067	2	–	–	–	–
3.262	2	3.268	2	–	–	–	–
3.432	1	3.430	1	–	–	–	–

of the Pb-O peak indicates the displacement of Pb atoms from its ideal perovskite positions. The Pb-B peak, ideally at 3.52 Å, in the simulated and measured PDFs split into two, corresponding to different Pb-Sc/Ta distances. The shortest Pb-Sc and Pb-Ta lengths differ by about 0.34 Å in Cm PST with c/a=1.0, which agrees with the experimental result of 0.4 Å, while in $P4mm$ and $R3m$ PST the separations are 0.2 Å and 0.15 Å, respectively. This splitting of the Pb-B peak was not seen in either the PZT neutron scattering experiment or our previous first-principles PZT calculations.

A generic feature of many lead-based perovskite alloys is the wide range of Pb-O nearest-neighbor bond lengths. The Pb-O nearest-neighbor bond lengths in both tetragonal and monoclinic imposed symmetries for the relaxed structures are shown in Table 4.1. In tetragonal symmetry, there are four groupings of Pb-O bond lengths: $\sim$ 2.5, 2.7, 2.9, and 3.3 Å. In imposed monoclinic Cm symmetry, the Pb-O groupings are more spread out. The experimental and theoretical curves in Fig. 4.6 both show peaks at $\sim$ 2.5, 2.9, 3.2 Å and a shoulder at $\sim$ 2.7 Å, corresponding to these Pb-O distances. These features, especially the peak near $\sim$ 2.5 Å, are also evident at the other compositions. The presence of the 2.5 Å bond length, similar

to the shortest Pb-O distance in $PbTiO_3$, is characteristic of PZT and many other perovskite lead-based alloys, as noted by Dmowski *et al.* [27]

Based on comparisons with model PDFs, Dmowski *et al.* [27] concluded that over short distances Pb atoms tend to have $\langle 100 \rangle$ pseudocubic displacements though the overall Pb polarization is along $\langle 111 \rangle$ direction. This is consistent with our tetragonal $P4mm$ calculations where Pb atoms move along $\langle 001 \rangle$ direction only, and our monoclinic Cm calculations, which show that the Pb atoms move toward one side of the oxygen octahedra and displace between the $\langle 111 \rangle$ and $\langle 001 \rangle$ directions.

4.2.2 PSW

The simulated PDFs obtained using the calculated relaxed atomic positions of PSW unit cells are displayed in Fig. 4.7 and fig. 4.8. The simulations used $Q_{max} = 80$ Å^{-1} for all the structures. Thermal factors of 0.0125, 0.00125, and 0.0075 Å^2 were used for Pb, Sc/W, and O atoms separately in 15-atom PSW, while 0.0025, 0.0002, and 0.0015 Å^2 were used respectively for these atoms in 30-atom PSW. The simulated PDFs of the 15-atom PSW supercells show very poor agreement with the experimental neutron scattering PDF results [158], as seen in Fig. 4.7. The measured B-O peak at 2.1 Å and the Pb-O peaks between 2.3 to 3.3 Å are barely reproduced by the calculated PDFs. On the other hand, the PDFs of PSW unit cells with 30 atoms and $P1$ symmetry agree much better with the experiment [158] (Fig. 4.8). This supports the "random site" structure in disordered PSW.

The first peak in the measured PDF figure at 2.1 Å reflects the B-O distance in PSW, and the B-O peaks in the PDFs of the 30-atom PSW supercells agree well with the experiment in both height and width (Fig. 4.8). The B atoms in both $I4/mmm$ and $Immm$ supercells have very small displacement from their ideal cubic positions. All Sc atoms move less than 0.13 Å away from their average positions,

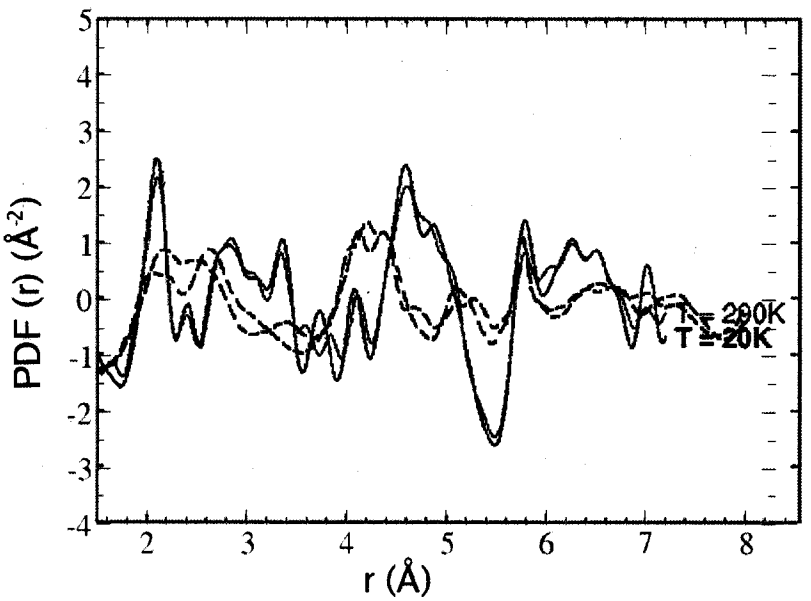

FIG. 4.7: PSW experimental pair distribution functions (PDF) at $T = 20$ K and 290 K [solid (black) curves] from Juhas *et al.* [158] are compared to simulated PDFs, calculated using the relaxed atomic positions (see text) of 15-atom monoclinic Pm (dashed green) and $P1$ (dashed red) PSW.

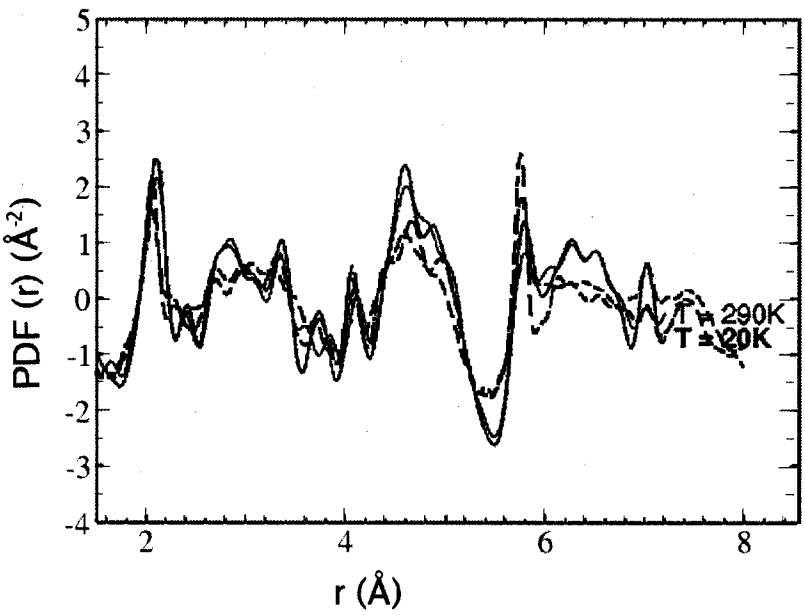

FIG. 4.8: PSW experimental pair distribution functions (PDF) at $T = 20$ K and 290 K [solid (black) curves] from Juhas *et al.* [158] are compared to simulated PDFs, calculated using the relaxed atomic positions (see text) of 30-atom $I4/mmm$ (dashed blue) and $Immm$ (dashed red) PSW.

W atoms move less than 0.08 Å. These small off-center distortions agree with the experimental observations. On the other hand, the ideal Pb-O distance around 3.0 Å splits into at least three peaks in both $Immm$ and $I4/mmm$ supercells, which is caused by the largely dispersive Pb-O bondlength from 2.3 Å to 3.3 Å. The shortest 2.3 Å Pb-O bond-length is also seen in Cm PST. Pb atoms also experience large off-centerings, ~0.5 Å, against the O-cage around them, while the B atom off-centerings against their surrounding oxygen octahedra are ~0.2 Å. These off-centerings are compatible to those in PST supercells.

4.2.3 PMN

The comparison between the PDFs obtained from the 60-atom PMN super cell and that from neutron scattering experiment [160] is shown in Fig. 4.9. The simulation used $Q_{max} = 80$ Å^{-1}, and an isotropic thermal factor of 0.0025 Å^2 for all the atoms. In Fig. 4.9, the structure near 2.85 Å corresponds to the Pb-O distances, ideally 2.88 Å, which splits into three peaks at ~ 2.5, 2.85, and 3.3 Å. The Pb-B peak ideally at around 3.5 Å also splits into two, at 3.3 and 3.6 Å separately. These splittings show that all ions displace strongly from their ideal cubic positions.

The good agreement of the calculated PDFs with experiments for PST, PSW and PMN indicates that the nearest neighbor atomic structure is reasonably well reproduced in all the relaxed simulation cells, except for the 15-atom PSW supercells.

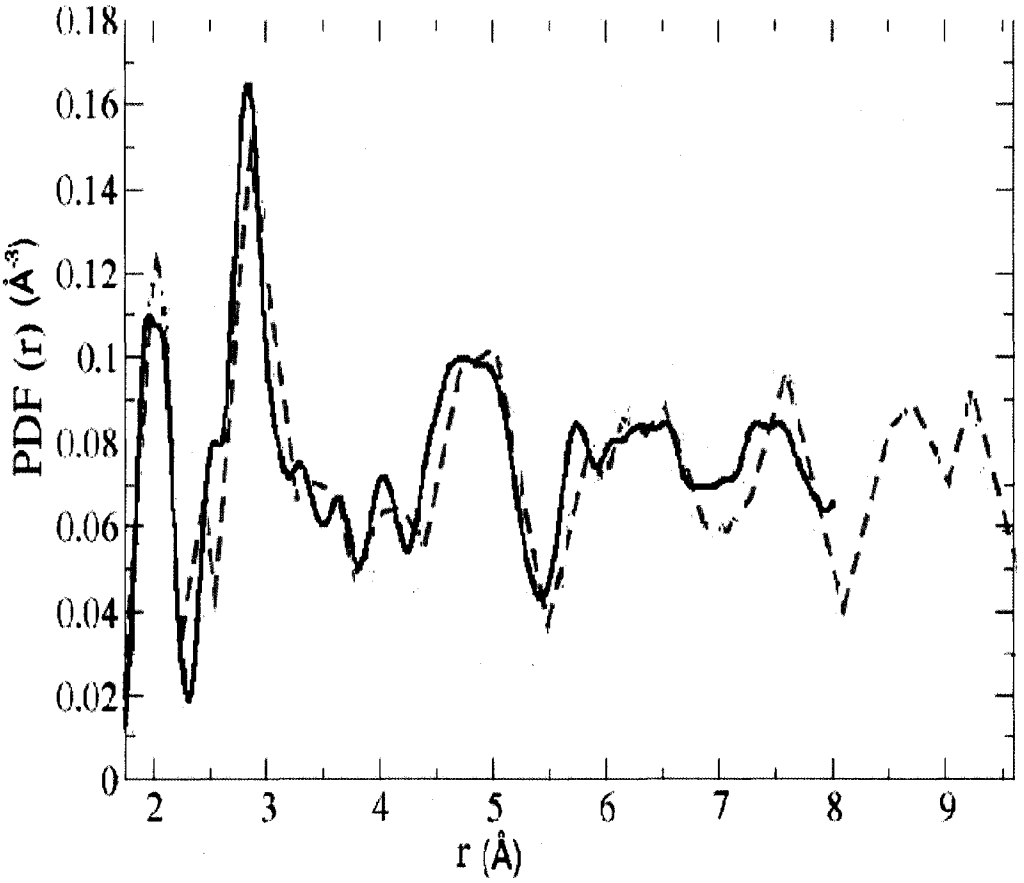

FIG. 4.9: Simulated PDF from relaxed PMN supercell [solid black curve] is compared to PDF from neutron scattering experiment [red dashed curve] [160].

4.3 EFG results

4.3.1 PST

Calculated EFGs for all atoms in [001]1:1 ordered PST supercells with imposed monoclinic Cm and tetragonal $P4mm$ symmetries are shown as a function of the strain c/a in Figs. 4.10 and 4.11. The atoms were labeled as following: In monoclinic Cm symmetry, both Pb_1 and Pb_2 are closer to Sc than to Ta, but the Pb_1 atom has a smaller Pb-Ta bond length than Pb_2 atom. For example, at $c/a = 1.04$ and with Cm symmetry, the Pb_1-Ta distance is 3.34 Å, and the Pb_2-Ta bondlength is 3.74 Å. In tetragonal $P4mm$ symmetry, Pb_1 is closer to Ta and Pb_2 to Sc. In both Cm and $P4mm$ symmetries, apex (c-axis) oxygen atoms O_1 and O_3 have the shortest B-O distance with the Ta and Sc atoms, respectively. The O_2 and O_4 atoms are roughly coplanar with the [001]-layers of Sc (Ta), respectively. In Cm symmetry with c/a less than 1.02, Pb_1 and Pb_2 move closer to Sc and have very similar distances to every B atom, corresponding to very similar V_{zz}(Pb) and η(Pb) values. As c/a increases from 1.02, Pb_1 reorients to a position with almost equal distance to Sc and Ta (slightly favors Sc), while Pb_2 moves closer to Sc and away from Ta. The different Pb-B displacements result in the split of V_{zz}(Pb) and η(Pb) values at $c/a \geq 1.02$, as can be seen in Figs. 4.10 and 4.11. It is also reflected in the Pb off-centering against its O_{12} cage, which will be discussed in section 4.4.2. By contrast, as c/a changes in $P4mm$ symmetry, Pb_1 stays close to Ta and Pb_2 close to Sc, unlike in Cm symmetry. Consequently, the EFG of Pb_2 atom in Cm PST approaches its value in $P4mm$ structure as c/a increases to 1.135, while $V_{zz}(Pb_1)$ and $\eta(Pb_1)$ are still rather different from their $P4mm$ values even at the largest $c/a = 1.135$. In the previous calculations of PZT(50/50) (Chapter 3), V_{zz}'s and η's of all B cations and O atoms in Cm supercells approached their $P4mm$ values at c/a as large as

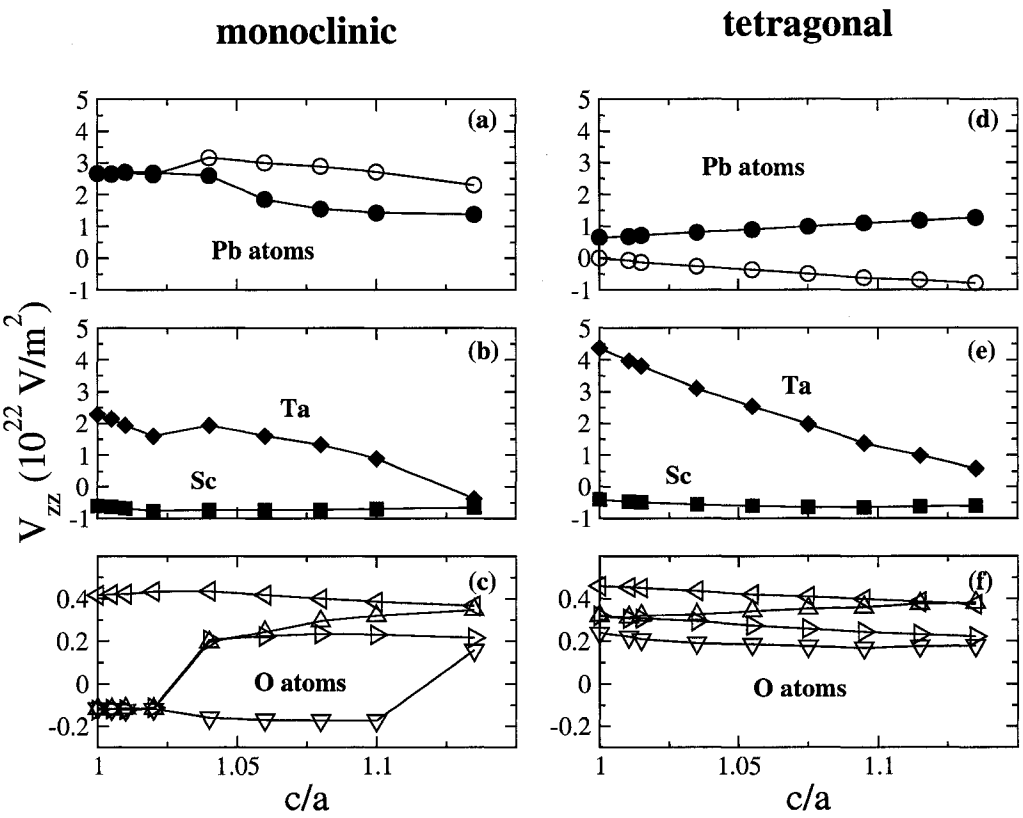

FIG. 4.10: Calculated V_{zz} vs c/a for PST. Panels (a)-(c) are for imposed monoclinic Cm symmetry, and panels (d)-(f) are for tetragonal $P4mm$ symmetry. In (a) and (d), open (filled) circles represent Pb_1 (Pb_2), respectively (see text). In (b) and (e), squares (diamonds) represent Sc (Ta), respectively. In (c) and (f), triangles pointing up, down, left, and right represent oxygen atoms O_1, O_3, O_2, and O_4, respectively (see text). Note the change of scale for the O atoms.

1.055. In Cm PST, only the V_{zz}'s and η's of Sc, O_1, and O_2 approach their $P4mm$ at c/a at 1.055, the EFGs of Ta and other oxygens are still very different from their $P4mm$ values at much larger $c/a = 1.135$. For c/a less than 1.02 in Cm PST, the two axial oxygens, O_1 and O_3 have very similar V_{zz} and η values, consistent with Pb_1 and Pb_2 having very similar EFGs.

Numerical results of EFGs for all atoms in PST at selected c/a values are displayed in Table 4.2. $V_{zz}(Pb_1)$ in Cm PST has large values, over 2.2 (10^{22} V/m^2), for all strains, while $V_{zz}(Pb_2)$ decreases to about 1.5 (10^{22} V/m^2) as c/a over 1.05. While $\eta(Pb_2)$ decreases to nearly 0 with increasing c/a, $\eta(Pb_1)$ remains as large as

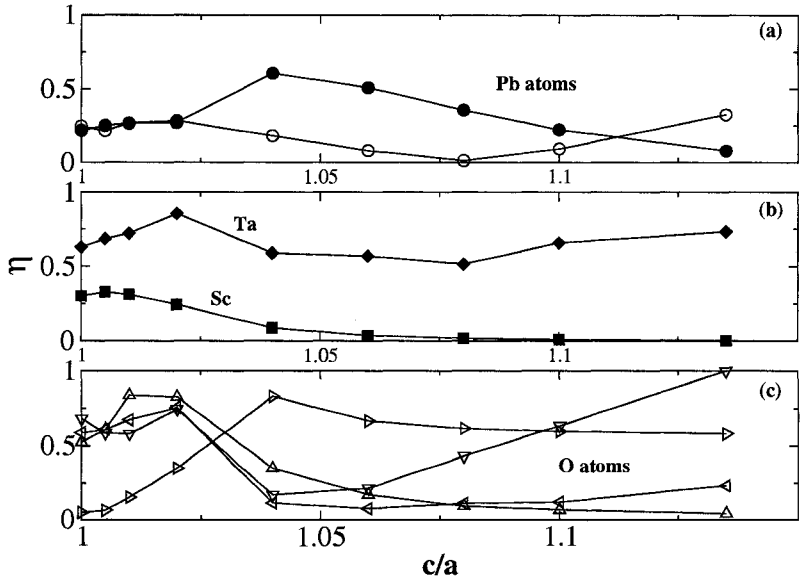

FIG. 4.11: Calculated EFG asymmetry for PST with imposed monoclinic Cm symmetry. Panels (a)-(c) show η vs c/a for monoclinic Cm PST. Symbols are the same as in Fig. 4.10.

0.3 at c/a=1.135. Such difference in the Pb EFGs are consistent with the differences in Pb-B displacements mentioned above.

To help understand the structural dependence of the calculated EFGs, it is helpful to examine the orientation of the EFG principal axes eigenvectors. Note that, by symmetry, one of the eigenvectors of the EFG tensors must be perpendicular to the Cm mirror plane; we label the corresponding eigenvalue $V_\perp$. The other two

TABLE 4.2: Calculated EFGs (V_{zz}) in units of 10^{22} V/m^2 for monoclinic Cm, tetragonal $P4mm$, and rhombohedral $R3m$ PST.

	Cm						$P4mm$				$R3m$	
	$c/a = 1.0$		$c/a = 1.04$		$c/a = 1.135$		$c/a = 1.00$		$c/a = 1.135$		$c/a = 1.0$	
	V_{zz}	η	V_{zz}	η	V_{zz}	η	V_{zz}	η	V_{zz}	η	V_{zz}	η
Pb_1	2.666	0.244	3.159	0.181	2.296	0.324	-0.005	0	-0.787	0	2.880	0
Pb_2	2.668	0.217	2.599	0.607	1.373	0.079	0.653	0	1.267	0	1.937	0
Sc	-0.598	0.303	-0.733	0.088	-0.663	0.003	-0.403	0	-0.603	0	-0.159	0
Ta	2.276	0.628	1.935	0.588	-0.375	0.661	4.371	0	0.573	0	-0.934	0
O_1	-0.118	0.523	0.196	0.350	0.348	0.043	0.320	0	0.381	0	-0.123	0.261
O_2	0.416	0.587	0.435	0.113	0.367	0.232	0.459	0.402	0.373	0.141	-0.123	0.261
O_3	-0.115	0.681	-0.161	0.168	0.158	0.999	0.239	0	0.178	0	-0.160	0.990
O_4	-0.124	0.049	0.206	0.829	0.216	0.581	0.319	0.358	0.222	0.318	-0.160	0.990

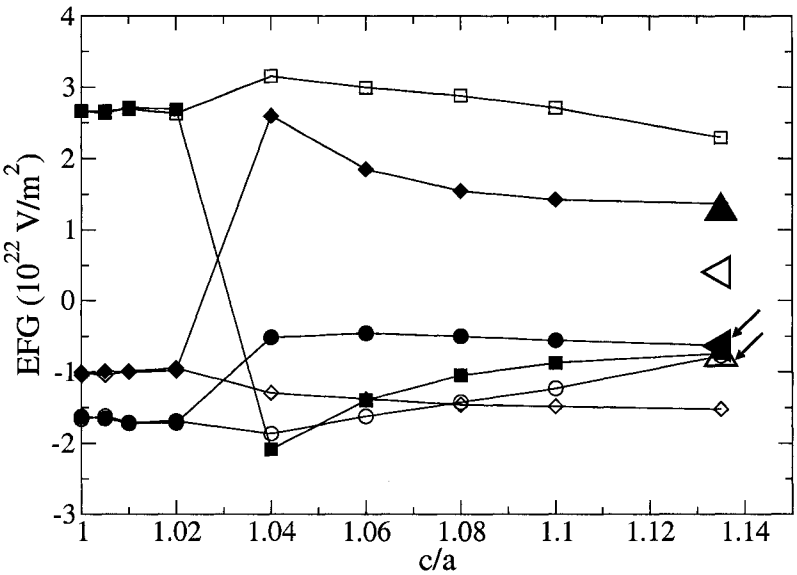

FIG. 4.12: Pb "projected" EFG eigenvalues (see text) vs c/a: circles label $V_\perp$, the EFG eigenvalue for the eigenvector that is perpendicular to the Cm mirror plane; diamonds label V_c, the EFG eigenvalue for the eigenvector that is approximately parallel to the c-axis; squares label $V_\parallel$, the EFG eigenvalue for the remaining eigenvector. The large up-triangles and left-triangles at $c/a = 1.135$, which are identified by arrows for clarity in some cases, represent the conventional EFG eigenvalues calculated in imposed $P4mm$ symmetry: V_{xx}=V_{yy} (left-triangles) and V_{zz} (up-triangles). All open symbols are for Pb_1, and filled symbols are for Pb_2.

eigenvectors necessarily lie in the mirror plane. Of these two eigenvectors, the one with the larger dot product with the [001] unit vector (c axis) has its eigenvalue labeled V_c, and the other is labeled $V_\parallel$. In the following we refer to $V_\perp$, $V_\parallel$, and V_c as "projected" EFG eigenvalues.

The projected eigenvalues for the Pb cations are plotted in Fig. 4.12. The largest EFG component of Pb_1 is $V_\parallel$ for all c/a values, while that of Pb_2 changes its orientation from parallel to the Cm plane at $c/a < 1.02$ to the c direction at larger c/a's. As in Cm PZT, the directions of V_{zz} for both Pb atoms are along the c axis for all c/a's.

The projected B-atom EFG eigenvalues are plotted in Fig. 4.13. The largest EFG components of both Sc and Ta are along the c direction for all c/a's in [001] or-

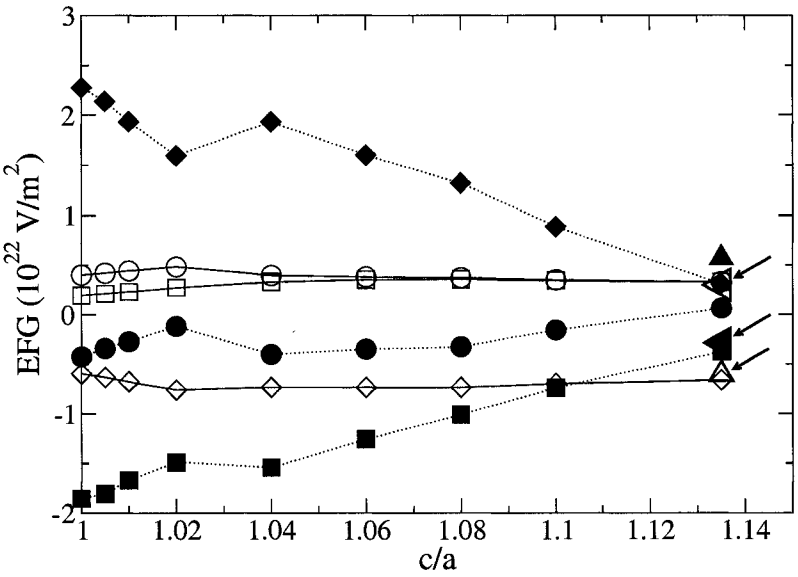

FIG. 4.13: Same as Fig. 4.12, but for Sc and Ta "projected" EFG eigenvalues (see text). All open symbols are for Sc, and filled symbols are for Ta.

dered Cm PST, and the same behavior was found for Zr and Ti in Cm PZT(50/50) supercells. The V_{zz}(Sc)'s and η(Sc)'s are similar to those of the Ti in PZT(50/50) with the same symmetry, while Ta has enormous V_{zz} values in all supercells compared to the Sc, especially at small c/a's. In PZT (50/50), Zr has larger EFGs than Ti atoms, but the Zr EFGs, no larger than 1.0 (10^{22} V/m^2), are still much smaller than Ta EFGs in PST. Ta atoms in [001] ordered Cm PST also have larger η values than Zr atoms in PZT. While V_{zz}(Sc) and η(Sc) approach their $P4mm$ values at the largest $c/a = 1.135$, η(Ta) $= 0.661$ is still much larger than 0. By contrast, the calculations of PZT 50/50 showed that the EFGs of both Zr and Ti in Cm supercell nearly reached their $P4mm$ values at $c/a = 1.055$ (Chapter 3).

The projected eigenvalues for the oxygen atoms are plotted in Fig. 4.14. The two apex oxygen atoms O_1 and O_3 have almost identical EFG components at $c/a < 1.02$. When $c/a > 1.02$, the largest EFG component of O_1, which is closer to Ta than to Sc, changes its direction from parallel to the Cm mirror plane to c direction, as

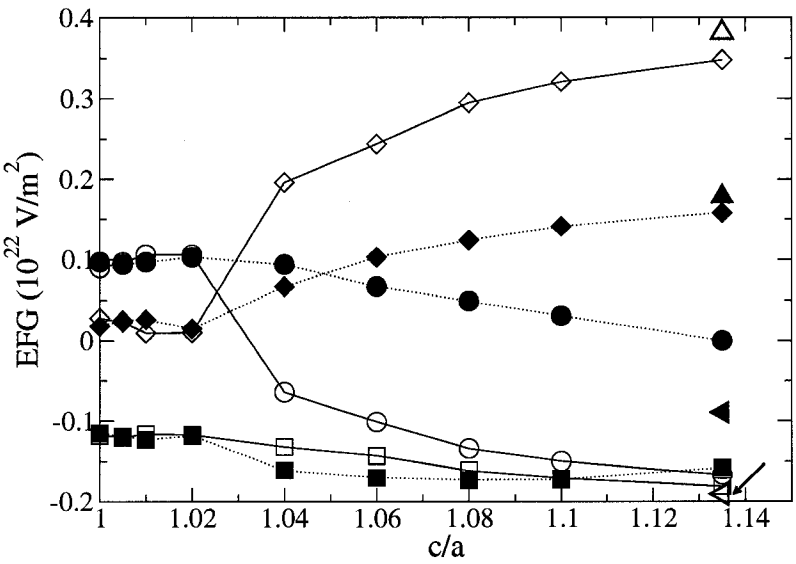

FIG. 4.14: Same as Fig. 4.12, but for the apex-O "projected" EFG eigenvalues (see text). All open symbols are for O_1 (shortest B-O bond with Ta), and filled symbols are for O_3 (shortest B-O bond with Sc).

happened to the apex oxygens in [001] 1:1 ordered *Cm* PZT. However, the other apex oxygen which is closer to Sc does not experience the same direction change of its largest EFG component. The EFG values in Table 4.2 show that $V_{zz}(O_2)$ (O_2 is roughly coplanar with Ta) is larger than the V_{zz}'s of other oxygens in PST for both *Cm* and *P4mm* symmetries. By contrast, all the O atoms in PZT (50/50) have similar V_{zz} values, all of which are smaller than O_2 in PST. Unlike in PZT, O_2 does not have large $\eta \approx 1$, but has instead $\eta < 0.5$ which is similar to that of the apex oxygens.

The effects of the above EFG trends on NMR spectra are examined and shown in section 4.5.

4.3.2 PSW

The numerical EFGs for all metal atoms in the four PSW unit cells are shown in Table 4.3. The metal EFGs in the 15-atom supercell with imposed monoclinic *Pm*

TABLE 4.3: Calculated EFGs (V_{zz}'s in units of 10^{22} V/m^2) for 15-atom PSW supercells with monoclinic Pm and $P1$ symmetries, and 30-atom PSW supercells constructed from $Immm$ and $I4/mmm$ ideal positions. NN is the number of the nearest B neighbors.

	15-Pm			15-$P1$		
Atom	NN(Sc/W)	V_{zz}	η	NN(Sc/W)	V_{zz}	η
Pb_1	5/3	1.359	0.519	5/3	3.614	0.286
Pb_2	6/2	2.449	0.395	6/2	2.447	0.379
Pb_3	5/3	3.606	0.281	5/3	1.383	0.519
Sc_1	3/3	-0.205	0.365	3/3	0.135	0.714
Sc_2	3/3	0.138	0.688	3/3	-0.205	0.376
W_1	6/0	-0.365	0.539	6/0	-0.357	0.481
	30-$Immm$			30-$I4/mmm$		
Atom	NN(Sc/W)	V_{zz}	η	NN(Sc/W)	V_{zz}	η
Pb_1	6/2	3.305	0.090	6/2	-2.366	0.965
Pb_2	5/3	3.133	0.256	6/2	-2.048	0.850
Pb_3	5/3	2.784	0.478	4/4	0.769	0.586
Pb_4	6/2	2.992	0.217	6/2	3.131	0.894
Pb_5	5/3	-1.477	0.868	4/4	1.851	0.261
Pb_6	5/3	1.448	0.248	6/2	1.624	0.929
Sc_1	6/0	-0.244	0.329	6/0	-0.238	0.758
Sc_2	2/4	-0.307	0.372	4/2	-0.805	0.100
Sc_3	2/4	-0.312	0.587	1/5	0.479	0.428
Sc_4	2/4	0.619	0.319	1/5	0.459	0.385
W_1	6/0	0.726	0.724	6/0	-0.725	0.609
W_2	6/0	0.618	0.817	6/0	1.151	0.789

symmetry are very similar to those in the 15-atom PSW unit cell with $P1$ symmetry, while the metal EFGs in the 30-atom $Immm$ supercell are different from those in the 30-atom $I4/mmm$ PSW simulation cell. Both the V_{zz}'s and the η's of these cations are very diverse with different B-cation local orderings. The largest V_{zz}(Pb) value in every structure is greater than those in all PST unit cells (showed in Table 4.3), except in the $I4/mmm$ structure. In $I4/mmm$ PSW, all Pb atoms surrounded by a nearest B neighbor (nBn) shell containing six Sc's and 2 W's (6Sc/2W) have very large asymmetry parameter with η's ≈ 1, while the η's of the Pb atoms in the $Immm$ PSW with the same nBn configuration are much smaller, no larger than 0.217.

The V_{zz}(Sc)'s in the two 15-atom supercells are smaller than all the V_{zz}(Sc)'s in $Immm$ and $I4/mmm$ supercells (Table 4.3). Some correlation between the V_{zz}(Sc)'s and the nBn environment of Sc atoms is observed in the 30-atom PSW unit cells. The Sc atoms with an isotropic Sc nBn cage have the smallest V_{zz} values compared to the Sc's with anisotropic nBn environments. In the $I4/mmm$ unit cell, the Sc with a 6Sc/0W nBn configuration has an $\eta = 0.758$, which is much larger than the η(Sc) = 0.329 of the Sc in $Immm$ PSW with an isotropic Sc nBn shell. The Sc with a Sc-rich nBn surrounding in $I4/mmm$ PSW has the largest $|V_{zz}| = 0.805$ and smallest $\eta = 0.100$ than Sc cations with W-rich nBn's (2Sc/4W and 1Sc/5W).

It is also shown in Table 4.3 that in $I4/mmm$ PSW, the Sc surrounded by a Sc-rich nBn shell (4Sc/2W) has the smallest $\eta = 0.1$ among all Sc's, as well as a V_{zz} twice as large as the Sc cations centered in W-rich nBn shell (1Sc/5W). Note that the six-coordinated ionic radii of Sc^{3+} and W^{5+} are 0.745 Å and 0.60 Å, respectively. The Sc cations in a configuration with W-rich nBn have more "free volume" in the oxygen octahedron, which leads to larger off-centering as well as easier re-orientation of the polarization. This is consistent with the fact that the V_{zz}'s of the Sc atoms with an isotropic Sc nBn shell in $Immm$ and $I4/mmm$ PSW are both about -0.24 (10^{22} V/m^2), which is ~30% larger compared to the V_{zz}= -0.16 (10^{22} V/m^2) for the

Sc in PST with imposed $R3m$ symmetry (note that the Sc in this supercell has an isotropic Ta nBn shell, and the ionic radius of Ta, 0.64 Å, is smaller than that of the Sc). As for the Sc cations in a Sc-rich nBn configuration, there is less space available for distortion, resulting in larger V_{zz}'s. On the other hand, the V_{zz}(Sc)'s in $Immm$ PSW further show their dependence on the off-centering against the O_6 octahedron (Table 4.3). Sc_2, Sc_3, and Sc_4 all have a 2Sc/4W nBn configuration, the off-centering of Sc_4 is 0.25 Å, which differs from the Sc_2 and Sc_3 off-centerings by more than 25%. This difference corresponds to the $|V_{zz}|(Sc_4)$ nearly twice as large as those of Sc_2 and Sc_3. By examining the structure of the nBn octahedral around Sc_2, Sc_3 and Sc_4, we found that in the nBn cage around Sc_2 and Sc_3, two Sc neighbors are both in the equatorial positions, while the two Sc neighbors of Sc_4 are both in the axial positions which allows more distortion.

In all PSW supercells, W atoms are always surrounded by a pure Sc nearest B shell, but they experience very different EFGs. The W's in the 15-atom unit cells both have $V_{zz} \sim 0.36\ 10^{22}\mathrm{V/m^2}$ and $\eta \sim 0.5$, while the ones in the 30-atom simulation cells all have V_{zz}'s larger than $0.6\ 10^{22}\mathrm{V/m^2}$ and η larger than 0.6. In $Immm$ PSW, both the V_{zz}'s and the η's of the two W cations are very similar with each other; and in $I4/mmm$ PSW, the V_{zz}'s of the W atoms are of 50% difference.

4.3.3 PMN

Since many NMR measurements [40, 43, 71, 72] of the Nb spectra in PMN have suggested that the Nb quadrupole coupling parameters are sensitive to the number and identity of its nearest B neighbors as well as its displacement from the ideal cubic position, the following study of PMN is focused on Nb atoms.

The EFGs and the nBn configurations of the Nb cations in the PMN supercell are displayed in Table 4.4. The asymmetry parameter η as well as the V_{zz} of the Nb's

TABLE 4.4: Calculated EFGs for Nb cations and the surrounding nBn configurations in the PMN simulation cell. NN is the number of the nearest B neighbors.

Atom	V_{zz} (10^{22} V/m^2)	η	NN(Mg/Nb)
Nb_1	0.483	0.458	1/5
Nb_2	0.421	0.561	1/5
Nb_3	-1.089	0.872	3/3
Nb_4	-1.091	0.847	3/3
Nb_5	-0.825	0.742	3/3
Nb_6	-0.814	0.527	3/3
Nb_7	-0.861	0.132	5/1
Nb_8	-0.790	0.181	5/1

are very sensitive to the nBn environment. In the PMN simulation cell, there are three types of nBn environments around the Nb cations, 1Mg/5Nb, 3Mg/3Nb, and 5Mg/1Nb. The Nb's centered in an nBn cage with 1:1 Nb/Mg (3Mg/3Nb nBn) all have η's larger than 0.5. The two Nb's with a Mg-rich nBn octahedron (5Mg/1Nb) have small η's both less than 0.2, while the η's of those Nb's surrounded by a Nb-rich nBn shell (1Mg/5Nb) are both around 0.5. The Nb's with a 1Mg/5Nb nBn configuration also have the smallest V_{zz} around 0.45, which is about 50% smaller than the V_{zz}'s of the Nb cations surrounded by more Mg atoms. Such effects of the nBn configuration on the centered B cation EFGs were also observed in the previous PSW calculations (shown in section 4.3.2).

4.4 Structural sensitivity of calculated EFGs

It has been shown that the off-centering of Ti atom in PZT correlates with strain and the polarization rotation. In this section, the effects of local structures on B-atom EFGs in PST, PSW and PMN are discussed. Previous PZT calculations (in Chapter 3) also showed strong sensitivity of the O EFGs to the local structure. Oxygen EFGs are strongly affected by the off-centering of Pb atoms, which correlates

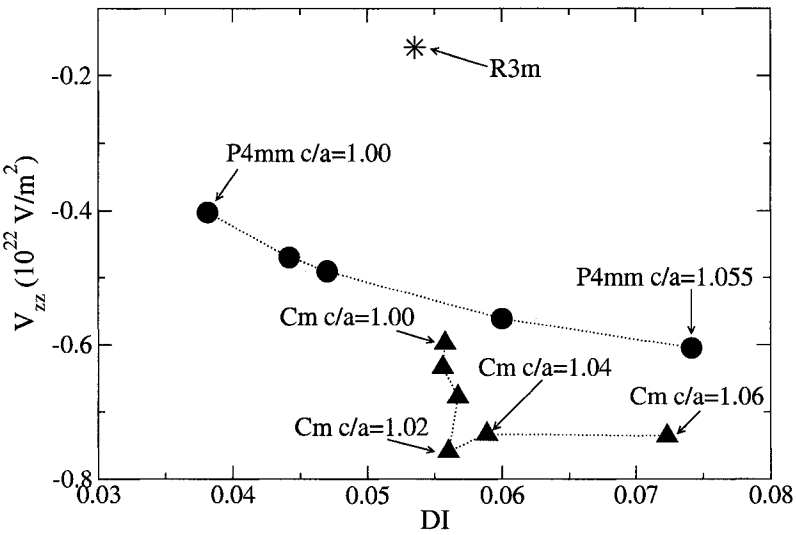

FIG. 4.15: Shear strain (distortion index DI, see Eq. (3.3)) dependence of the calculated PST V_{zz}(Sc) for different imposed symmetries: tetragonal $P4mm$ (circles), monoclinic Cm (triangles), and rhombohedral $R3m$ (star).

with the polarization. Hence, in this section, Pb off-centerings in Cm PST and their effects on surrounding O EFGs are examined.

4.4.1 EFGs and off-centerings of B atoms

One measure of the B-atom off-centering, the distortion index (DI) (Eq. (3.3)), showed very strong correlation with the polarization rotation in Cm PZT 50/50. Figs. 4.15 and 4.16 show the dependence of V_{zz} on DI for Sc and Ta in PST with imposed Cm, $P4mm$, and $R3m$ symmetries. In $P4mm$ PST, both Sc and Ta show nearly linear variations, but Ta has much larger slope than Sc. In Cm PST, for $c/a \leq 1.02$, DI(Sc) shows little variation as V_{zz}(Sc) changes by about 25%. For $c/a \geq 1.04$, DI(Sc) shows about a 25% variation as V_{zz}(Sc) remains nearly constant. By contrast with the linear variation of DI in $P4mm$ PST, both DI(Sc) and DI(Ta) show an abrupt change in slope near c/a = 1.02. Another measure of the B-atom off-centering is the longitudinal strain $|\alpha|$, defined in Eq. (3.2). The longitudinal

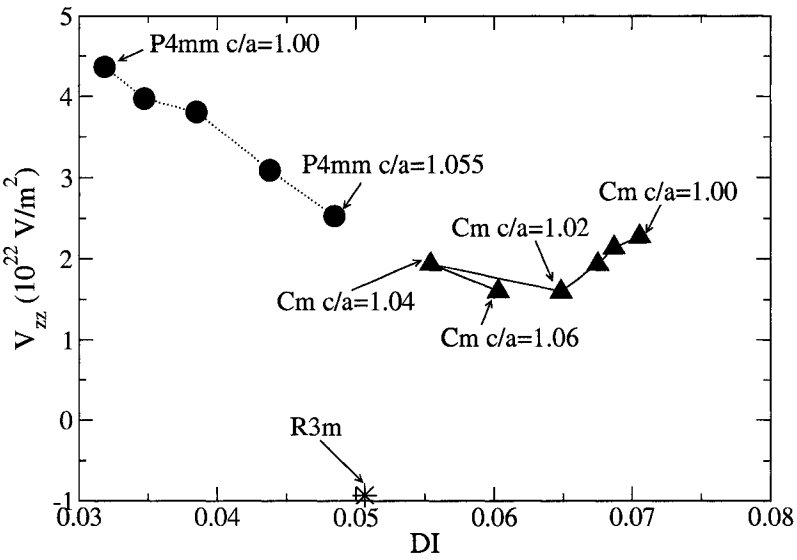

FIG. 4.16: Shear strain (distortion index DI, see Eq. (3.3)) dependence of the calculated PST V_{zz}(Ta) for different imposed symmetries. Same legends as in Fig. 4.15.

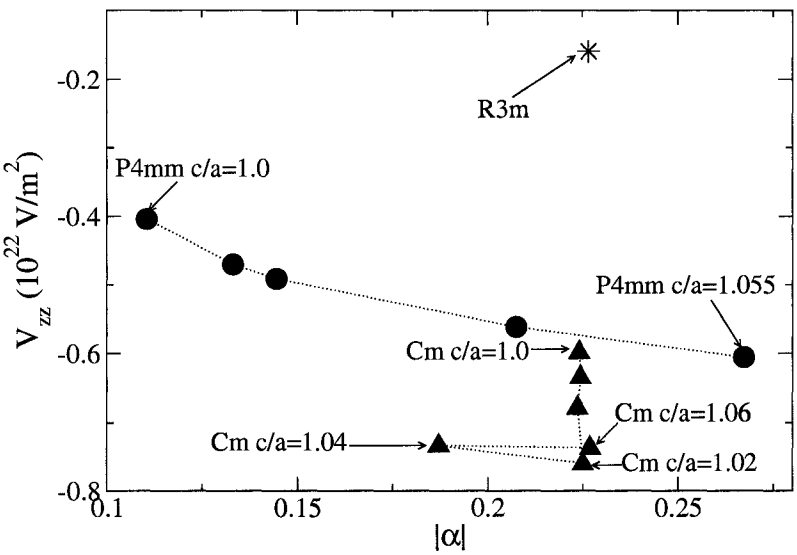

FIG. 4.17: Longitudinal strain $|\alpha|$ (see Eq. (3.2)) dependence of the calculated PST V_{zz}(Sc) for different imposed symmetries. Same legends as in Fig. 4.15.

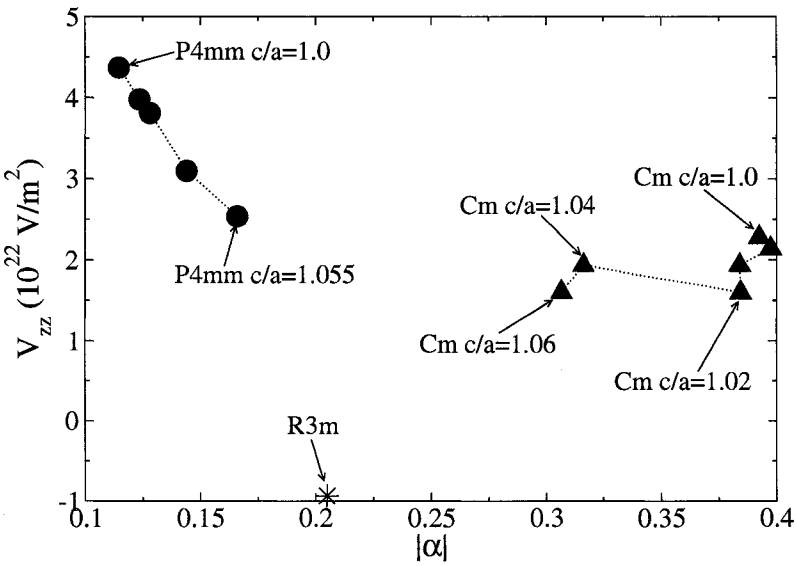

FIG. 4.18: Longitudinal strain $|\alpha|$ (see Eq. (3.2)) dependence of the calculated PST V_{zz}(Ta) for different imposed symmetries. Same legends as in Fig. 4.15.

strain $|\alpha|$ of both Sc and Ta also show this abrupt break in slope in Cm PST, as displayed in Figs. 4.17 and 4.18. This is in contrast to Cm PZT 50/50, where $|\alpha|$(Ti) varied linearly as shown in Fig. 3.16.

NMR experiments have been carried out to measure the ^{45}Sc spectra in PSW [41], and ^{93}Nb spectra in PMN [40, 44, 45] in order to study the local structures in these solid solutions. Unfortunately, it is very difficult to identify various chemical B sites with different nBn structures because their spectra often overlap with one another and form a broad peak. Hence, it is of great importance to examine the nBn influence on the centered Sc and Nb EFGs in PSW and PMN.

The dependence of V_{zz} on DI and $|\alpha|$ for Sc in PSW and Nb in PMN simulation cells are shown in Fig. 4.19 – Fig. 4.22. $|\alpha|$(Nb)'s separate to form three groups according to the three types of the Nb nBn configurations in Fig. 4.21. The longitudinal strain of the Nb cations with a Mg-rich nBn shell (5Mg/1Nb) are more than 25% smaller than those of the Nb's with less Mg's in the nBn cage. Since Mg^{2+} has an ionic radius of 0.72 Å, larger than $R_{\text{ionic}}(Nb^{5+}) = 0.64$ Å, Mg-rich nBn

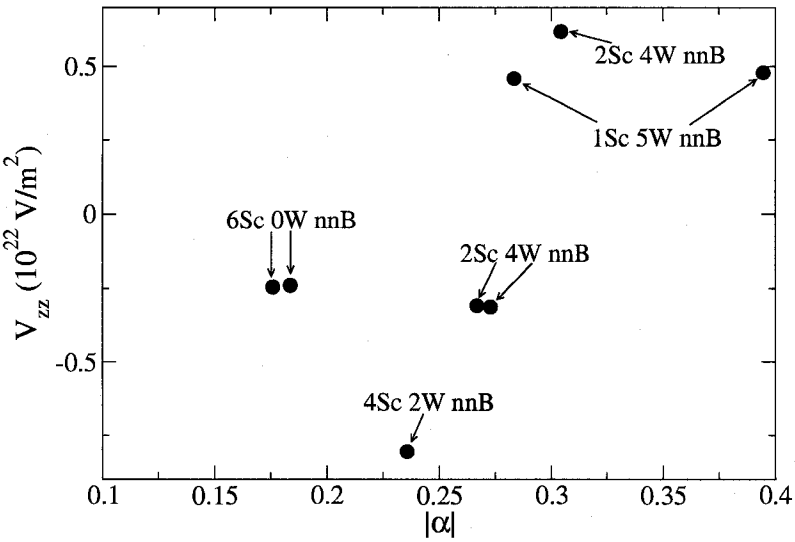

FIG. 4.19: Longitudinal strain $|\alpha|$ (see Eq. (3.2)) dependence of the calculated PSW V_{zz}(Sc). Black circles are for Sc atoms in $Immm$ PSW supercell, and red circles are for Sc atoms in $I4/mmm$ supercell.

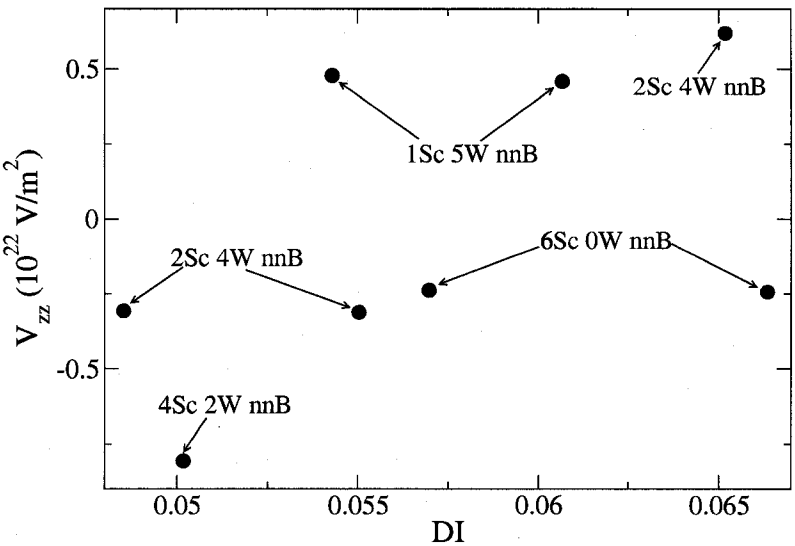

FIG. 4.20: Shear strain (distortion index DI, see Eq. (3.3)) dependence of the calculated PSW V_{zz}(Sc) for $Immm$ and $I4/mmm$ supercells. Symbols are the same as in Fig. 4.19.

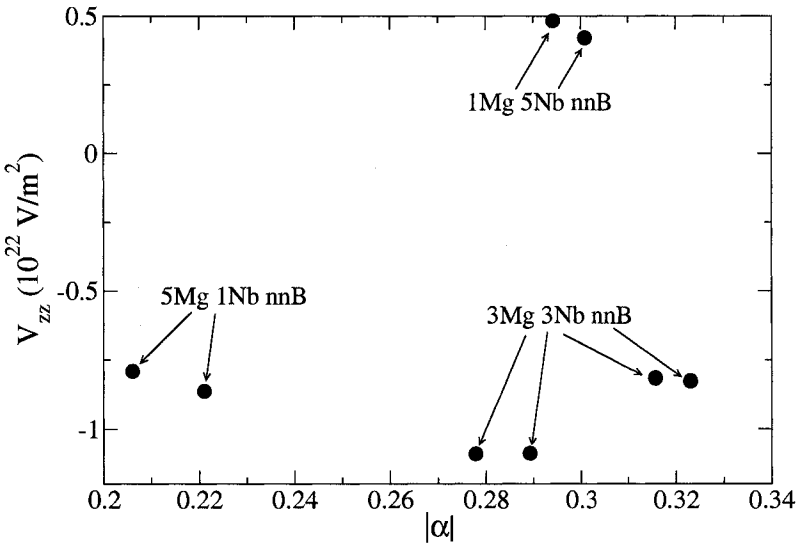

FIG. 4.21: Longitudinal strain $|\alpha|$ (see Eq. (3.2)) dependence of the calculated PMN V_{zz}(Nb).

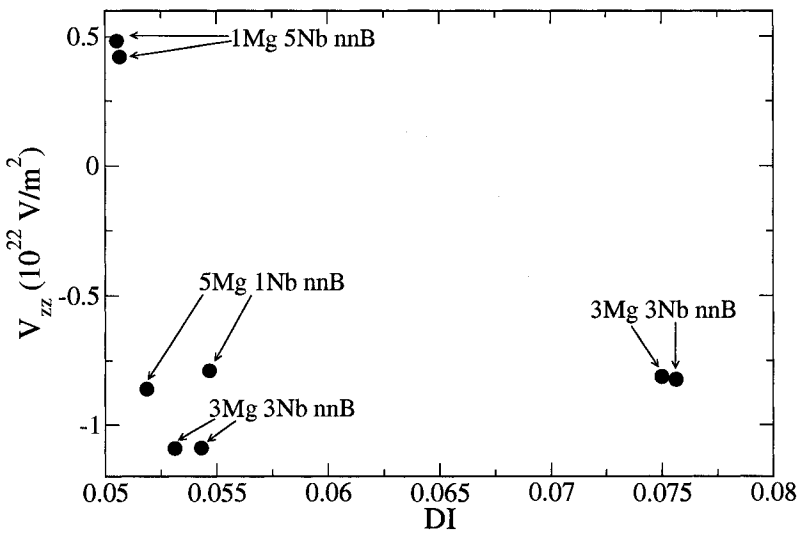

FIG. 4.22: Shear strain (distortion index DI, see Eq. (3.3)) dependence of the calculated PMN V_{zz}(Nb).

configurations yield less free space in the O_6 cage for the surrounded Nb to displace from the high symmetry cubic position. The Nb's with 3 Mg's or 1 Mg in the nBn configuration experience α's within 15% difference, but their $|V_{zz}|$'s are separated by about 200%. However, DI(Nb)'s showed less correlation with the nBn environments (Fig. 4.22). DI's of the two Nb's with 5Mg/1Nb nBn cage as well as two Nb's with 3Mg/3Nb nBn cage are all between 0.052 and 0.055, while DI's of the other two Nb's with 3Mg/3Nb nBn shell are larger than 0.075.

By contrast with the strong correlation between α(Nb) and surrounding nBn configuration in 60-atom PMN simulation cell, both $|\alpha|$(Sc) and DI(Sc) in 30-atom PSW supercells show little sensitivity to the nBn configuration (Figs. 4.19 and 4.20). The two Sc's centered in an isotropic Sc nBn cage have similar longitudinal strain around 0.2, and two out of three Sc's with 2Sc/4W nBn configuration have $|\alpha| \sim$ 0.27. The lack of sensitivity of the Sc off-centerings to the local structure may be caused by the limitations of the present 30-atom PSW simulation cells, which are half the size of the PMN supercell, in modeling the disordered structure of PSW. However, the good agreement of the calculated pair distribution functions (PDFs) with the experimental PDFs in Fig. 4.8 indicates that the nearest neighbor atomic structure is reasonably well reproduced.

4.4.2 Pb off-centering and O EFGs in PST

The Pb off-centerings with respect to the surrounding oxygen cage are examined in this section to understand the EFG changes of Pb and O atoms shown in Figs. 4.10 and 4.11. Note in these figures, V_{zz}'s of Pb_1 and Pb_2 in monoclinic Cm PST are almost identical at $c/a \leq 1.02$. At $c/a \geq 1.04$, $V_{zz}(Pb_1)$'s increased as $V_{zz}(Pb_2)$'s decreased. The difference between η values of the two Pb atoms also largely increased at $c/a \geq 1.04$. In $P4mm$ symmetry, the $V_{zz}(Pb_1)$'s are more than 3 times larger

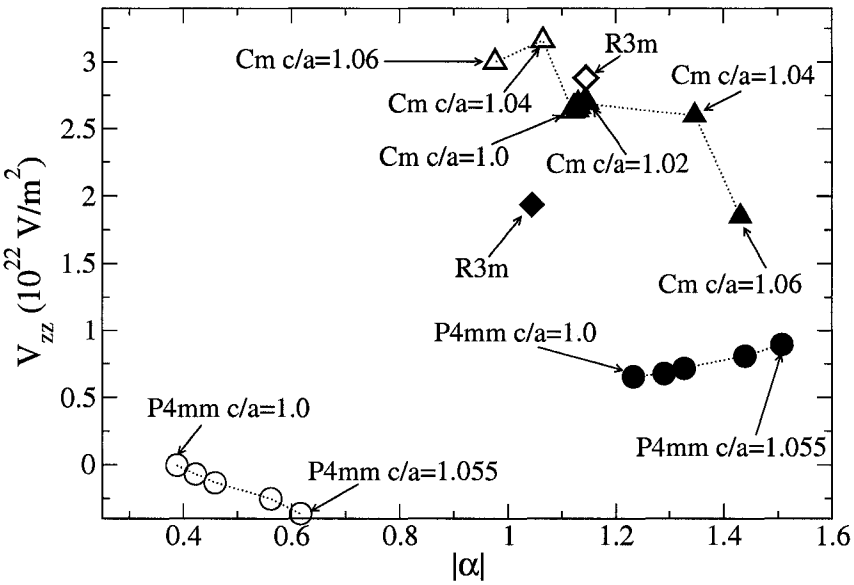

FIG. 4.23: Longitudinal strain $|\alpha|$ (see Eq. (3.2)) dependence of the calculated PST V_{zz}(Sc) for different imposed symmetries: tetragonal $P4mm$ (circles), monoclinic Cm (triangles), and rhombohedral $R3m$ (diamonds). All open symbols are for Pb_1, and filled symbols are for Pb_2.

than $V_{zz}(Pb_2)$'s. The large difference of Pb_1 and Pb_2 EFGs in PST with both Cm and $P4mm$ symmetries were not observed in PZT 50/50. The V_{zz}'s and the η's of the oxygens in PST showed similar changes of behavior at c/a's above 1.02 as Pb atoms. To facilitate comparison of heterovalent PST 50/50 with homovalent PZT 50/50, Pb off-centerings in PST in the range $0 \leq c/a \leq 1.06$ are focused on, since the structures of PZT and PST are similar in $P4mm$ and Cm symmetries.

One measure of the Pb off-centering is the longitudinal strain $|\alpha|$. Fig. 4.23 shows the calculated PST Pb V_{zz} as a function of $|\alpha|$ in imposed monoclinic Cm, tetragonal $P4mm$, and rhombohedral $R3m$ symmetries. In Cm PST with $c/a \leq 1.02$, Pb_1 and Pb_2 have the same value of $|\alpha|$'s, as well as V_{zz}'s. At larger c/a, Pb_1 has smaller longitudinal strains and larger V_{zz}'s compared to Pb_2. This is consistent with the Pb EFG changes shown in Figs. 4.10 and 4.11. At the largest c/a values, the Pb_1 V_{zz} in Cm symmetry is 8 times as large as the V_{zz} in $P4mm$ symmetry,

while $|\alpha|(Pb_1)$ in monoclinic PST is 30% larger than that in tetragonal PST. On the other hand, the V_{zz} and $|\alpha|$ of Pb_2 differ by only 100% and 5% in Cm and $P4mm$ symmetries, respectively. V_{zz}'s in $P4mm$ symmetry show a nearly linear variation for both Pb's, but the slopes are of opposite sign. And all $|\alpha|$'s and V_{zz}'s of Pb_2 are more than 2 times larger than those of Pb_1 in $P4mm$ PST. In $R3m$ symmetry, the two Pb atoms are less different than in $P4mm$ symmetry, the V_{zz}'s and $|\alpha|$'s of the Pb's differ by 40% and 10% separately from each other.

Another measure of Pb off-centering, $\vec{\delta}$, is the displacement of the Pb from its surrounding O-cage center of mass. Numerical results are listed in Table 4.5. In Cm symmetry, there is little difference in $\vec{\delta}(Pb_1)$ and $\vec{\delta}(Pb_2)$ at c/a less than 1.04. For $c/a \geq 1.04$, Pb $\vec{\delta}$'s differ by about 30%. The corresponding $|\alpha|$'s also differ by about 30% in Fig. 4.23. More importantly, unlike in Cm PZT, $\vec{\delta}$(Pb)'s in Cm PST are not orientated and rotated along the same directions as c/a changes. For $c/a \leq 1.02$, Pb_1 lies in the $\langle 110 \rangle$ mirror plane pointing close to the [111] direction, while Pb_2 lies in the same plane pointing close to another body diagonal direction $[11\bar{1}]$. As c/a increases, $\vec{\delta}(Pb_1)$ rotates in the Cm plane away from the c direction and toward the $[11\bar{1}]$ direction, while $\vec{\delta}(Pb_2)$ rotates toward $[00\bar{1}]$ c direction. The difference between the Pb rotation directions in Cm symmetry is consistent with the different behaviors of Pb EFG components seen in Fig. 4.12: 1)the Pb_1 EFG component parallel to the Cm plane, $V_{\parallel}(Pb_1)$, remains the largest in magnitude compared to the other two components as c/a changes, 2)both of the Pb_2 EFG components parallel to the Cm mirror and along c direction change sign at $c/a \geq 1.04$, and all EFG components are close to their $P4mm$ values at the largest $c/a = 1.055$. However, in Cm PZT 50/50 , all EFG components of both Pb's persist their signs. The differences in V_{zz}(Pb) and η(Pb) between the two Pb's in Cm PZT are much smaller than in Cm PST at large $c/a = 1.055$. In $P4mm$ PST, both Pb atoms can only move along the c axis, but $\vec{\delta}(Pb_2)$ is more than 3 times as large $\vec{\delta}(Pb_1)$ for all c/a's. As in $P4mm$ PZT

TABLE 4.5: Pb off-centerings in monoclinic Cm, tetragonal $P4mm$ and rhombohedral $R3m$ PST along x, y, z directions as well as the total magnitude all in the unit of Å.

		Pb_1				Pb_2			
	c/a	δ_x	δ_y	δ_z	$\lvert\delta_{off}\rvert$	δ_x	δ_y	δ_z	$\lvert\delta_{off}\rvert$
Cm	1.0	0.340	0.340	0.250	0.542	0.339	0.339	-0.258	0.544
	1.005	0.338	0.338	0.264	0.545	0.340	0.340	-0.252	0.543
	1.01	0.345	0.345	0.258	0.551	0.343	0.343	-0.257	0.549
	1.02	0.338	0.338	0.258	0.543	0.341	0.341	-0.268	0.551
	1.04	0.333	0.333	-0.079	0.478	0.156	0.156	-0.591	0.631
	1.06	0.305	0.305	-0.160	0.460	0.090	0.090	-0.670	0.682
$P4mm$	1.0	0	0	-0.138	0.138	0	0	-0.600	0.600
	1.0105	0	0	-0.151	0.151	0	0	-0.624	0.624
	1.015	0	0	-0.168	0.168	0	0	-0.640	0.640
	1.035	0	0	-0.215	0.215	0	0	-0.689	0.689
	1.055	0	0	-0.234	0.234	0	0	-0.718	0.718
$R3m$	1.0	0.318	0.318	0.318	0.550	0.300	0.300	0.300	0.519

50/50, $\vec{\delta}$(Pb) of the two Pb atoms differ by no more than 50%. Given that PZT 50/50 has isovalent B-site cations, Zr^{4+} and Ti^{4+}, while PST has heterovalent B-site cations, Sc^{3+} and Ta^{+5}, the hetero-charged B-site in [001]1:1 ordered PST gives rise to largely different Pb displacements as well as their EFGs.

As mentioned, the large Pb off-centerings about 0.5 Å in Cm, $P4mm$ and $R3m$ PST (Table 4.5) are also seen in the PDFs (Fig. 4.6). In the ideal perovskite structure, the 12 Pb-O bonds are all of the same length. As a result of the strong Pb off-centering in PST with imposed Cm symmetry, the nearest Pb-O distance is greatly reduced to 2.3 Å as shown in Table 4.1. In [001]1:1 ordered Cm PZT 50/50, the simulated static quadrupole NMR spectra of the axial oxygens, O_1 and O_3, showed great sensitivity to the electric polarization direction. As will be shown in the next section, in Cm PST, not only the quadrupole NMR spectra of the axial oxygens O_1 and O_3, but those of the equatorial oxygens O_2 and O_4 all show similar sensitivity to local structures. The width, the splitting and the lineshape of the

TABLE 4.6: Pb off-centerings in [001]1:1 ordered monoclinic Cm, tetragonal $P4mm$ and [111]1:1 ordered rhombohedral $R3m$ PZT 50/50 along x, y, z directions as well as the total magnitude all in the unit of Å.

		Pb_1				Pb_2			
	c/a	δ_x	δ_y	δ_z	$\lvert\delta_{off}\rvert$	δ_x	δ_y	δ_z	$\lvert\delta_{off}\rvert$
Cm	1.0	-0.294	-0.294	0.257	0.489	-0.289	-0.289	0.411	0.579
	1.01	-0.273	-0.273	0.290	0.483	-0.266	-0.266	0.456	0.591
	1.02	-0.241	-0.241	0.328	0.473	-0.237	-0.237	0.502	0.603
	1.03	-0.199	-0.199	0.368	0.463	-0.198	-0.198	0.549	0.616
	1.035	-0.167	-0.167	0.389	0.455	-0.172	-0.172	0.572	0.621
	1.04	-0.134	-0.134	0.411	0.453	-0.145	-0.145	0.599	0.633
	1.045	-0.117	-0.117	0.424	0.455	-0.131	-0.131	0.611	0.638
	1.05	-0.104	-0.104	0.439	0.463	-0.109	-0.109	0.623	0.642
	1.055	-0.082	-0.082	0.447	0.462	-0.085	-0.085	0.641	0.652
$P4mm$	1.0	0	0	0.401	0.401	0	0	0.589	0.589
	1.01	0	0	0.408	0.408	0	0	0.589	0.589
	1.02	0	0	0.427	0.427	0	0	0.616	0.616
	1.03	0	0	0.434	0.434	0	0	0.623	0.623
	1.035	0	0	0.440	0.440	0	0	0.629	0.629
	1.04	0	0	0.442	0.442	0	0	0.632	0.632
	1.045	0	0	0.452	0.452	0	0	0.643	0.643
	1.05	0	0	0.456	0.456	0	0	0.652	0.652
	1.055	0	0	0.459	0.459	0	0	0.658	0.658
$R3m$	1.0	-0.284	-0.284	-0.284	0.491	-0.305	-0.305	-0.305	0.528

oxygen spectra showed large difference at $c/a \leq 1.02$ and $c/a \geq 1.04$, as can be seen in Fig. 4.26 – Fig. 4.29. Also shown in Table 4.2, at the largest $c/a = 1.135$, the EFGs of all oxygens are close to their $P4mm$ values at the same c/a, except for the axial O_3. Note that O_2 and O_4 are in the PbO_{12} cage of both Pb_1 and Pb_2, but O_1 and O_3 are only in the PbO_{12} cage of Pb_2 and Pb_1, respectively. Given that $\vec{\delta}(Pb_1)$ is along body-diagonal direction instead of the c direction at large c/a beyond 1.04, the local environment around O_3 is not close to its $P4mm$ structure.

4.5 Simulated NMR spectra

NMR experiment [39] and previous calculations in PZT 50/50 showed that oxygen NMR spectra are very sensitive to the local structure. EFGs of B-atoms and O atoms in PST also vary as strain and imposed symmetry changes. In PSW and PMN, the sensitivity of Sc (in PSW) and Nb (in PMN) EFGs to the number and identity of their nBn environment as well as to distortions from exact cubic symmetry seen in previous discussion have also been deduced from NMR measurements [40, 43, 71, 72]. Hence, the first part of this section will present the simulated EFG NMR spectra in PST, PSW and PMN. In the second part of this section, comparisons between the simulated B-atom EFG spectra and NMR measurements in PST, PSW and PMN will be presented and discussed.

4.5.1 Manifestation of EFGs on measured NMR spectra

From the calculated PST EFGs, static NMR powder patterns were generated and shown in Fig. 4.24 – Fig. 4.29 for monoclinic Cm PST as a function of c/a for all atoms except Pb, which has no quadrupolar interaction. The spectrum of tetragonal $P4mm$ PST (for $c/a = 1.055$) is also shown in the figures for comparison. The spectra are powder patterns of the central ($m = 1/2 \leftrightarrow -1/2$) $\nu^{(2)}_{1/2}$ transition,

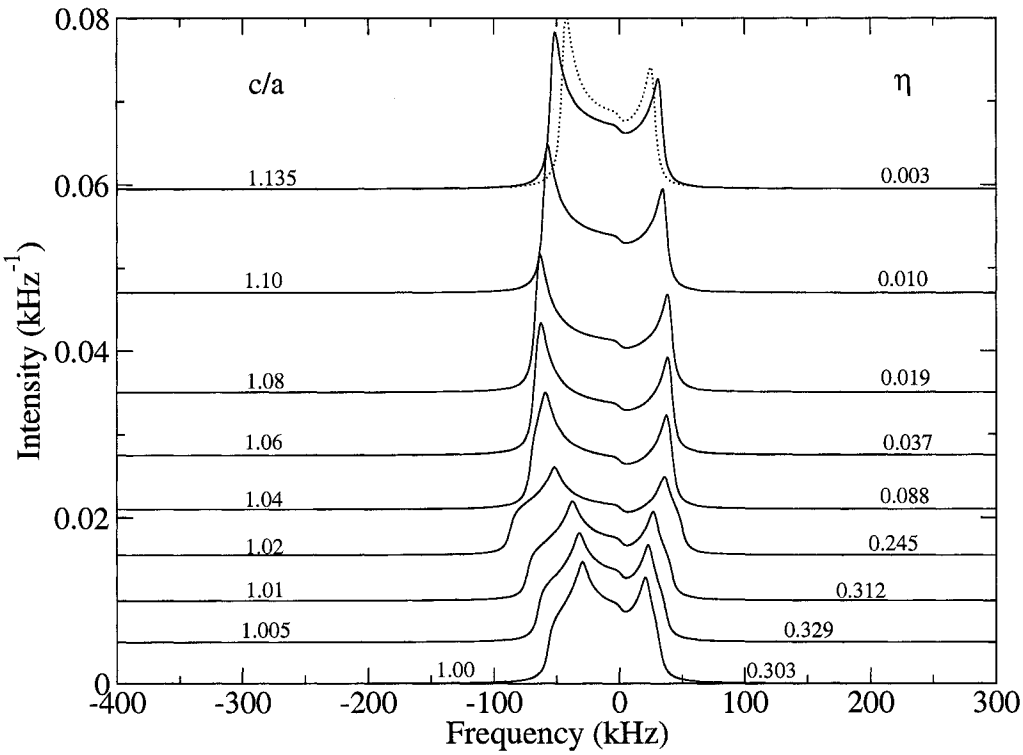

FIG. 4.24: ^{45}Sc static NMR powder spectrum in monoclinic Cm PST. For comparison, the dotted curve shows the spectrum in tetragonal $P4mm$ PST with c/a=1.135. Numbers labeling the curves show the corresponding c/a and η values, as indicated.

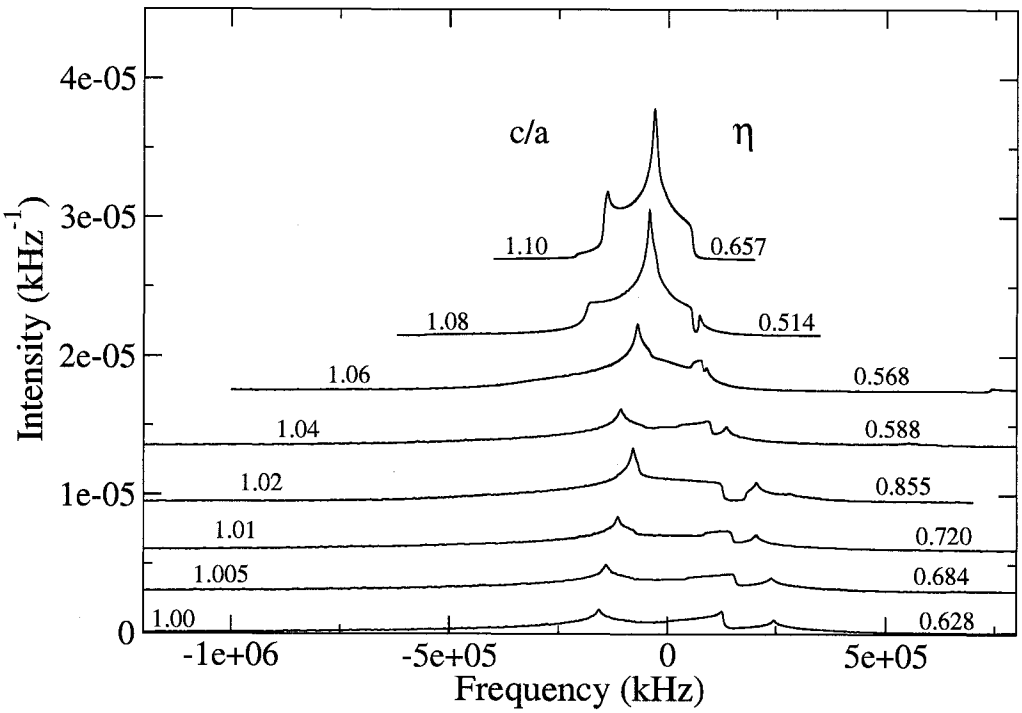

FIG. 4.25: ^{181}Ta static NMR powder spectrum in monoclinic Cm PST. The spectrum in tetragonal $P4mm$ PST with c/a=1.135, which is much narrower than the Cm spectra, is not shown here.

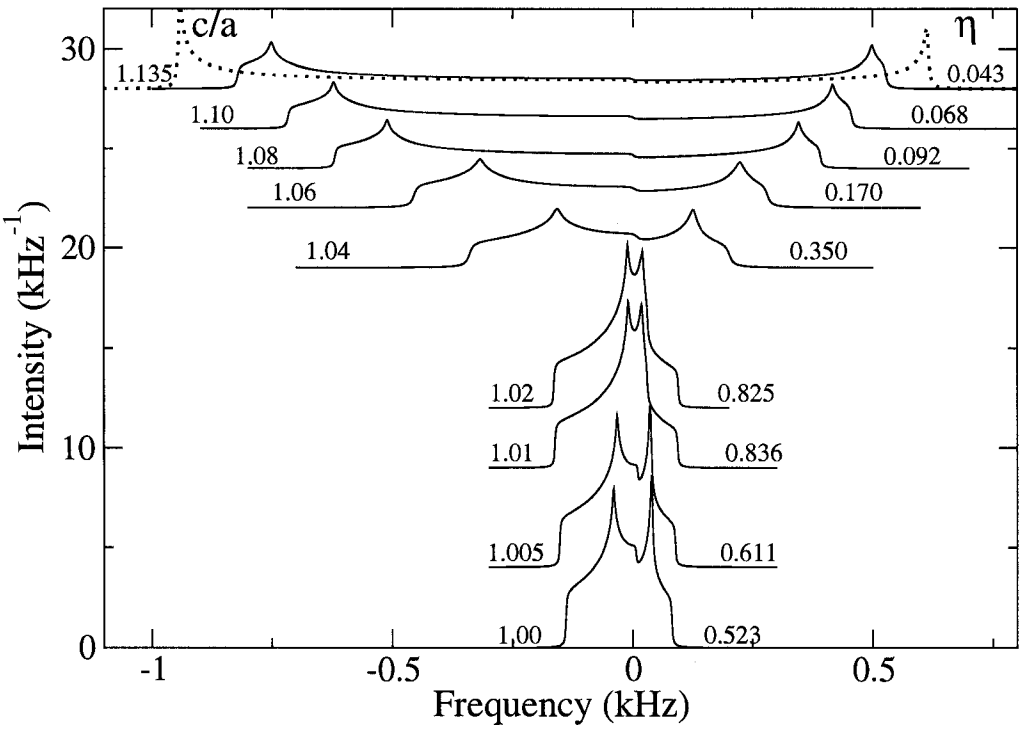

FIG. 4.26: ^{17}O static NMR powder spectrum for the apex O_1 atom (apex O nearest to Ta) in monoclinic *Cm* PST. Note the change in the frequency scale. Dotted curve as in Fig. 4.24.

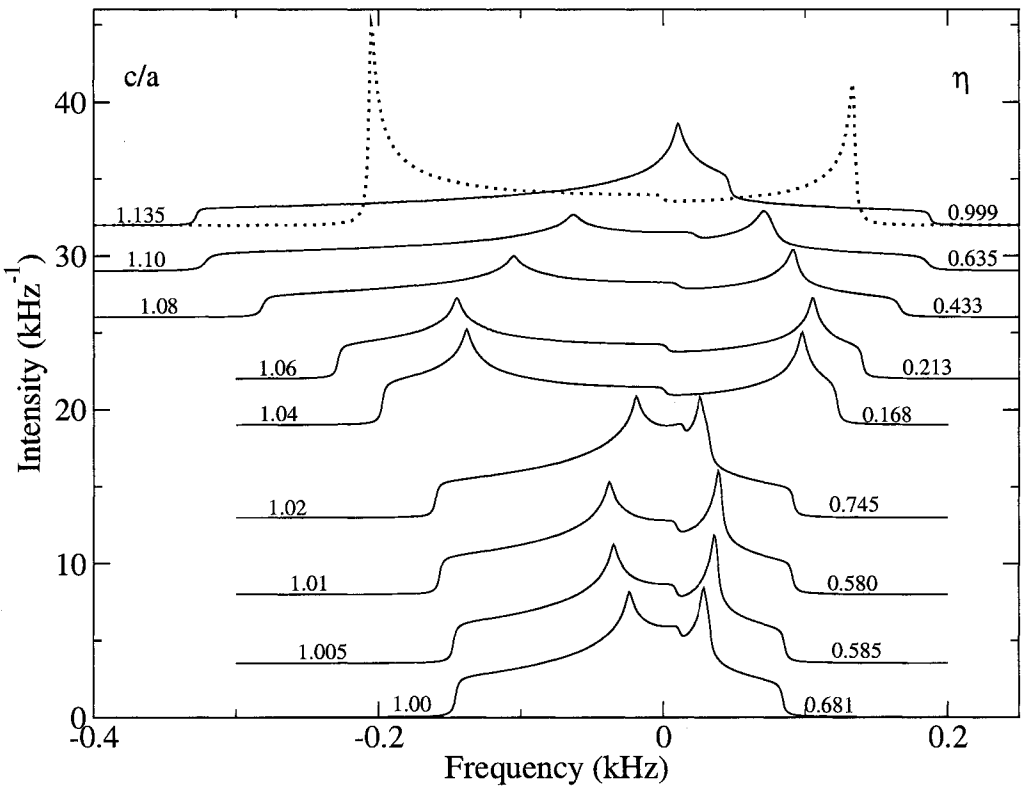

FIG. 4.27: ^{17}O static NMR powder spectrum for the apex O_3 atom (apex O nearest to Sc) in monoclinic *Cm* PST. Dotted curve as in Fig. 4.24.

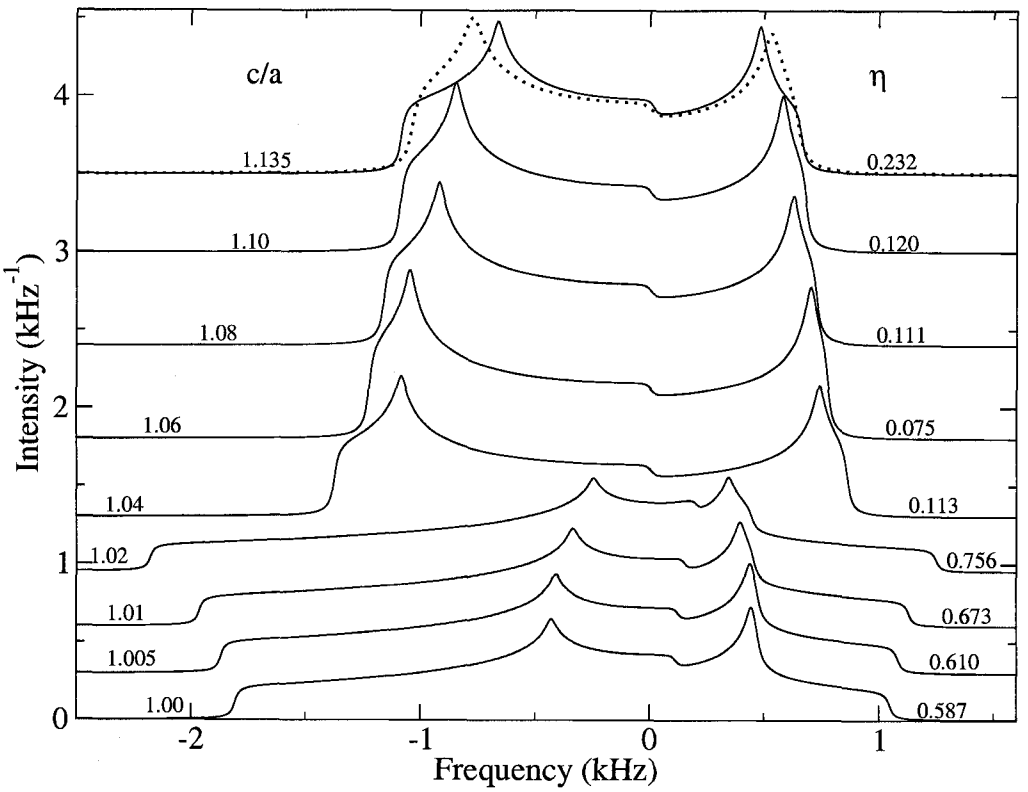

FIG. 4.28: ^{17}O static NMR powder spectrum for the O_2 atom (equatorial O approximately in the Sc plane) in monoclinic Cm PST. Dotted curve as in Fig. 4.24.

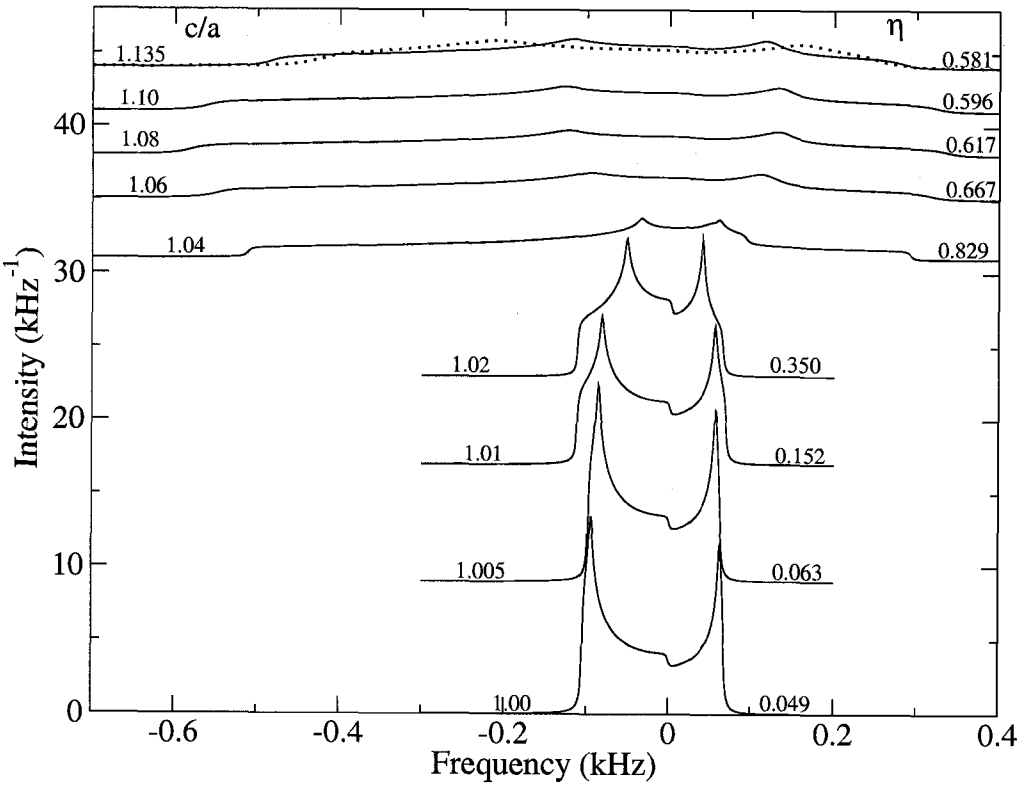

FIG. 4.29: ^{17}O static NMR powder spectrum for the O_4 atom (equatorial O approximately in the Ta plane) in monoclinic Cm PST. Dotted curve as in Fig. 4.24.

as described in Appendix A. In simulating these spectra, the values used for the quadrupole moments Q were -22.0, 317.0, and -2.558 fm^2 for ^{45}Sc, ^{181}Ta, and ^{17}O, respectively [146]. Both Sc and Ta isotopes have spin $I = 7/2$, and ^{17}O has spin $I = 5/2$. The powder patterns were calculated for an applied (high) field of B = 17.6 T, which corresponds to Larmor frequencies of 182.205, 89.775, and 101.676 MHz for ^{45}Sc, ^{181}Ta, and ^{17}O, respectively. The simulated spectra of Sc and Ta in Cm PST show the smallest change in both the width and the splitting compared to the oxygen atoms. All the O simulation spectra experience abrupt change of splitting or/and width at $c/a = 1.02$, where Pb_1 and Pb_2 start to have different B environments. These changes in the O spectra are consistent with the abrupt break of slope of DI(Sc,Ta) and $|\alpha|$(Sc,Ta) seen in Fig. 4.15 – Fig. 4.18. The O spectra in Cm PST are all approaching their $P4mm$ results at the largest $c/a = 1.135$ except for axial O_3 which locates almost in the same $\langle 001 \rangle$ plane as Pb_1. Since Pb_1 is far from its $P4mm$ position at $c/a = 1.135$, the coplanar O_3 can not achieve its $P4mm$ environment, as shown in Fig. 4.10 and Table 4.2. The width of the simulated O_3 spectrum increases more smoothly than the other oxygen spectra, and the splitting at $c/a = 1.135$ is very different from its $P4mm$ spectrum. The apex O EFG spectra are thus seen to be a very sensitive probe of structural changes associated with the Pb displacements in PST. It is also seen that the simulated NMR spectra of O_2 and O_4, coplanar with Sc and Ta respectively, have very different behavior. O_4 spectrum experiences an abrupt increase of the line width at c/a=1.02 while the splitting has little change. The line width of O_2 decreases as c/a above 1.02, and the splitting sharply increases. This opposite change of trends in the equatorial oxygen spectra linewidth was also seen in our previous calculations for PZT 50/50 which has a heterovalent B site, and the changes in PZT O spectra were monotonic with no reflection of the polarization rotation. Also note that the line width of O_2 is more than twice as large as that of O_4, while the width difference of two equatorial O

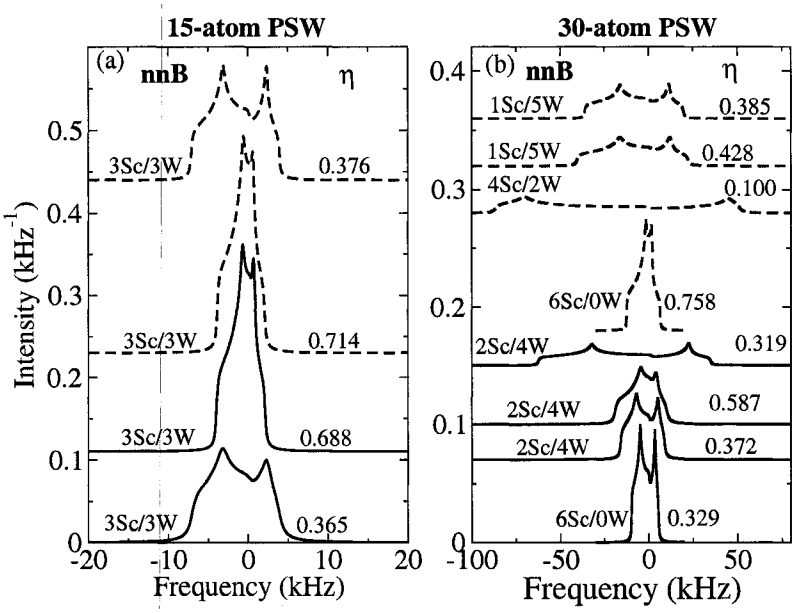

FIG. 4.30: Panel (a) and (b) show ^{45}Sc static powder spectrum in 15-atom and 30-atom PSW supercells separately. In panel (a), the solid curves are for monoclinic Pm PSW, and the dashed ones for $P1$ PSW. In panel (b), the curves with solid line are for $Immm$ PSW, and the ones with dashed line are for $I4/mmm$ PSW. Note the change of the frequency scale between the two panels.

spectra in PZT are very small. The sensitivity of the equatorial O EFG spectra can thus help to identify the B ordering related structure changes.

In the NMR measured spectrum of ^{45}Sc in PSW [41], a narrow peak and a broad peak were observed, where the narrow peak was assigned to the Sc site with a pure Sc nBn shell and the broad peak include the contributions from all other Sc sites surrounded by both Sc and W cations. Two Gaussians were used to simulate the broad peak in experiment, but no specific nBn configurations were assigned to the Gaussians. To help interpret the measured Sc NMR spectra, simulated static ^{45}Sc (I = 7/2) quadrupolar NMR spectra were generated from the calculated V_{zz}(Sc)'s and η(Sc)'s, shown in Fig. 4.30. The quadrupole moment Q and the Larmor frequency used in these simulations are the same as those used to generate PST ^{45}Sc spectra. The Sc spectra show some sensitivity to the nBn environment. In $Immm$ PSW, the Sc with an isotropic Sc nBn has the narrowest line width compared with

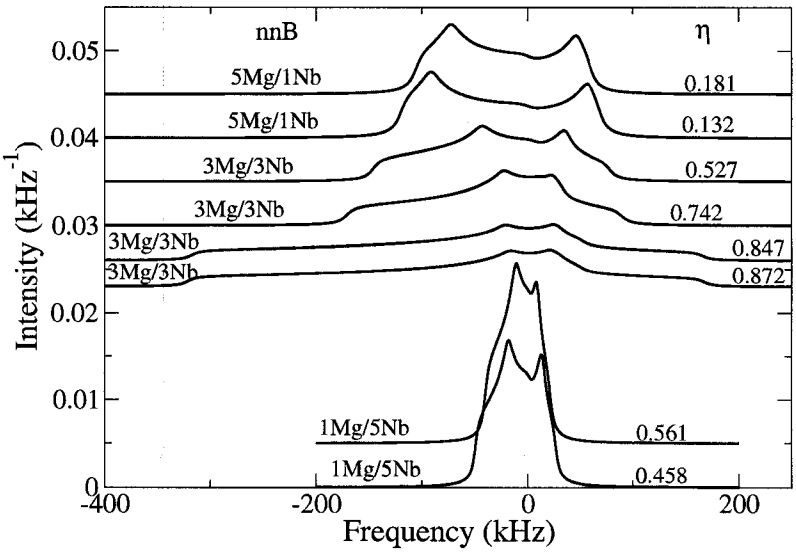

FIG. 4.31: ^{93}Nb static powder spectrum in the PMN supercell.

spectra of the other three Sc atoms surrounded by a 2Sc/4W nBn. In $I4/mmm$ PSW, the Sc centered at a pure Sc_6 shell has not only the narrowest spectrum line width, but also the smallest splitting. The Sc with a Sc-rich 4Sc/2W nBn cage has the broadest spectrum line width as well as the largest splitting.

In the PMN supercell, the difference in the Nb EFGs can result in different lineshapes as well as broadenings of the EFG-induced NMR quadrupole static spectra. Using the calculated EFGs, static NMR powder patterns for isotope ^{93}Nb with spin $I = 9/2$ are shown in Fig. 4.31. In simulating the ^{93}Nb spectra, the quadrupole moment Q = -32.0 fm^2 [146] was used. The powder patterns were calculated for an applied (high) field of B = 17.6 T, which corresponds to a Larmor frequency of 183.321 MHz for ^{93}Nb.

As seen in Fig. 4.31, the calculated ^{93}Nb spectra show large sensitivity to the nBn configuration. The spectra of the Nb's with a 1Mg/5Nb nBn configuration have the narrowest line width, and the Nb's with a 5Mg/1Nb nBn cage have the largest splitting between the peaks.

TABLE 4.7: Nb quadrupole coupling constant C_Q from the LAPW calculation and from NMR measurement [45] for broad lineshapes D1 and D2 in units of MHz. The calculated C_Q for D1 is an average over the two Nb's with 1 Mg in the nBn configuration, while C_Q(LAPW) for D2 is an average over all other Nb's. The sign of the C_Q is not determined from the NMR measurement.

	C_Q(LAPW)	C_Q(NMR)
D1	-34.97	28
D2	70.54	24

4.5.2 B atom NMR spectra comparison between simulations and experiments

In both PST and PSW simulation cells, the Sc with an isotropic nBn shell has the smallest V_{zz} than other Sc cations with both types of B cations in their nBn surrounding, as seen in Tables 4.2 and 4.3. In NMR experiments, a narrow peak is usually associated with B sites centered at an isotropic nBn environment [40, 41, 44]. Fig. 4.32 shows the calculated Sc quadrupole central peak static powder spectra for monoclinic, tetragonal, rhombohedral PST and the simulated spectrum from NMR measured C_Q = 3.8 MHz and η = 0.9 [41] for an ordered PST sample [27]. All of the simulated Sc spectra are seen to be much wider than that of the experiment, even the narrowest simulated spectrum of $R3m$ PST is about twice wider than the experiment. On the other hand, NMR Sc spectrum in a disordered PST single crystal yields a C_Q = 12 MHz [161], which corresponds to $|V_{zz}|$(Sc) $\approx$ 0.225 (10^{22} V/m^2). This measurement is close to the calculated $|V_{zz}|$(Sc) $\approx$ 0.159 in $R3m$ PST and $|V_{zz}|$(Sc) = 0.403 in $P4mm$ PST with c/a = 1.00.

Calculated quadrupole central peak static powder spectra for the 6Sc nBn surrounded Sc in $I4/mmm$ and $Immm$ PSW as well as the simulated spectrum from NMR measured C_Q = 4.4 MHz and η = 0.9 [41] for PSW are shown in Fig. 4.33. The simulated Sc spectra are seen to be about 4 times wider than that of the experiment.

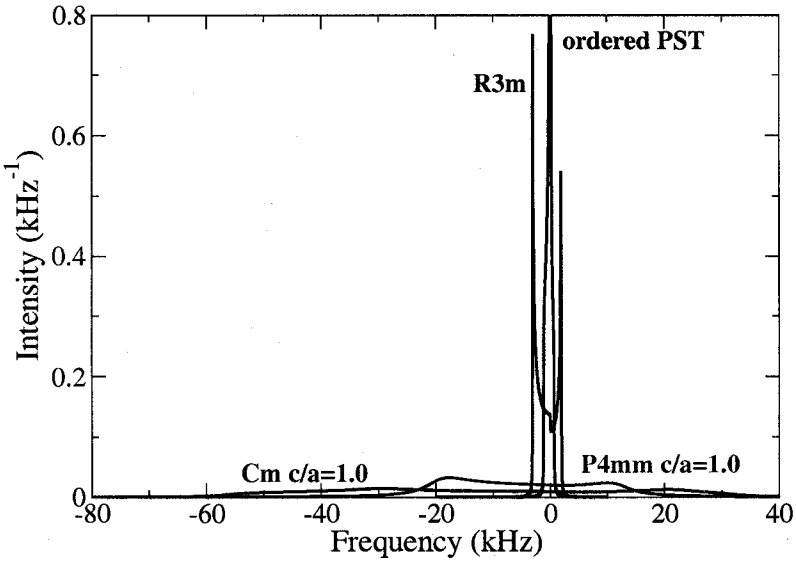

FIG. 4.32: Calculated NMR quadrupole powder spectra of ^{45}Sc in PST: calculated from the experimental C_Q = 3.8 MHz and η = 0.9 (black) [41]; PST [001]1:1 monoclinic c/a = 1.0 (red); PST [001]1:1 tetragonal c/a = 1.0 (green); PST [111]1:1 rhombohedral (blue).

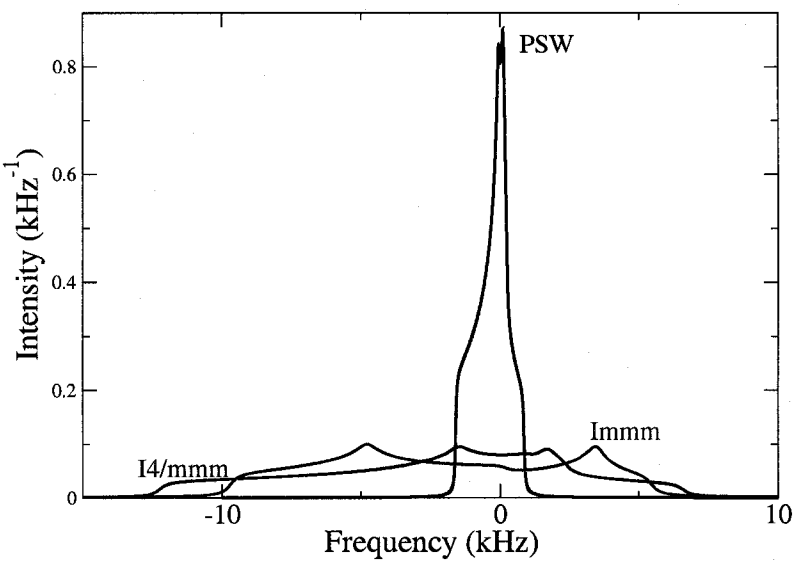

FIG. 4.33: Calculated NMR quadrupole powder spectra of ^{45}Sc in PSW: calculated from the experimental C_Q=4.4 MHz and η = 0.9 (black) [41]; $I4/mmm$ PST (red); $Immm$ PST (green).

High resolution NMR measured ^{93}Nb spectrum shows three peaks, a sharp peak assigned to Nb sites with 6 Mg^{2+} nBn sites, and two broad lineshapes, D1 and D2, associated with various nBn configurations containing up to 1 Mg^{2+} cation and configurations including 2 to 5 Mg^{2+} cations, respectively. In the 60-atom PMN simulation cell, there is no Nb atom with an isotropic Mg nBn shell. The measured quadrupole coupling constants C_Q corresponding to the two broad lineshapes are listed in Table 4.7, in comparison with the simulation results.

The average C_Q of Nb's with 1 Mg^{2+} in the nBn cage from the LAPW calculation is about 25% larger than the measured C_Q for lineshape D1, while the average C_Q of Nb's with 3Mg/3Nb and 5Mg/1Nb configurations is 3 times as large as the measured C_Q for lineshape D2 (Table 4.7).

In PST, PSW and PMN, the simulated B spectra are generally larger than the NMR measurements. Similar discrepancy was seen in Chapter 3 between the calculated and experimental Ti spectra in PZT. One possible explanation for this discrepancy is that the experimental spectra are motionally narrowed. Evidence of motional narrowing was recently reported in NMR quadrupole Ti spectra in single-crystal cubic phases of the related perovskites $BaTiO_3$ and $SrTiO_3$ [157]. These were interpreted as showing the mixed order-disorder and displacive character of the ferroelectric transition. The motional narrowing was interpreted as arising from a fast motion between eight nearly degenerate [111] off-centerings, with a slight bias, on a slower time scale, toward a local tetragonal polarization along a cubic direction. In PST and PSW, motional narrowing would be possible if there were several local structures which were energetically nearly degenerate. Like in PZT, a soft energy landscape was also seen in both PST and PSW. For example, the energies of the PST Cm $c/a = 1.0$ and the $R3m$ structures differ by about 6 mRy/perovskite-unit, and the energy difference between $Immm$ PSW and $I4/mmm$ PSW is only 0.3 mRy/perovskite-unit. The existence of these structures with small energy dif-

ference are consistent with possible motional narrowing in PST and PSW. A soft Born-Oppenheimer energy landscape, which is characteristic of ferroelectrics with high piezoelectric constants, also exists in PMN. This is conducive to the motional narrowing. Another possible reason for the discrepancy between the simulation and the NMR measurements in PMN is that the PMN simulation cell includes only three different nBn configurations, 1Mg/5Nb, 3mg/3Nb and 5Mg/1Nb, around Nb cations, as the NMR broad lineshapes contain the contributions from 5 different nBn configurations with 1 to 5 Mg cations.

Chapter 5

Conclusion

Electric field gradients (EFGs) were calculated for solid solutions $Pb(Zr_{1/2}Ti_{1/2})O_3$ (PZT), $Pb(Sc_{1/2}Ta_{1/2})O_3$ (PST), $Pb(Sc_{2/3}W_{1/3})O_3$ (PSW) and $Pb(Mg_{1/3}Nb_{2/3})O_3$ (PMN) using a first-principles LAPW method to study their local structures. To simulate 1:1 ordered PZT with homovalent Zr^{4+}, Ti^{4+} cations and 1:1 ordered PST with heterovalent Sc^{3+}, Ta^{5+} cations, a number of 10-atom supercells were used: [001] ordered with imposed monoclinic Cm symmetry, [001] ordered with imposed tetragonal $P4mm$ symmetry, and [111] ordered with imposed $R3m$ symmetry. Strains were applied to the [001] ordered unit cells. For PSW with 2:1 heterovalent Sc^{3+} and W^{6+} cations, 15-atom [111] ordered unit cells and 30-atom unit cells obeying the "random-site" model were used. The simulation cell for PMN with 2:1 heterovalent Nb^{5+} and Mg^{2+} cations contains 60 atoms arranged following the "random-site" model. All these relaxed structural models yielded pair distribution functions in good agreement with experiments, except for 15-atom PSW supercells. This indicated that all the PZT, PST unit cells and the PSW, PMN random-site supercells represent the atomic structure in these perovskite alloys well.

It has been shown by Wu and Krakauer [60] that for [001]1:1 ordered PZT

with imposed monoclinic Cm symmetry, the electric polarization is nearly parallel to the [001] (c-axis) for $c/a \gtrsim 1.04$, and it begins to rotate away from the c-axis at $c/a \sim 1.035$. The present calculations in PZT showed large changes of the EFGs as the electric polarization rotates between tetragonal and monoclinic symmetries. The onset of polarization rotation in Cm symmetry showed strong correlation with the shearing of the TiO_6 octahedra, and there was a sharp change in slope in the plot of Ti EFGs versus octahedral distortion index (DI). However, the plot of Ti EFGs versus longitudinal strain $|\alpha|$, another measure of the TiO_6 distortion, varied linearly. Results for the PZT oxygen EFGs were consistent with a greater sensitivity of the apex oxygen chemical shifts to the local environment compared to the equatorial oxygen atoms. This is in qualitative agreement with recent ^{17}O nuclear magnetic resonance (NMR) measurements of Baldwin *et al.* [39] In this ^{17}O NMR measurement, two oxygen peaks were assigned to apex and equatorial O sites according to their intensities. The apex O peak disappeared as the Zr concentration increased to 25%, while the equatorial O peak persisted up to 75% Zr in PZT. Furthermore, the Ti spectrum was insensitive to the Zr concentration. Baldwin *et al.* thus associated the existence of O peak with the existence of the Ti-O-Ti chain, and further suggested anisotropy in PZT local structure. However, our calculated Ti EFGs showed great sensitivity to local structure. Furthermore, examination of Pb-O bonds in our PZT structural models showed that instead of the anisotropy, the similar Ti-O bondlengths in all the PZT models could be used to explain the persistence of the "equatorial" O peak.

In 1:1 ordered heterovalent PST, large changes of calculated EFGs were also seen at $c/a = 1.02$. At the same c/a value, the Pb off-centerings with respect to the surrounding oxygen cage, which is related to the total polarization, started to rotate toward different directions as c/a increases. In PZT, the onset of polarization rotation in Cm symmetry showed strong correlation with the shearing of

the TiO_6 octahedra, and a sharp change in slope appeared in the plot of Ti EFGs versus octahedral distortion index (DI). In PST, an abrupt change in slope was also seen in plots of EFGs versus DI for both Sc and Ta atoms. By contrast with the monotonic change of $|\alpha|$(Ti) as a function of EFG in PZT, EFGs versus $|\alpha|$ for both Sc and Ta plots showed abrupt break of slope. Furthermore, both the axial and equatorial oxygen simulated NMR spectra were very sensitive to the change of the local environment.

The calculations of heterovalent PSW and PMN showed that Sc and Nb EFGs were strongly correlated to the number, identity and arrangement of its nBn cations, as deduced from experimental NMR spectra. Isotropic nBn configuration corresponded to the smallest V_{zz} of Sc and Nb atoms. When surrounded by anisotropic nBn configurations dominated by B cations with larger ionic radius (Sc and Mg), the centered B atoms tended to have larger V_{zz}'s. In the plot of Nb EFGs versus $|\alpha|$ in PMN, three well distinguished groups of data points were formed according to three different nBn configurations. In the plot of Nb EFGs versus DI in PMN, the data points separated into two groups only: the ones with one Mg in the nBn cage and the ones with more than one Mg in the nBn cage. By contrast, in the plots of Sc EFGs versus DI and Sc EFGs versus $|\alpha|$ in PSW, data points correlated weakly with the nBn environments. This may be explained by the limitation of the 30-atom PSW unit cells.

NMR experiments have been performed to measure the spectra of ^{47}Ti, ^{45}Sc, and ^{93}Nb isotopes in PZT, PST, PSW and PMN solid solutions, respectively. Compared to the EFG values of these atoms inferred from NMR measurements, the calculated B-atom EFGs in all four alloys are generally up to 3 times as large. One possible explanation for this discrepancy is the limitation of the simulation cells, even though these supercells are good representations of the local structure. Considering these ferroelectrics all have almost degenerate energy states, the discrepancy

can also be explained by the motional narrowing in NMR measurements, which is discussed in terms of static and dynamic structural models of these alloys.

After the EFGs were obtained, the next step to fully simulate the NMR experimental spectra is to calculate the chemical shielding on each inequivalent chemical site. In Professor Krakauer's research group, chemical shielding calculations are currently underway for many of the oxides discussed in this thesis.

Appendix A

Nuclear quadrupole central peak powder patterns

The method used to calculate the NMR EFG powder spectra is described in this Appendix. The Hamiltonian describing the nuclear quadrupole coupling of a nucleus with spin I is [81]

$$< Im'|H|Im >= \frac{eQ}{6I(2I-1)} \sum_{jk} V_{ij} < Im'|\frac{3}{2}(I_j I_k + I_k I_j) - \delta_{jk}\boldsymbol{I}^2|Im > \qquad \text{(A.1)}$$

where Q is the nuclear electric quadrupole moment and the I_j are the components of the nuclear spin operator. The nuclear quadrupolar coupling interaction is absent for nuclei with $I < 1$, since $Q = 0$ in this case [81]. V_{ij} is the symmetric traceless

electric field gradient (EFG) tensor at the nucleus and is defined by

$$V_{ij} = \lim_{(r_i,\, r_j)\to 0} \left(\frac{\partial^2 V(\mathbf{r})}{\partial r_i \partial r_j} - \frac{1}{3}\delta_{ij}\nabla^2 V \right), \tag{A.2}$$

where $V(\boldsymbol{r})$ is the Coulomb potential. The three eigenvalues of the EFG tensor are its principal components with respect to its principal axis $x\,y\,z$ reference frame defined by the corresponding eigenvectors. In conventional notation, the principal axes coordinates are labeled such that the eigenvalues of the EFG tensor are ordered as $|V_{zz}| > |V_{yy}| > |V_{xx}|$. Since the EFG tensor is traceless, these can be expressed in terms of two independent variables, V_{zz} and the asymmetry parameter η, which is defined as

$$\eta = \frac{V_{xx} - V_{yy}}{V_{zz}}, \tag{A.3}$$

and where $0 \leq \eta \leq 1$.

In the presence of large magnetic fields, the nuclear quadrupole interaction can be accurately treated as a perturbation of the Zeeman Hamiltonian, shifting the $(2I + 1)$ equally spaced Zeeman levels so that $2I$ distinct lines are observed in an NMR measurement. For half-integral I, the central transition ($m = 1/2 \leftrightarrow -1/2$) $\nu_{1/2}^{(2)}$ is shifted only in second-order and is surrounded by $2I - 1$ first-order satellite lines. The frequencies of the observed lines depend on the orientation of the quadrupolar principal axis frame with respect to the applied magnetic field. Measurements on powder samples are dominated by the $\nu_{1/2}^{(2)}$ resonance, since the orientation dependence of the first-order satellite lines makes them very broad and

difficult to observe. The explicit orientation dependence of the central resonance $\nu_{1/2}^{(2)}$ is given by [81, 82, 162]:

$$\begin{aligned} \nu_{1/2}^{(2)}(\mu,\phi) &= \nu_L - \left(\frac{R}{6\nu_L}\right) \\ &\times \left[A(\phi)\mu^4 + B(\phi)\mu^2 + C(\phi)\right], \end{aligned} \tag{A.4}$$

where ν_L is the Larmor frequency, $\mu = cos(\theta)$, and

$$\begin{aligned} A(\phi) &= -\frac{27}{8} - \frac{9}{4}\eta\cos(2\phi) - \frac{3}{8}\eta^2\cos^2(2\phi) \\ B(\phi) &= \frac{30}{8} - \frac{\eta^2}{2} + 2\eta\cos(2\phi) + \frac{3}{4}\eta^2\cos^2(2\phi) \\ C(\phi) &= -\frac{3}{8} + \frac{\eta^2}{3} + \frac{\eta}{4}\cos(2\phi) - \frac{3}{8}\eta^2\cos^2(2\phi) \\ R &= \frac{9}{\pi^2}\omega_Q^2\left[I(I+1) - \frac{3}{4}\right], \\ \omega_Q &= \frac{eQV_{zz}}{4I(2I-1)\hbar}. \end{aligned} \tag{A.5}$$

Here the Euler angles θ and ϕ describe the orientation of the applied magnetic field with respect to the EFG principal axis frame. A variety of conventions are used in the literature to describe the the quadrupolar coupling constant ω_Q in Eq. (A.4), such as $C_Q = eQV_{zz}/h$ or $\nu_Q = eQV_{zz}/h$.

In a powder sample, the variables μ and ϕ are randomly distributed, so the powder patterns shown in Figs. 3.8 - 3.11 are obtained, up to a normalization, by

averaging over these angles, yielding the spectral density

$$\rho(\nu) = \int_{-1}^{1} d\mu \int_{0}^{2\pi} d\phi \; \delta\left(\nu - \nu_{1/2}^{(2)}(\mu, \phi)\right). \tag{A.6}$$

To calculate $\rho(\nu)$ in Eq. (A.6), the delta function is replaced by a Lorentzian of finite width for each frequency ν and summed over the discretized angular integrals.

Chemically inequivalent sites for a given nuclear isotope will each produce their own characteristic EFG shifts and broadening of the observed NMR lines. In addition, each chemically inequivalent site will in general be subject to an anisotropic chemical shift of the NMR lines due to different screening of the applied magnetic field by induced electronic currents [82]. The combination of these effects can make it difficult to discriminate spectra arising from inequivalent sites. The width of the EFG powder pattern is inversely proportional to the magnetic field strength, as seen from Eq. (A.4), so high-magnetic fields help to improve the resolution of the spectra. Magic angle spinning (MAS) NMR techniques can also reduce the EFG broadening by effectively averaging to zero the second-order tensor part of the powder pattern in Eq. (A.4) and the broadening due to the anisotropic chemical shift. The calculated "static" powder patterns in this paper do not include this effect. We have not calculated the chemical shifts in the present work, as solid-state methods to accurately determine these in crystals for light to heavy atoms have only recently been developed using specialized computer codes [163, 164]. We have also calculated the powder patterns using exact diagonalization in the $(2m+1)$-dimensional I-subspace instead of perturbation theory, but the spectra obtained in these two

ways are virtually identical at the high magnetic fields now typically used in NMR experiments.

BIBLIOGRAPHY

[1] M. E. Lines and A. M. Glass, *Principles and Applications of Ferroelectrics and Related Materials* (Clarendon, Oxford, 1977).

[2] K. Uchino, *Piezoelectric Actuators and Ultrasonic Motors* (Kluwer Academic Publishers, Boston, 1996).

[3] G. E. Pake, *Solid State Physics Advances in Research and Applications*, vol. 2 (Academic Press, New York, 1956).

[4] G. Burns, *Introduction to Group Theory with Applications* (Academic Press, New York, 1977).

[5] J. F. Nye, *Physical Properties of Crystals* (Oxfort University Press Inc., New York, 1985).

[6] L. Carlsson, Acta Crystallorg. **20**, 459 (1966).

[7] F. Jona and G. Shirane, *Ferroelectric Crystals* (The McMillan Company, New York, 1962).

[8] W. Cochran, Phys. Rev. Lett. **3**, 412 (1959).

[9] W. Cochran, Adv. Phys. **19**, 387 (1960).

[10] W. Cochran, Adv. Phys. **20**, 401 (1961).

[11] Blinc and B. Zeks, *Soft Modes in Ferroelectrics and Antiferroelectrics* (North-Holland Publishing Co., New York, 1974).

[12] G. A. Samara and P. S. Peercy, Solid State Physics **36**, 1 (1981).

[13] G. A. Samara, Solid State Physics **56**, 239 (2001).

[14] L. L. Boyer, R. E. Cohen, H. Krakauer, and W. A. Smith, Ferroelectrics **111**, 1 (1990).

[15] L. E. Cross, in *Ferroelectrics* (1994), vol. 151, p. 305.

[16] G. A. Samara, J. Phys.: Condens. Matter **15**, R367 (2003).

[17] L. E. Cross, Ferroelectrics **7**, 241 (1987).

[18] G. Burns and F. H. Dacol, Ferroelectrics **104**, 25 (1990).

[19] G. A. Smolenskii and V. A. Isupov, Dokl. Akad. Nauk SSSR **97**, 653 (1954).

[20] R. E. Newnham, NIST Spec. Publ. **804**, 39 (1996).

[21] S.-E. Park and T. R. Shrout, J. Appl. Phys. **82**, 1804 (1997).

[22] P. Groves, J. Phys. C: Solid State Phys. **18**, L1073 (1985).

[23] Z. C. Kang, C. Caranoni, G. Nihoul, and C. Boulesteix, J. Solid State Chem. **87**, 308 (1990).

[24] K. S. Knight and K. Z. Baba-Kishi, Ferroelectrics **173**, 341 (1995).

[25] C. Malibert, B. Dkhil, J. M. Kiat, D. Durand, J. F. Berar, and A. S. de Bire, J. Phys.: Condens. Matter **9**, 7485 (1997).

[26] C. Perrin, N. Menguy, E. Suard, C. Muller, C. Caranoni, and A. Stepanov, J. Phys.: Condens. Matter **12**, 7523 (2000).

[27] W. Dmowski, M. K. Akbas, P. K. Davies, and T. Egami, J. Phys. Chem. Solids **61**, 229 (2000).

[28] N. Takesue, Y. Fujii, M. Ichihara, and H. Chen, Phys. Rev. Lett. **82**, 3709 (1999).

[29] M. Reaney, J. Petzelt, V. V. Voitsekhovskii, F. Chu, and N. Setter, J. Appl. Phys. **76**, 2086 (1994).

[30] J. Petzelt, E. Buixaderas, and A. V. Pronin, Mater. Sci. Eng. B **55**, 86 (1998).

[31] U. Bismayer, V. Devarajan, and P. Groves, J. Phys.: Condens. Matter **1**, 6977 (1989).

[32] H. Idink and W. White, J. Appl. Phys. **76**, 1789 (1994).

[33] E. Husson, Key Eng. Mater. **155**, 1 (1998).

[34] E. A. Rogacheva, Physica B **291**, 359 (2000).

[35] F. Jiang, S. Kojima, C. Zhao, and C. Feng, J. Appl. Phys. **88**, 3608 (2000).

[36] I. G. Siny, R. S. Katiyar, and A. S. Bhalla, Ferroelectrics Rev. **2**, 51 (2000).

[37] J. Kreisel, A. M. Glazer, P. Bouvier, and G. Lucazeau, Phys. Rev. B **63**, 174106 (2001).

[38] R. Blinc, A. Gregorovic, B. Zalar, R. Pirc, V. V. Laguta, and M. D. Glinchuk, J. Appl. Phys. **89**, 1349 (2001).

[39] A. Baldwin, P. A. Thomas, and R. Dupree, J. Phys.:Condens. Matter **17**, 7159 (2005).

[40] G. L. Hoatson, D. H. Zhou, F. Fayon, D. Massiot, and R. L. Vold, Phys. Rev. B **66**, 224103 (2002).

[41] W. J. Brouwer, *Nuclear magnetic resonance studies of relaxor ferroelectrics* (2005), Ph.D. dissertation.

[42] D. Zhou, *Multinuclear nmr studies of relaxor ferroelectrics* (2003), Ph.D. dissertation.

[43] D. H. Zhou, G. L. Hoatson, and R. L. Vold, J. Magn. Res. **167**, 242 (2004).

[44] R. L. Vold, G. L. Hoatson, and M. Vijayakumar, Phys. Rev. B **75** (2007).

[45] M. Vijayakumar, G. L. Hoatson, and R. L. Vold, Phys. Rev. B **75** (2007).

[46] C. A. Randall, D. J. Barber, R. W. Whatmore, and P. Groves, J. Mater. Sci. **21**, 4456 (1986).

[47] L. A. Bursill, P. Julin, Q. Hua, and N. Setter, Physica B **205**, 305 (1995).

[48] H. Lemmens, O. Richard, G. V. Tendeloo, and U. Bismayer, J. Electron-Microsc. **48**, 843 (1999).

[49] M. Abplanalp, D. Barosova, P. Bridenbaugh, J. Erhart, J. Fousek, P. Gunter, J. Nosek, and M. Sulc, Solid State Commun. **119**, 7 (2001).

[50] V. Westphal, W. Kleemann, and M. D. Glinchuk, Phys. Rev. Lett. **68**, 847 (1992).

[51] A. K. Tagantsev and A. E. Glazounov, Phys. Rev. B **57**, 18 (1998).

[52] R. Pirc and R. Blinc, Phys. Rev. B **60**, 13470 (1999).

[53] R. Blinc, J. Dolinsek, A. Gregorovic, B. Zalar, C. Filipic, Z. Kutnjak, A. Levstik, and R. Pirc, Phys. Rev. Lett. **83**, 424 (1999).

[54] V. Bobnar, Z. Kutnjak, R. Pirc, R. Blinc, and A. Levstik, Phys. Rev. Lett. **84**, 5892 (2000).

[55] G. A. Smolenskii, V. A. Isupov, A. I. Agranovskaya, and S. N. Popov, Sov. Phys. Solid State (English translation) **2**, 2584 (1961).

[56] D. Viehland, S. J. Jang, L. E. Cross, and M. Wuttig, J. Appl. Phys. **68**, 2916 (1990).

[57] B. Noheda, D. E. Cox, G. Shirane, J. A. Gonzalo, L. E. Cross, and S.-E. Park, Appl. Phys. Lett. **74**, 2059 (1999).

[58] H. Fu and R. Cohen, Nature **403**, 281 (2000).

[59] L. Bellaiche, A. Garcia, and D. Vanderbilt, Phys. Rev. Lett. **84**, 5427 (2000).

[60] Z. Wu and H. Krakauer, Phys. Rev. B **68**, 14112 (2003).

[61] B. Noheda, D. E. Cox, G. Shirane, S.-E. Park, L. Cross, and Z. Zhong, Phys. Rev. Lett. **86**, 3891 (2001).

[62] D. Vanderbilt and M. H. Cohen, Phys. Rev. B **63**, 094108 (2001).

[63] W. Dmowski, T. Egami, L. Farber, and P. K. Davies, in *Fundermental Physics of Ferroelectrics*, edited by H. Krakauer (AIP Conf. Proc., 2001), vol. 582, p. 33, We are grateful to W. Dmowski for making available numerical data corresponding to Figs. 3. 1 and 3. 2 in this dissertation.

[64] B. Jaffe, W. R. Cook, and H. Jaffe, *Piezoelectric Ceramics* (Academic Press, London, 1971).

[65] N. Setter and L. E. Cross, J. Appl. Phys. **51**, 4356 (1980).

[66] F. Chu, N. Setter, and A. K. Tagantsev, J. Appl. Phys. **74**, 5129 (1993).

[67] F. Chu, I. M. Reaney, and N. Setter, J. of the American Ceramic Society **78**, 1947 (1995).

[68] I. W. Chen, J. Chem. Phys. Solids **61**, 197 (2000).

[69] P. K. Davies and M. A. Akbas, J. Phys. Chem. Solids **61**, 159 (2000).

[70] P. Bonneau, P. Garnier, G. Calvarin, E. Husson, J. R. Gavarri, A. W. Hewat, and A. Morell, J. Solid State Chem. **91**, 350 (1991).

[71] O. B. Lapina, D. F. Khabibulin, K. V. Romanenko, Z. Gan, M. G. Zuev, V. N. Krasil'nikov, and V. Fedorov, Solid State NMR **28**, 204 (2005).

[72] J. J. Fitzgerald, S. Prasad, J. Huang, and J. S. Shore, J. Am. Chem. Soc. **122**, 2556 (2000).

[73] B. Zalar, V. V. Laguta, and R. Blinc, Phys. Rev. Lett. **90**, 37601 (2003).

[74] A.Abragam, *The Principles of Nuclear Magnetism* (Clarendon Press, Oxford, 1978).

[75] E. Fukushima and S. B. Roeder, *Experimental Pulse NMR: A Nuts and Bolts Approach.* (Addison-Wesley Publishing Company, Inc., London, 1981).

[76] C. P. Slichter, *Principles of Magnetic Resonance.*, vol. 1 (Springer-Verlag, New York, 1990), third edition.

[77] R. R. Ernst, G. Bodenhausen, and A. Wokaun, *Principles of nuclear magnetic resonance in one and two dimensions.* (Clarendon Press, Oxford, 1987).

[78] V. J. McBrierty and K. J. Packer, *Nuclear Magnetic Resonance in Solid Polymers.* (Cambridge University Press, New York, 1993).

[79] D. E. Leyden and R. H. Cox, *Analytical Applications of NMR*, vol. 48 (John Wiley & Sons, Inc., New York, 1977).

[80] T. P. Das and E. L. Hahn, Solid State Phys. (1957), supplement 1.

[81] M. H. Cohen and F. Reif, Sol. St. Phys. **5**, 321 (1957).

[82] J. F. Baugher, P. Taylor, T. Oja, and P. J. Bray, J. Chem. Phys. **50**, 4914 (1969).

[83] O. S. Harbison and H. W. Spiess, Chem. Phys. Lett. **124**, 128 (1986).

[84] K. A. Bell, G. L. Hoatson, and R. L. Vold, J. Magn. Reson. A **108**, 238 (1994).

[85] N. J. Stone, p. 1 (2001), http://www.nndc.bnl.gov/nndc/stone_moments/.

[86] R. B. Firestone, V. S. Shirley, C. M. Baglin, S. Y. Chu, and J. Zipkin, *The 8th edition of the Table of Isotopes (also 1998 and 1999 updates).* (John Wiley & Sons, Inc., New York, 1996).

[87] A. A. Gusev, I. M. Reznik, and V. A. Tsitrin, J. Phys.: Condens. Matter **7**, 4855 (1995).

[88] S. C. Schmidt, K. Sen, T. P. Das, and A. Weiss, Phys. Rev. B **22**, 4167 (1980).

[89] F. D. Wette, Phys. Rev. **123**, 103 (1961).

[90] P. Blaha, K. Schwarz, and P. Herzig, Phys. Rev. Lett. **54**, 1192 (1985).

[91] P. Blaha, K. Schwarz, and P. H. Dederichs, Phys. Rev. B **37**, 2792 (1988).

[92] P. Blaha, K. Schwarz, W. Faber, and J. Luitz, Hyper. Interact. **126**, 389 (2000).

[93] P. Blaha, J. Phys.: Condens. Matter **3**, 9381 (1991).

[94] K. Schwarz, C. Ambrosch-Draxl, and P. Blaha, Phys. Rev. B **42**, 2051 (1990).

[95] D. J. Singh, ferroelectrics **153**, 183 (1994).

[96] M. D. Johannes and D. J. Singh, Phys. Rev. B **71**, 212101 (2005).

[97] H. M. Petrilli, P. E. Blöchl, P. Blaha, and K. Schwarz, Phys. Rev. B **57**, 14690 (1998).

[98] D. Alfè, M. J. Gillan, and G. D. Price, Nature **401**, 462 (1999).

[99] M. Côté, P. D. Haynes, and C. Molteni, J. Phys.: Condens. Matter **14**, 9997 (2002).

[100] C. K. Skylaris, O. Igglessi-Markopoulou, A.Detsi, and J. Markopoulos, Chem. Phys. **293**, 355 (2003).

[101] C. Molteni, I. Frank, and Parrinello, J. Am. Chem. Soc. **121**, 12177 (1999).

[102] E. Artacho, M. Rohlfing, M. Côté, P. D. Haynes, R. J. Needs, and C. Molteni, Phys. Rev. Lett. **93**, 116401 (2004).

[103] M. Born and J. F. Oppenheimer, Ann. Physik **84**, 457 (1927).

[104] R. M. Martin, *Electronic Structure: Basic Theory and Practical Methods* (Cambridge University Press, Cambridge, 2004).

[105] W. Kohn and L. J. Sham, Phys. Rev. A **140**, 1133 (1965).

[106] L. Hedin and B. I. Lundquist, J. Phys. C **4**, 2064 (1971).

[107] R. O. Jones and O. Gunnarsson, Rev. Mod. Phys. **61**, 689 (1989).

[108] A. D. Becke, Phys. Rev. A **38**, 3098 (1988).

[109] J. P. Perdew and Y. Wang, Phys. Rev. B **45**, 13244 (1992).

[110] J. P. Perdew, K. Burke, and M. Ernzerhof, Phys. Rev. Lett. **77**, 3865 (1996).

[111] M. E. Casida, in *Recent Developments and Applications of Density Functional Theory*, edited by J. M. Seminario (Elsevier, Amsterdam, 1996), p. 391.

[112] T. Grabo, T. Kreibich, S. Kurth, and E. K. U. Gross, in *Strong Coulomb Correlations in Electronic Structure: Beyond the Local Density Approximation*, edited by V. I. Anisimov (Gordon & Breach, Tokyo, 1998).

[113] D. M. Bylander and L. Kleinman, Int. J. Mod. Phys **10**, 399 (1996).

[114] A. D. Becke, J. Chem. Phys. **98**, 1372 (1993).

[115] A. D. Becke, J. Chem. Phys. **98**, 5648 (1993).

[116] J. P. Perdew, M. Ernzerhof, and K. Burke, J. Chem. Phys. **105**, 9982 (1996).

[117] W. E. Pickett, Comp. Phys. Rep. **9**, 115 (1989).

[118] H. Hellmann, *Einfuhrung in die Quantumchemie* (Franz Duetsche, Leipzig, 1937).

[119] R. P. Feynman, Phys. Rev. **56**, 340 (1939).

[120] X. Gonze, J.-M. Beuken, R. Caracas, F. Detraux, M. Fuchs, G.-M. Rignanese, L. Sindic, M. Verstraete, G. Zerah, F. Jollet, et al., Computational Materials Science **25**, 478 (2002).

[121] G. Gilat, J. Comp. Phys. **10**, 432 (1972).

[122] O. Jepsen and O. K. Andersen, Sol. St. Comm. **9**, 1763 (1971).

[123] G. Lehmann and M. Taut, Phys. Status Solidi **54**, 469 (1972).

[124] D. J. Chadi and M. L. Cohen, Phys. Rev. B **8**, 5747 (1973).

[125] H. J. Monkhorst and J. D. Pack, Phys. Rev. B **13**, 5188 (1976).

[126] H. J. Monkhorst and J. D. Pack, Phys. Rev. B **16**, 1748 (1977).

[127] N. W. Ashcroft and N. D. Mermin, *Solid State Physics* (Saunders college publishing, Orlando, 1976).

[128] D. R. Hamann, M. Schlüter, and C. Chiang, Phys. Rev. Lett. **43**, 1494 (1979).

[129] G. B. Bachelet, D. R. Hamann, and M. Schlüter, Phys. Rev. B **26**, 4199 (1982).

[130] N. Troullier and J. L. Martins, Phys. Rev. B **43**, 1993 (1991).

[131] A. M. Rappe, K. M. Rabe, E. Kaxiras, and J. D. Joannopoulos, Phys. Rev. B **41**, 1227 (1990).

[132] http://opium.sourceforge.net/.

[133] O. K. Andersen, Phys. Rev. B **12**, 3060 (1975).

[134] J. C. Slater, Phys. Rev. **51**, 846 (1937).

[135] D. J. Singh, *Planewaves, pseudopotentials and the LAPW Method* (Kluwer Academic publishers, Boston, 1994).

[136] D. Singh, Phys. Rev. B **43**, 6388 (1991).

[137] M. Weinert, J. Math. Phys. **22**, 2433 (1981).

[138] J. D. Jackson, *Classical Electrodynamics, Third Edition* (John Wiley and Sons, Inc., 1998).

[139] S. Wei and A. Zunger, J. Chem. Phys. **107**, 1931 (1997).

[140] J. Ehmann and M. Fahnle, Phys. Rev. B **55**, 7478 (1997).

[141] R. Sternheimer, Phys. Rev. **84**, 244 (1951).

[142] B. Noheda, J. Gonzalo, L. Cross, R. Guo, S.-E. Park, D. Cox, and G. Shirane, Phy. Rev. B **61**, 8687 (2000).

[143] T. Proffen and S. J. L. Billinge, Journal of Applied Crystallography **32**, 572 (1999).

[144] D. Padro, V. Jennings, M. E. Smith, R. Hoppe, P. A. Thomas, and R. Dupree, J. Phys. Chem. B **106**, 13176 (2002).

[145] Calculations of hyperfine spectra and powder spectra were performed using a computer program provided by R. Vold.

[146] R. K. Harris, E. D. Becker, S. D. Menezes, R. Goodfellow, and P. Granger, Pure Appl. Chem. **73**, 1795 (2001).

[147] D. Padro, A. P. Howes, M. E. Smith, and R. Dupree, Solid State Nuclear Magnetic Resonance **15**, 231 (2000).

[148] P. Herzog, B. Klemme, and G. Schaefer, Z. Physik **269**, 265 (1974).

[149] W. Troeger, M. Dietrich, J. P. Araujo, J. G. Correia, H. Haas, and ISOLDE-Collaboration, Z. Naturforsch **57a**, 586 (2002).

[150] S. Friedemann, F. Heinrich, H. Haas, and W. Troeger, Hyperfine Interactions **159**, 313 (2004).

[151] R. B. Firestone, V. S. Shirley, S. Y. F. C. C. M. Baglin, and J. Zipkin, *Table of Isotopes, 8th Edition* (John Wiley & Sons, Inc., 1999).

[152] M. Dietrich, private communication: talk presented at the ISOLDE/CERN Physics Workshop, Geneva, Switzerland, 15-17 Dec. 2003; url-http://isolde.web.cern.ch/ISOLDE/Workshop2003/workshop2003.htm. ν_Q in this reference is equal to C_Q defined in Appendix A.

[153] D. J. Payne, R. G. Egdell, A. Walsh, G. W. Watson, J. Guo, D. A. Glans, T. Learmonth, and K. E. Smith, Phy. Rev. Lett. **96**, 157403 (2006).

[154] G. Shirane and R. Pepinsky, Phy. Rev. **97**, 1179 (1955).

[155] A. M. Glazer and S. A. Mabud, Acta Cryst. B **34**, 1065 (1978).

[156] W. H. Baur, Acta Crystallogr. B **30**, 1195 (1974).

[157] B. Zalar, A. Lebar, J. Seliger, R. Blinc, V. V. Laguta, and M. Itoh, Phys. Rev. B **71**, 064107 (2005).

[158] P. Juhas, I. Grinberg, A. M. Rappe, W. Dmowski, T. Egami, and P. K. Davies, Phys. Rev. B **69**, 214101 (2004).

[159] T. Mitsui, E. Nakamura, and K. Gesi, in *Oxides* (Springer, Berlin, 1981), vol. Landolt-Bornstein, New Series, Group III,Vol. 16, Pt. a.

[160] T. Egami, W. Dmowski, M. Akbas, and P. K. Davies, in *First Principles Calculations for Ferroelectrics*, edited by R. E. Cohen (AIP, Melville, NY, 1998), p. 1.

[161] R. Blinc, A. Gregorovic, B. Zalar, R. Pirc, and S. G. Lushnikov, Phys. Rev. B **61**, 253 (2000).

[162] K. Narita, J.-I. Umeda, and H. Kusumoto, Journal of Chemical Physics **44**, 2719 (1966).

[163] F. Mauri and S. G. Louie, Phys. Rev. Lett. **77**, 5300 (1996).

[164] C. J. Pickard and F. Mauri, Phy. Rev. B **63**, 245101 (2001).

Vita

Dandan Mao

Dandan Mao was born on the twentieth of October, 1978 in Hubei, China. She attended the high school of Jianghan Petroleum University and graduated in July, 1995. The following August she entered Peking University in Beijing, China, and received her Bachelor of Arts in nuclear physics in July, 1999. She entered the College of William and Mary in August, 1999, and received her Master of Science degree in physics in December, 2000. This PhD dissertation was defended on June 1, 2007 at the College of William and Mary in Williamsburg, Virginia.